Title
Explorations of spin excitations and dynamics in homonuclear and heteronuclear spin-1 atomic gases

Author
FANG, FANG

Publication Date
2020

Explorations of spin excitations and dynamics in homonuclear and heteronuclear spin-1 atomic gases

by

Fang Fang

A dissertation submitted in partial satisfaction of the

requirements for the degree of

Doctor of Philosophy

in

Physics

in the

Graduate Division

of the

University of California, Berkeley

Committee in charge:

Professor Dan M. Stamper-Kurn, Chair
Professor Holger Müller
Professor Ming Wu

Fall 2019

Explorations of spin excitations and dynamics in homonuclear and heteronuclear spin-1 atomic gases

Abstract

Explorations of spin excitations and dynamics in homonuclear and heteronuclear spin-1 atomic gases

by

Fang Fang

Doctor of Philosophy in Physics

University of California, Berkeley

Professor Dan M. Stamper-Kurn, Chair

Ultracold atomic system provides us a versatile platform to address problems ranging from quasi-particle excitations supported by a variety of ground states, to cold collisions which could lead to a precise determination of interatomic molecular potential, and to atomtronics focusing on atomic analogues of electronic components. In this dissertation, I describe our efforts in exploring a wide topic range by our ^{87}Rb Bose Einstein condensate (BEC) machine and ^{7}Li - ^{87}Rb mixture machine, including magnons, which are collective spin excitations supported by Rb F = 1 ferromagnetic BEC ground state, cold elastic collisions between Li and Rb co-trapped in a spherical quadrupole trap, and Li spin dynamics in a spin bath formed by Rb.

To my parents, for their unconditional support

Contents

List of Figures

List of Tables

Acknowledgments

The work documented in this thesis cannot be finished without the help and support from lots of people during my time at Berkeley.

First, I would like to acknowledge my PhD advisor, Dan Stamper-Kurn, for his patience, considerable support, insights about physics, from which I benefited and learned so much. Sometimes we refer to him as the ”most strict referee” for his ability to catch every corner of the problem we are faced with, some of which might not be challenged by a journal referee.

I acknowledge support from members of Stamper-Kurn team. They are first-rate colleagues and friends from whom I learned and benefited so much. Therefore, I acknowledge Jennie Guzman, Gyu-boong Jo, Nicolas Spethmann, Sydney Schreppler, Claire Thomas, Vincent Klinkhamer, Thomas Barter, Jonathan Kohler, Zephy Leung, Justin Gerber, Emma Deist, Julian Wolf, Kayleigh Cassella, Johannes Zeiher, Severin Daiss, Scott Eustice, Govind Unnikrishnan, Masayuki Okano, Shantanu Debnath, Charles Brown and everyone I neglected listing name here.

Special acknowledgments go to E4 team, Ed Marti, Andrew Macrae, Holger Kadau, Eric Copenhaver, Thomas Mittiga, Joshua Issacs, Aaron Smull, Katinka Horn, Dalila Robledo for their acceptance and support over years long struggle. Special thanks goes to Ryan Olf, for his patience and mentor in my early career. Special thanks goes to Shun Wu, for her firm support and contribution in the Li - Rb project.

Special recognition goes to the student machine shop owner, Joseph Kant, for his patience in training someone like me without any skill and apparently learning really slowly in machining technique in my early career, and for his help and patience in responding to my last-minute request with a vague design goal in my later career. Acknowledgments should also go to our main shop workers Warner Carlisle, Tommy Gutierrez, Abel Gonzalez, Gordon Long for their patience for my hand-drawn immediate request.

I should thank our purchasing team, Carlos Bustamante, Stephen Pride, our building manager , Anthony James Vitan, for their patience and assistance during my time here. I should thank our former adminitrator Anne Takizawa, as well as our current administrator Joelle Miles, and Donna K. Sakima, for her assistance in GSI recruitment, and our travel reimbursement team.

Graduate school cannot be enjoyable without the accompany of friends. I would like to thank Shudan Zhong, for the countless enjoyable lunch and chat over the years at Berkeley. I would like to thank Dandan Zhang, my roommate over five years at Berkeley, for her support and patience when I was frustrated in lab and late for almost everything. I would like to thank Kayleigh Cassella for the warm chat and suprising gift. I would like to thank Katinka Horn for all the culture and thoughts sharing chat, countless enjoyable lunch/dinner, and her support and encouragement when I was deep in frustration. I would also like to say thanks to a cat named ”Happy” owned by my landlord lady who was always ready to offer me a warm welcome during my countless late night arrival from the lab.

Finally, I would like to thank my parents, for all the privilege and priority they offered me, and for their unconditional support over this long journey. When I was deep in doubt about myself and sometimes everything, they were always standing by me and backed me up.

Chapter 1

Introduction

A postdoc researcher who worked with me during my long PhD journey, Shun Wu, once told me a sentence which I can't agree more: Every PhD has his/her own story. In this intro-chapter, I am going to share my PhD journey with you over seven years at Berkeley. This chapter will be written in a narrative way, together with some motivations and brief explanations for the physics topics we encounter as we move forward in independent sections. Because this is a PhD story, I will include failures I encountered, which cost time without leading to publication. If you are reading this chapter, please do not feel guilty about it. Just take a break reading it before you jump into later chapters which might be helpful for your busy research life[1].

In fall 2012, I was accepted as a graduate student at UC Berkeley. At that time, I really enjoyed my 11 hours flight over the Pacific Ocean to San Francisco, which was actually my first time over 21 years of life to be on an air-plane[2]. Without much of time to explore this foreign new land, I met our graduate mentor, Dmitry Budker and immediately dived into the busy graduate life here. The first task for the incoming PhD students was a preliminary test on physics offered by the department. As I finished my undergraduate study in summer, all knowledge of physics was still fresh in my head. Therefore, I took the test and passed it without much of a headache. Then the real headache came: I was appointed as a graduate student instructor immediately after I passed the language test with the lowest score(B^-), although the department secretary guaranteed me a physics reader position no matter I passed the test or not. Later I realized that, as a public university, Berkeley was always short in GSIs for intro-level physics courses, which was required for both science and engineer majors. The memory of my first class was still vivid in my head: I wrote down and memorized the sentences that I planned to say and, then, recited them in front of my pre-medical students, embarrassed. As time went on, I started to feel comfortable interacting with my students. Sometimes I put maths symbols, as well as physics formulas, on blackboard and asked them to teach me how to say it in English. This experience turned out to be very

---

[1] I read other people's intro-chapters on their stories, too.

[2] I no longer enjoy long time on air plane as time goes on

helpful for me to improve my communication skills, which was crucial to survive in a research group here, as an international.

Fascinated by experimental AMO physics back in my undergraduate days, I made appointments with AMO professors in the department and was later accepted as a graduate student researcher by Prof. Dan Stamper-Kurn after the summer 2013. Without much of experimental experience and skill, the E4 team, including two senior graduate students, Ed Marti and Ryan Olf, and a postdoc, Andrew MacRae, kindly welcomed and accepted me. Starting from daily optical alignment and soldering, I gradually became familiar with the Rb BEC machine, as well as their PhD stories. E4 was initially designed as a dual species machine dedicated to Li and Rb and the experimental theme is dual species atom interferometry in a micro-fabricated ring trap. At the time that I joined, Li was abandoned and they settled down to study an interesting topic: magnons in a spin-1 ferromagnetic BEC. This topic was related to the traditional direction of Dan's group, spinor Bose gas, and turned out to be very fruitful.

1.1 Magnon series in E4

Magnons are quasi-particles describing collective spin excitations in a magnetic ordered medium. For Rb spin -1 BEC, the ground state is ferromagnetic breaking the SO(3) rotational symmetry of its Hamiltonian, leading to a Goldstone boson with quadratic dispersion, which is our research topic, magnons. More discussions on magnons can be found in Chapter 2.

In Ed's work [1], this quadratic dispersion is confirmed experimentally through contrast interferometer methods, where magnons with different $\boldsymbol{k}$ are created through optical Zeeman effect and their evolution are subsequently monitored through state sensitive in-trap imaging method. Later in Ryan's work [2, 3], magnons are shown to be able to act as a coolant and a thermometer for the majority condensate. One core technique here is spin sensitive microwave addressing non-destructive absorption imaging method, which has been well documented in Eds' thesis.

My contribution for this magnon series is to be able to condense them and confirm their living environment is indeed flat. Along this journey, we found that we are only able to make magnon quasi-condensate with spatial inhomogeneity decorated by the so-called Mermin-Ho spin textures. This magnon quasi-condensate coarsens slowly during its entire lifetime in the dipole trap. The technical side contribution I was able to make is to incorporate spin-echo technique to our spin sensitive *in situ* imaging. This allows us to image the transverse magnetization. The main obstacle for E4 apparatus is that we have fairly weak radio frequency (rf) coupling to atoms. The environmental magnetic field noise prevents us from doing π pulse for the Zeeman sub-levels. As I recalled back in the days, even a reliable $\frac{\pi}{2}$ pulse had to be done at quiet late night. Two improvements have been made. First, we built three big bias coils around the optical table and fed the current back to the reading of a magnetometer placed right next to the experimental chamber. This effort made rf transfer more robust, for instance, against magnetic field disturbances caused by motion of the elevators in Birge Hall. However, we still could not perform a π pulse. This effort was done by Eric Copenhavor, under the supervison of Ryan Olf. During this exploration, we found the magnetometer's reading displayed stable 60 HZ AC line noise, leading to our second effort where we synchronized our rf pulse to this 60 HZ AC line noise. After careful adjustment in the resonant rf frequency, we were finally able to do reliable π pulse, however, still in late quiet night. In my later graduate career, we made a third improvement: adding a second stage amplification on RF signal with a single channel industrial amplifier (AETECHRON 7228), recommended by a later postdoc, Joshua Issacs. With this extra amplification stage, we are able to increase rf coil current by more than a factor of two.

At the end of these three works on magnons and spinor BEC, there were still many more interesting topics to explore, including real time vortex tracking through magnon interferometer, magnon mass shift study, and coarsening of magnon quasi-condensate. However, with the inherit technique difficulties related with E4 apparatus such as the weak rf coupling and low imaging resolution, we assessed that these struggles made further progress on spinor BEC research too costly in this specific setup. Along with the recent emergent exciting field of ultracold molecule [4], we decided to switch back on the dual species machine to work with bosonic Li and Rb again. The idea was to cool both species down to near quantum degeneracy, associate them into weakly bounded Feshbach molecule [5], and finally coherently transfer them into the ro-vibrational ground state [6–10]. The dipole moment for LiRb combination is the second largest among the diatomic alkali combinations. This large dipole moment can give rise to a relative strong long range anisotropic dipole - dipole interaction [11], which could be observed in a lattice of LiRb molecular gas with relative low fillings. With this ultimate goal in mind, together with an existing Li laser system, a dual species Zeeman slower and some optics for the dual species magneto-optical trap (MOT) that had already been selected to incorporated 671 nm wavelength dedicated to Li, we started to put Li back into our apparatus. Our plan was to use the current E4 machine to progress as far as we could toward creating LiRb molecules, learning (and finding scientific opportunities) along the way. Meanwhile, we would also work on the design of a brand new machine dedicated to this research direction. At this time, we were joined by a postdoc, Shun Wu and a graduate student, Thomas Mittiga. In the late 2015 and early 2016, the three of us did an oven change from a single species oven to a dual species one, adapted the design from Ryan Olf several years ago. Meanwhile, we were also working on Li laser setup to recover it back to life, finally leading to a completely rebuilding and redesigning. These efforts could be found in Chapter 3. Then Thomas decided to leave the group to work with Prof. Norman Yao on NV centers before we turned the dual species oven back on.

1.2 Li MOT searching

As a first test of Li flux, we sent a laser light with two colors down from our slower to the exit of the oven nozzle while running the Li oven. The first color was to address the Li

D_2 cycling transition compensated by the Doppler shift. The second color was for repump purpose. With this light on, we were able to observe Li fluorescence, both on a camera and directly by eye. Increasing the oven temperature, we observed Li flux became brighter, as expected. Confirming the fact that we did have Li in our oven, we went ahead to incorporate Li magneto-optical trap (MOT) optics to the existing Rb optics. The waveplates we used for the dual-color MOT setup was multi-order dual color waveplates from Foctek, designed to be a half waveplate for one wavelength and a full waveplate for another, or a quarter waveplate for both colors. These waveplates gave us independent control in beam balance adjustment for the two atomic species[3]. Without much of an effort, we were able to get Rb MOT back. With Rb as a guide, we aligned Li MOT laser beam to the Rb MOT laser beam. Our slower was initially designed to allow simultaneous slowing of both Li and Rb atoms. Due to the large mass difference, Li can follow a rapid field change and still stay adiabatic compared to Rb. At the same time, the small mass of Li leads to a large recoil energy which can cause severe transverse heating. Combined with these facts, the right way to create slow Li atomic flux was to rapidly slow it down just before it entered the MOT region, and, at the same time, shrink the distance between the MOT center and slower exit. Our slower design incorporated the above mentioned ingredients. To load Li, we thus changed the slower configuration, including running a “boost” coil at the end of the slower to rapidly slow Li down. This boost coil could change the field in the MOT region, and thus required compensation. This compensation was done by running a pair of coil in Helmholtz configuration around the MOT region along the slower axis. With Rb MOT as a target, we adjusted the current in the compensation coil according to the boost coil current. This measurement calibrated the magnetic field gradient settings for Li MOT. With these tools in hand, after one month search, we observed Li MOT in our chamber with 180 A running in the boost coil. One small accident happened during the period: the MOSFETs for the boost coil power supply burned themselves[4] with smoke. This smoke and bad smell ”attracted” our lab neighbors to knock the door and asked “Are you OK?” We were of course OK except our poor MOSFETs. Then we started to optimize this Li MOT by adjusting beam balance, slower coil current, corresponding MOT/slower laser frequency. However, with all this optimization, we were not able to boost Li number in the MOT. The details of Li MOT performance are documented in Chapter 3.

1.3 Li Rb co-existence

Without much of a success in Li MOT optimization, we decided to move on and worked with several times 10^7 Li in the MOT, along with several times 10^9 Rb in the MOT. Then our immediate observation was a severe loss in Li MOT number when it overlapped with the big Rb MOT. This lossy channel was mainly from the inelastic collisions between Li and excited state Rb. One way to shrink the number of atoms in excited state in MOT was to make

---

[3] However, these waveplates are imperfect and can cause trouble. See Chapter 3 for details.

[4] We had them in parallel for high current applications.

a dark spot MOT, which could be achieved simply by blocking the center position of the repump laser, for Na atoms [12]. The idea for dark spot MOT is that atoms are captured by the edge where there is repump light illumination and accumulated into very high density in the center position where there is no photon scattering happen. However, due to the less leaky cycling transition in Rb, it is more complicated to implement a dark spot MOT [13]. Typical methods involve imaging an opaque spot to the center of MOT and simultaneously illuminating with depump light. We gave it a try by blocking the center of the repump beam and overlapping the spot which was blocked with depump light. However, this configuration disturbed Rb MOT a lot and did not lessen Li loss dramatically. We were stuck there for a while and suspected the problem was from the incomplete blocking of repump light.

With this problem in mind, I attended a conference held in Newcastle University in England where I presented our work on magnon series there, in replacement of my advisor. There I met Xiaoke Li, a former graduate student from Prof. Dajun Wang's group in CUHK, who worked with NaRb mixtures for his PhD. It turned out that they had similar problems for Na-Rb combination. Their way to get around this problem was to add a little imaging light along one MOT beam path to displace one species relatively away from the other. This spatial separation effectively removed this issue and this extra light could be gradually turned off for later operation. Due to the fact that the imaging light was near resonance, relatively low power was needed to displace the MOT. This discussion made me realize a "pusher" beam formed by Rb imaging light to displace it away from Li during the loading stage could be the right way to move forward.

Before I went back to work in lab, I took a trip to visit Cambridge university, which has played such a famous role in the development of science. It was around September, with lots of tourists from all over the world. I purchased tickets to visit King's college, Queen's college and Trinity College. I was astonished by grass there. They looked so soft and clean for which I could believe they had super hardworking gardeners. I also enjoyed a boat trip passing by the Bridge of Sighs, with the guide talking about the history of the University. Then I followed the crowd to the site memorializing a famous Chinese poet, Xu Zhimo, with his famous "Taking Leave of Cambridge Again". This poem was required to recite back in my middle school days which I had a hard time reciting. However, even with Cambridge in front of my eye, I was still astonished by the poet's imagination to connect the real scenery to the gorgeous interpretation in his poem. As my last stop, I visited the chapel and took a picture with the statue of Sir Isaac Newton with the hope that he could generously share some luck with me for my physics research. However, as you will see soon, there was actually no luck happen. Therefore, maybe we can conclude here that praying cannot solve any problem.

After this brief trip, I was back to the lab and we turned on our imaging light during Rb MOT loading to displace it relative to Li MOT. We optimized this "pusher" by scanning its frequency and adjusting its intensity while monitoring both Li and Rb number in MOT. Finally, we parked the "pusher" intensity and frequency at the region where Li and Rb both had stable atom number in the MOT without much loss of Li number due to spatial overlap with Rb. After the loading stage, we gradually turned off this "pusher" in 20 ms before we detuned the MOT laser frequency, turned off the magnetic field gradient for the molasses cooling stage. This molasses stage could take several tens of ms. We first confirmed that during this time, there was no loss happen for Li due to inelastic collisions. Then we came to next challenge. Due to the unresolved hyperfine structure of Li, unlike Rb for which polarization gradient cooling [14] automatically worked at D_2 transition, Li temperature would be stuck at hundreds of micro-Kelvin for Li D_2 molasses. Therefore, we needed to figure out a way to cool Li down below Doppler limit. At this point, we realized that a recent technique, gray molasse cooling, had been developed and applied to alkali atoms as ^{39}K [15], ^{6}Li/^{7}Li [16, 17] with unresolved hyperfine structure. Similar technique had also been applied to direct molecular cooling [18, 19]. The idea of gray molasses includes a blue molasses on D_1 transition and a dark state induced by the intense principal cooling light slightly blue detuned from D_1 transition, and its weak sidebands on the repump frequency of Li, in a Λ configuration. With blue detuned principal cooling light, Li atoms are more likely to be decelerated at high energy, thus in bright states. As they are slowed down, they start to accumulate in the near zero - velocity dark states. Therefore, gray molasses is neither bright nor dark. That is why it is called “gray”, in the middle of bright and dark.

1.4 Li gray molasses cooling

To apply this technique to our system, we designed and built a laser system dedicated to this purpose. This effort is documented in Chapter 3. We aligned this D_1 laser to the MOT path. Initially, we did not see this cooling effect when we first shone it to the Li atoms. After several rounds of tweaking of the laser frequency without much luck to get it to work, we finally found a finer compensation of field gradient was the key, leading to a temperature of around 40 μK. Incorporating Li gray molasses cooling into our experimental sequence was natural because at this point, Rb was automatically undergoing polarization gradient cooling. At the end of this molasses stage, both species were at a temperature of tens of μK. Then we were ready to trap them simultaneously in our spherical quadrupole trap. The plan was to perform forced microwave evaporation on Rb. Meanwhile, Li would be sympathetically cooled by Rb without severe loss in atom number. Sympathetic cooling relied on the fact that Rb number was much larger than Li number together with a relative strong interspecies interaction strengths. Majorana loss could be a concern at lower temperature for spherical quadrupole trap with a zero field trap minimum, where atoms could undergo non-adiabatic spin-flip processes, leading to atom loss. We thus decided to purchase a green laser serving as the optical plug for preventing the system from Majorana loss [20]. In our experiment, we were able to co-trap 6×10^8 Rb with 2×10^7 Li, thus satisfying the first criterion. Previous studies on Li - Rb mixture system on Feshbach resonance positions and triplet scattering length made it possible for the theorists to decide the parameters for the interspecies molecular potential, which, in principle, could be used to predict the collision cross section between any combinations of magnetic sub-levels. However, we made a mistake in estimating the cross section for Li and Rb in $|1,-1\rangle$ from the theoretically determined singlet and triplet interspecies scattering length. This mistake overestimated the cross section and misled us to believe the cross section was OK for the sympathetic cooling to work.

1.5 Li Rb co-trapped in spherical quadrupole trap with optical plug

Around Christmas in 2016, we had both species transfered from molasses stage into the spherical quadrupole trap after a short optical pumping stage. Both species were trapped in $|1, -1\rangle$ state. As I recalled back, we did a quick experiment where we had Li in contact with Rb reservoir of different temperature. This experiment was done by holding Li with Rb for a variable time, and then imaging Li atomic distribution after a finite time of flight (TOF). The observation was that we did not see obvious momentum distribution change of Li. The momentum distribution was initially anisotropic. This anisotropy arises from a mismatch between the spherical or slightly prolate spatial distribution of the atoms at the end of laser cooling, and the oblate equipotential lines of the spherical-quadrupole trap. To our surprise, this anisotropy lasted for 40 s hold in the trap. We later realized similar behavior had been observed for the fermionic Li system [21, 22]. This adventure is recorded in detail in Chapter 4.

At that time, we suspected that the problem was from Majorana loss process. Meanwhile, our 15 W green laser was shipped to us. Therefore, we decided to implement this optical plug trap first. As I looked back from now, the Christmas data had already suggested that the interspecies cross section was much smaller than we expected. Therefore, at that time, we should have been more careful and talked to a theorist about this calculation. Fig. 1.1 showed our optical set-up for this optical plug. This green laser was first sent through several cylindrical lens for beam shaping purpose before propagating through the final 250 mm achromat directly in front of the chamber viewport. The goal was to overlap the resultant 19 μm waist focal point to the center of the spherical quadruple magnetic trap, forming an optical barrier. We thus built an imaging path along the beam path of the plug beam. With this imaging path, we were able to image the Rb cloud distribution on the CCD camera. This image helped us determine the x-y position of the plug beam, which would be at the center of Rb cloud image. For the z position, we moved the 250 mm achromat along the optical axis on a translation stage. The plug position was optimized by decreasing the beam power while maintaining plug trap performance. Without the plug beam, we were only able to evaporate Rb down to tens of μK. By adding the plug, we were able to evaporate Rb down to below 1 μK.

Then we studied Li response in the spherical quadrupole trap with and without the plug beam. We measured Li life time without the plug beam with t_{life} around 70 s. By adding the plug beam to plug the zero field Majorana hole, we still measured a similar life time. However, when we displaced the plug beam slightly away from the trap center, this lifetime decreased to 36 s. Meanwhile, for the cases with plug beam, the anisotropy went away and Li cloud became ergodic. This ergodicity turned out to be related to the cylindrical symmetry

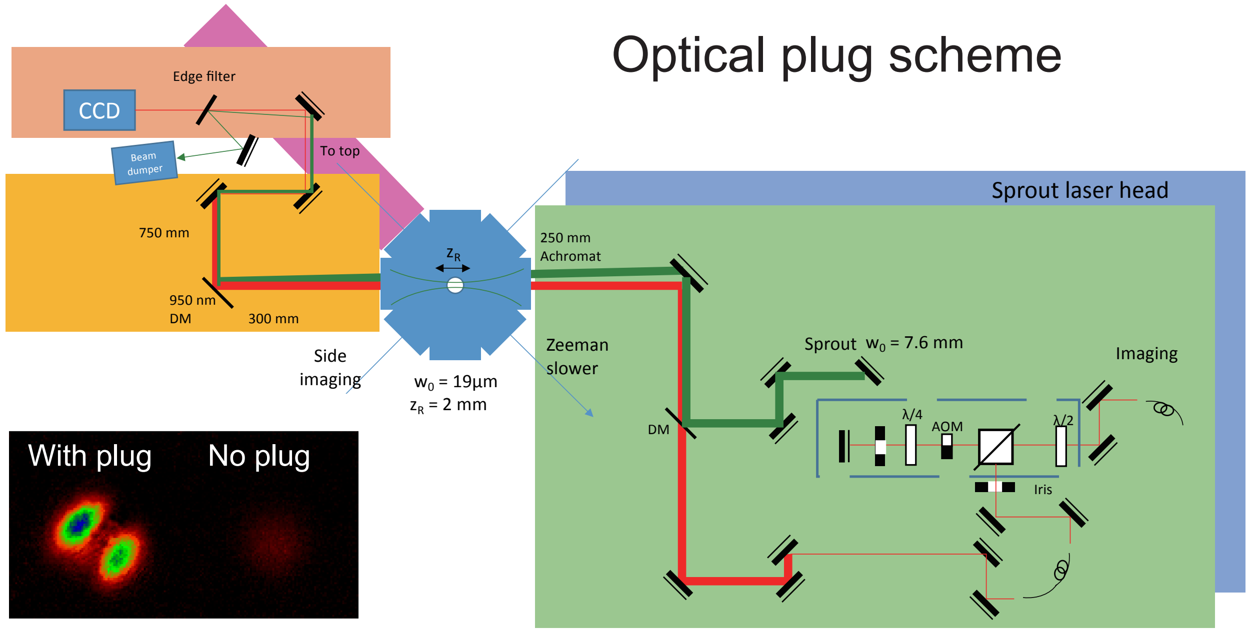

Figure 1.1: Optical Plug scheme. The blue rectangle represents the bottom breadboard where the green laser (Sprout) sits. After some beam shaping, this green laser is sent vertically through a periscope to an elevated breadboard, shown in the graph by the green rectangle on top of the blue, whose optics are at the horizontal level of the experimental chamber, where the green plug laser beam and the red imaging beam are combined by a dichroic mirror (DM) and sent through the 250 mm achromat into the vacuum chamber. The red imaging beam propagates through the chamber, finally impinges on the CCD camera. The double passed AOM setup is for time and frequency control of this imaging light. The green plug beam is focused down to the center of the spherical quadrupole trap, then propagates through the chamber, hits a edge filter in front of the CCD camera and is finally collected by a beam dumper. Inset Left: Rb atom with optical plug beam with a temperature of 3.7 μK. Inset Right: Rb atom after the same evaporation trajectory without optical plug.

of the spherical quadrupole trap. This topic was discussed in Chapter 4. Now we can explain the shrinking of lifetime by the fact that the non-ergodicity of Li cloud protected it against Majorana loss. There existed trajectories with non-zero axial angular momentum avoiding the Majorana hole area persisting forever in the non-ergodic case. With the Majorana hole plugged, although Li cloud became ergodic, the lifetime was not affected. On the other hand, when the plug beam was slightly displaced and could not prevent the Majorana loss, the life time of Li would decrease. However, when we introduced Rb into the spherical quadrupole trap, we observed that Li life time decreased dramatically to 13 s. We immediately realized that this was due to a tiny leakage of laser light at Rb repump frequency which constantly produced Rb F = 2 atoms. After blocking the light carefully through turning off the AOM, detuning the frequency, together with a mechanical shutter, we were able to get rid of these F = 2 atoms. And, we enjoyed a lifetime increase to 50 s. This observation indicated a large inelastic cross section between F = 2 states Rb and F = 1 states Li. Meanwhile, we also observed a Li cloud shape change with Rb presence, serving as a signature of interaction between the two. This observation finally led to the work discussed in Chapter 4.

Single-sideband mixer

Another effort we made for this sympathetic cooling project was to increase the microwave power for Rb evaporation. Our investigation showed that the performance of Rb evaporation was still not saturated on microwave power. Therefore, an increase in microwave power could improve the efficiency of Rb forced evaporation, and, ultimately, helped with the sympathetic cooling process. Our microwave set-up involved a rf signal generator (NI PXI-5650), mixing with 7 GHZ LO (PLO-4000-06.80), up-converted to a frequency range near 6.8 GHZ Rb hyperfine splitting before being sent into a 40 dB microwave amplifier (AM53-6.8S-40-40) with 40 dBm saturation power. However, the output of this amplifier saturated at 37 dBm. We attributed this saturation to the multi-tone input. Although the frequency at the local oscillator was well suppressed, similar power at two side-bands both seeded the amplifier. A suppression of the useless sideband could in principle increase the useful seed power and thus, seed the amplifier better. Therefore, our first effort was to replace the common used mixer to a single side-banded mixer (SSM), which could provide a single-sideband suppressed carrier output.

The scheme of SSM is shown in Fig. 1.2 a[5]. A lower sideband (LSB) or upper sideband (USB) output can be selected by choosing which I port to drive with the IF signal. The idea behind it is shown in Fig. 1.2 b. SSM includes two mixers, two quadrature power dividers and one in-phase power dividers. In any mixer, the phase angles of its RF and LO input signals are conserved during the mixing process. Therefore, the phase of IF port equals to the sum of the RF and LO input phase angles, multiplied by their respective harmonic coefficients, m and n. Thus we have phase angle equal to $m\theta_R + n\theta_L$ for an IF frequency of $mf_R + nf_L$. Now let's examine I_1 output as an example:

$$\begin{aligned} I_1 &= \frac{1}{2}(I_1' + I_2'\angle\frac{\pi}{2}) \\ &= \frac{1}{2}(I_{mn} + I_{mn}\angle(m+1)\frac{\pi}{2}) \\ &= \begin{cases} I_{mn} & \text{m = -1, n = 1, } f_{IF} = f_L - f_R \\ 0 & \text{m = 1, n = -1, } f_{IF} = f_R - f_L \end{cases} \end{aligned} \tag{1.1}$$

The similar argument applies to I_2 output. To implement this idea in lab, we used a quardrature hybrid coupler from Werlatone (QH8859-102) and a IQ mixer from Marki (MLIQ

---

[5] SSM discussion is based on a Tech-note from WJ Communications, Inc.

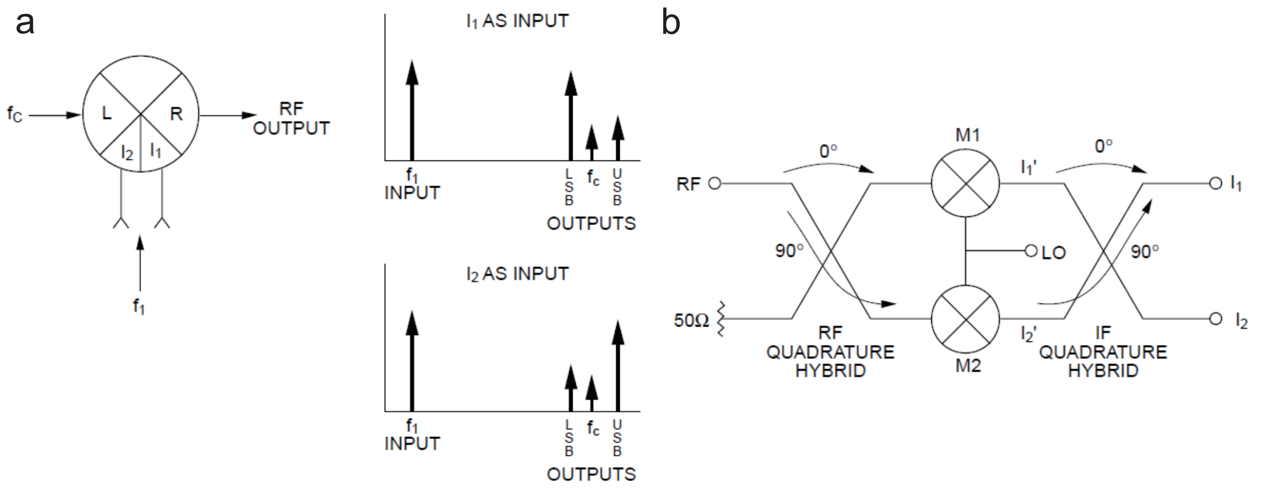

Figure 1.2: Single sideband mixer. (a) The scheme. (b) Block diagram.

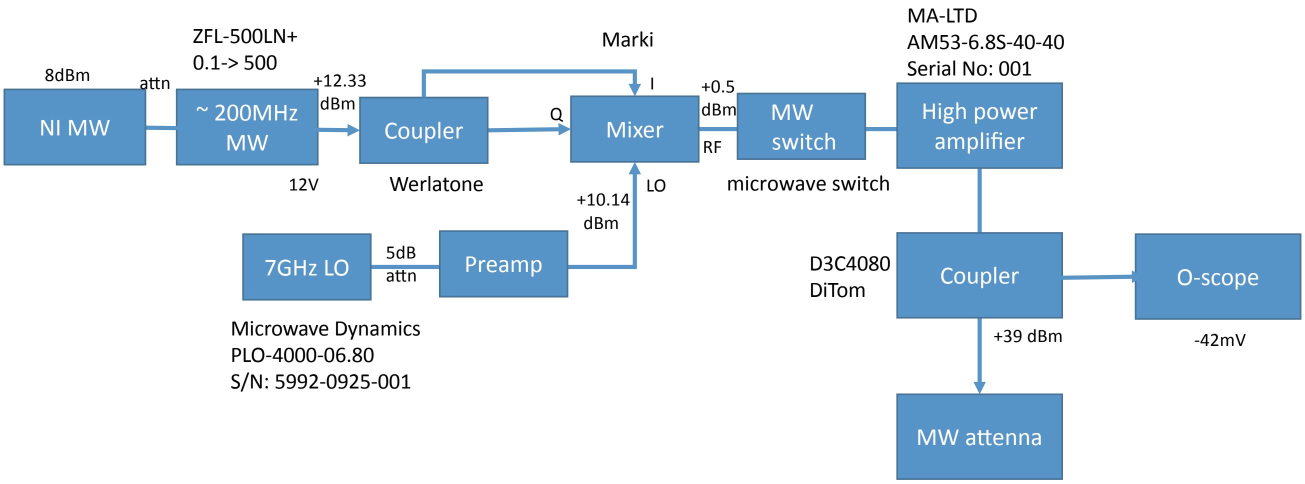

Figure 1.3: Block diagram for the microwave setup for Rb.

- 0416), shown in Fig. 1.3. With this implemented, we were able to increase the 37 dBm output to 39 dBm ouput.

The third effort we made to increase the microwave power by replacing the amplifier to one with 46 dBm saturation power(AM43-6.7-7.2-40-46). With SSM, we were able to achieve a 45 dBm final output power. With the increased microwave power, indeed, we were able to improve the efficiency of Rb forced evaporation through shrinking the total evaporation time while achieving larger atom number at each evaporation stage. However, as documented in Chaper. 4, we were not able to implement sympathetic cooling for Li by Rb bath due to the fact that the interspecies cross section turned out to be way smaller compared to our initial expectation.

With this small cross section, we started to suspect our way to calculate the cross section between the two in $|F=1, m_F=-1\rangle$ from the known singlet and triplet scattering length. After some literature searching, I ended up finding quantum defect theory was a standard method for our purpose from J. P. Burke's thesis [23–25]. Quantum defect theory treats scattering problems by dividing the inter-atomic potential into the long range part and short range part. For the long range part, the collisions are described by a single channel and the potential by the van der Waals interaction. Scattering in this potential can be treated exactly. For the short range part, the collision involves multiple channels while atomic motion in the deep short-range potential is almost independent of collisional energy and applied field. Scattering is treated by quantum defects. The value of these quantum defects could be determined by fitting the theoretical model to experimentally measured Feshbach resonances. My advisor, Dan, immediately bridged us with a theorist, Prof. Chris H. Greene. Chris generously shared his notebook on LiRb calculation with us. It turned out the theory predicted a even smaller cross section between the two compared to our measurement. Collaborating with Chris and his student, Yimeng Wang, we worked together to lessen the tension between our experiment and theory. This adventure is documented in Chapter 4.

1.6 Li Rb bichromatic dipole trap approach

At the end of 2017, we decided to abandon the idea of sympathetic cooling of Li by Rb in a plugged spherical quadrupole trap. This period also brought some changes in laboratory personnel: Shun Wu returned to China to assume a professorship position, while a new student, Aaron Smull, and, shortly afterwards, a new postdoc, Joshua Isaacs, joined Li - Rb efforts. We started to explore the possibility of all-optical approach to cool both species down to quantum degeneracy. The idea was to overlap two optical dipole traps, one formed with light at 1064 nm wavelength, and the other formed with light at 767 nm wavelength. With the high density in the dipole trap, we were hoping to get sympathetic cooling of Li by Rb in this bichromatic optical dipole trap [26]. Our first step was to create the 1064 nm wavelength dipole trap and load atoms into this trap directly from the molasses. For this purpose, we purchased a multimode high power laser amplifier from IPG (IPG YLR-100-1064-LP). While I was learning to catch Li and Rb in a single beam dipole trap formed by this multimode laser, Aaron, under the supervision of Josh, started to build the 767 nm laser system for this bichromatic trap. It turned out that both Rb and Li molasses were automatically working in the dipole trap. With 10 W power focused to the atomic cloud with a waist of 34 μm, we were able catch about 2 $\times 10^5$ Li at a temperature of around 36 μK and about 2 $\times 10^6$ Rb at a temperature of around 87 μK. To enhance the density in trap more, we added a second beam to form a cross dipole trap. With this cross dipole trap, we were able to achieve Rb BEC by this all optical approach. However, this multimode laser caused trouble. We found that the trapping laser light was causing stimulated Raman scattering [27, 28], which caused Rb atoms, initially pumped into the F=1 hyperfine level at the end of polarization gradient cooling, to be transferred into the F=2 hyperfine level. Most problematically, inelastic collisions of these excited-hyperfine-state Rb atoms with Li atoms caused the Li atoms to be rapidly lost from the trap. We found a similar problem arose from exposure of atoms to our 767-nm-wavelength light. Due to the fact that it was fairly close to 780 nm, the spontaneous Raman scattering could generate F = 2 Rb, depleting Li atom again. With pointing stability issue of the bichromatic trap, we finally decided to abandon this approach.

At this point, all of us, including my advisor, lost confidence in this old machine. I started to accept the fact that I could not achieve our initial goal: to bring both species down to quantum degeneracy. Aaron and Josh started to design the second generation machine of Li-Rb experiment. I started to think about ideas which could be done using these optically co-trapped Li - Rb thermal mixtures. From the communication and interaction with Chris Greene and Yimeng Wang, I realized the fact that the spin-dependent interaction between Li-Rb was pretty appreciable although they had a small spin-independent interaction compared to other bi-alkali mixtures. The pioneering work done in Dajun Wang group on heterospinor physics in Na-Rb mixtures motivated me a lot [29]. Similar physics should be able to see in Li - Rb system. This adventure was documented in Chapter 5.

1.7 Thesis structure

This thesis is structured chronologically. Chapter 2 focuses on the efforts in condensing magnons for our E4 magnon series. Chapter 3 documents the changes we made to incorporate Li into a Rb BEC machine. Chapter 4 discusses our results in measuring the interspecies cross section in a spherical quadrupole trap. Finally, Chapter 5 discusses our results in the spin-dependent interaction between Li and Rb.

Chapter 2

Condensing magnons in a box-like potential

Presented in this chapter is our efforts in studying the spin excitations, magnons, supported by the F = 1 ferromagnetic ^{87}Rb Bose-Einstein condensate (BEC). This work is the successor of our two previous study on the same topic, described in Ed's [1] and Ryan's thesis [2], and has been published [30].

Here we will first briefly discuss the properties of magnons. For more detailed discussion, please refer to Eds' thesis [1]. Then we discuss the phenomenon of magnon condensation. There we make a direct analogy between a gas of magnons and a gas of bosons, as well as between magnon condensation and Bose-Einstein condensation. This helps bridge the intuition from a regular BEC formed by real particles to a BEC formed by quasi-particles. Next, we examine the potential these magnons see. Interestingly, it turns out that these magnons behave like free particles propagating in a box-like potential. The signature of this box-like potential is probed experimentally through the spatial distribution of non - condensed magnon gas and the critical point of condensation. After condensing the magnons, we study the resultant quasi-condensate by probing the transverse magnetization, where we observe vortex-like spin texture in this quasi-condensate. Finally, we study the thermalization of this quasi-condensate.

2.1 What is a magnon?

Collective spin excitations from the magnetic order in a magnetic material are manifested by spin waves and their quanta, magnons. In Landau theory of phase transition, this kind of low energy excitation, called Nambu-Goldstone boson, is dictated by broken symmetries. Here we explain this concept with our experimental system.

Our research object is the F = 1 ferromagnetic BEC formed by ^{87}Rb . The Hamiltonian of this system respect both the phase symmetry, U(1), and rotational symmetry, SO(3). The ground state, the ferromagnetic BEC, breaks both in a way that a BEC breaks the phase symmetry while the ferromagnet breaks the rotational symmetry. The former leads to a Goldstone boson, called phonon, the quantum related to density excitations with linear dispersion. The latter leads to our research topic, the magnon, with quadratic dispersion. The story is actually more complicated. In Ref. [31], a detailed study on the relationship between the number of Nambu-Goldstone boson and the number of broken generators shows that they are not equal to each other for system without Lorentz invariance. For Heisenberg ferromagnet, there are two broken generators leading to only one Goldstone Boson with quadratic dispersion. Eds' work [32] shows a nice interferometry measurement confirming this quadratic dispersion in our system.

Now we derive magnons by adding spin fluctuations to the ground state wavefunction through applying an infinitesimal spin rotation:

$$\Psi_{magnon} = \sqrt{n} R(\phi, \theta, 0) \begin{pmatrix} 1 \\ 0 \\ 0 \end{pmatrix} \xrightarrow{\theta << 1} \sqrt{n} \begin{pmatrix} 1 \\ \frac{1}{\sqrt{2}} \theta e^{i\phi} \\ 0 \end{pmatrix} \tag{2.1}$$

Here $R(\phi, \theta, 0) = e^{-iF_z \phi} e^{-iF_y \theta}$, with ϕ, θ Euler angles and F_z, F_y spin - 1 matrices. From Eq. 2.1, we can see this spin fluctuation information is encoded in $|0\rangle$ atom. For this reason, in our system, with atoms initially prepared in a longitudinally magnetized state, we can typically identify atoms in the $|0\rangle$ Zeeman sublevel as being magnons. This identification is relevant, for example, when imaging the magnon distribution selectively.

2.2 Magnon condensate

In Eds' work [32], we show we are able to create magnons and make a nice calibration of its dispersion. Now we ask the question whether we are able to condense the magnon gas. Unlike a typical Bose - Einstein condensate where real particles are condensed into the ground state, in our system, magnon condensate is a spin superfluid phase coherent state formed by quasi-particles. To have a better intuition on magnon condensation, we make a direct comparison between Bose gases and magnon gases, as well as their condensates. For Bose gas, the conservation of atom number leads to a charge conservation described by U(1) symmetry. When the system is driven across the BEC phase transition, the ground state (BEC) breaks the U(1) symmetry by picking up a definite phase, with an emergence of non-zero mean field ground state wavefunction $\langle \Psi(\boldsymbol{r}) \rangle$, which serves as the order parameter of this phase transition. For magnon, instead of the number conservation, we have total magnetization conservation, leading to rotational invariance described by O(2) symmetry[1]. After the system is driven across the magnon BEC phase transition, the ground state (magnon BEC) breaks O(2) symmetry by developing a non-zero mean-field transverse magnetization $\langle M_x + iM_y \rangle$, which serves as the order parameter of this phase transition. The following Table 2.1 shows a detailed comparison between the two.

---

[1] In our ferromagetic spinor BEC system, we have SO(2) spin-gauge coupled rotational symmetry[33]

Therefore, to study this magnon condensate, we need to create magnons and then, drive them through the magnon-BEC phase transition. Finally, we should figure out a way to study the order parameter, transverse magnetization. Figure. 2.1 shows our experimental sequence. Our experiment starts with a ^{87}Rb ferromagnetic BEC prepared in the $|F=1, m_F=-1\rangle$ state held in a state-independent optical dipole trap. The temperature of the gas is controlled through evaporation cooling by the depth of the trap. At high trap depth with gas temperature ranging from $T_i = 80$ nK to 140 nK, we control the number of magnons pumped into the system by varying the time duration of the rf pulse. After holding this spin-mixed gas at constant temperature for 2.5 seconds, allowing for thermalization of the magnon gas, we lower the trap depth in 5 s to decrease the system's temperature. The lowest temperature achieved in our experiment is 30 nK with a trap depth of 122 nK, with trap frequency $\omega_{x,y,z} = 2\pi$ (23, 8.8, 160) s^{-1}. By increasing the initial magnon number pumping into the system, we are able to drive the magnon gas across the BEC transition. We probe the momentum distribution across the phase transition through momentum space focusing, a technique documented in detail in Ryan's thesis [2]. In addition, we probe the order parameter, transverse magnetization, across the phase transition, through imaging simultaneously the spatial distribution of the three Zeeman sublevels after applying $\pi/2$ pulse. The details on the transverse magnetization measurement will be recorded later in this chapter.

Bose gas	**Magnon**
Particles	Spin excitations(Bosonic quasiparticles)
Boson number N	Spin component M_z
Charge conservation U(1)	Rotational invariance O(2)
Wave function $\langle\Psi(\boldsymbol{r})\rangle$	Transverse magnetization $\langle M_x + iM_y\rangle$
BEC of Bose gas	**BEC of magnons**
Break U(1)	Break O(2)
Emergence of nonzero $\langle\Psi(\boldsymbol{r})\rangle$	Emergence of nonzero Transverse magnetization $\langle M_x + iM_y\rangle$

Table 2.1: Comparison between Bose and magnon gases, and their condensation at low temperature.

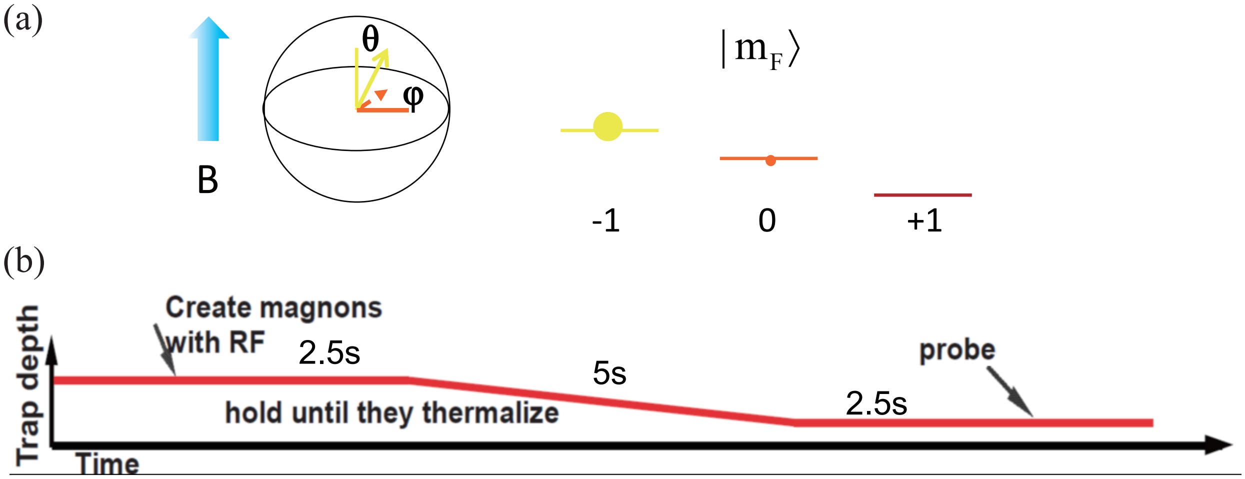

Figure 2.1: Experimental sequence to condense magnons. (a) The system is initialized in a spin-polarized state $|F = 1, m_F = -1\rangle$, and then a short rf pulse is applied to rotate the spin to create magnons. (b) Experimental sequence. After the creation of magnons, the spin-mixed gas is held in the dipole trap for 2.5 s, allowing for thermalization of the magnon gas. Then the dipole trap depth is lowered in 5 s for evaporation to decrease the system's temperature. Holding the mixture gas in this lower trap for 2.5 s, either the momentum distribution of magnon gas or the transverse magnetization is probed.

2.3 Magnons in a box

Boxlike potential

Now we study the living environment of magnons in our system. Due to the precise cancellation of the trapping potential and the mean-field repulsion of the majority condensate, magnons see a flat potential. This statement can be understood by the following argument. The effective potential V_{eff} magnons see is a sum of the harmonic trapping potential $V(\mathbf{r}) = \frac{1}{2}(m\omega_x^2 x^2 + m\omega_y^2 y^2 + m\omega_z^2 z^2)$ and the mean field repulsion $g_{01}n_1$. Here g_{01} denotes the coupling constant between atoms in states $|0\rangle$ and $|-1\rangle$, and n_{-1} denotes density of the majority condensate in the state $|-1\rangle$. Under Thomas-Fermi approximation, we have $n_{-1} = \max\left(\frac{\mu_{-1}-V}{g_{11}}, 0\right)$. Here μ_{-1} is the chemical potential of the majority condensate, and g_{11} is the coupling constant within the condensate. With the rotational symmetry in this F = 1 spinor gas, we have $g_{01} = g_{11}$. Therefore, we have:

$$V_{eff} = V + g_{01}n_{-1} = \max(V, \mu_{-1}) \tag{2.2}$$

The box shape is determined by the condensate, and thus is elliptical with three axis R_x, R_y and R_z, which are the Thomas-Fermi radii of the majority condensate. Figure. 2.2 shows a scheme for this effective potential and elliptical box. As magnons are quasi-particles with a magnetic moment equal in magnitude to atomic magnetic moment [32], any residual

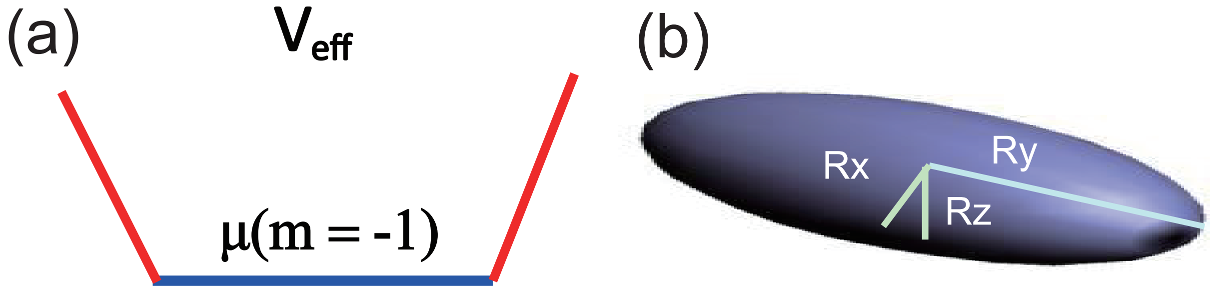

Figure 2.2: (a) Effective potential $V_{eff} = V + g_{01}n_1 = \max(V, \mu_{-1})$. (b) 3D elliptical box with $(R_x, R_y, R_z) = (21, 54, 3)$ μm.

magnetic gradient/curvature can affect their distribution. In our experiment, the gas is exposed to a 177 mG magnetic field and we are able to control the field such that it is uniform to about 10 μG within the condensate.

Boxlike potential signature: Position/Momentum-space distribution

We first consider position-space distribution of non-degenerate magnon gas in this effective potential. When $k_BT \ll \mu_{-1}$, this effective potential approaches a hard-wall box. With uniform density inside this elliptical hardwall box, the column density of magnons n_{col}, integrated along the imaging axis (z), is proportional to $\max(1 - x^2/R_x^2 - y^2/R_y^2, 0)^\beta$, with $\beta = 0.5$. Here $R_{x,y,z} = (\frac{2\mu_{-1}}{m\omega_{x,y,z}^2})^{\frac{1}{2}}$. On the other hand, for the majority condensate under Thomas-Fermi approximation, the column density has similar math expression as magnons in a hardwall box with a different exponent $\beta = 1.5$. Both deviate from that of a harmonically-trapped critical Bose gas, which is proportional to $g_2(e^{-\frac{x^2}{2\sigma_x^2}-\frac{y^2}{2\sigma_y^2}})$, with $\sigma_{x,y} = (\frac{k_BT}{m\omega_{x,y}^2})^{\frac{1}{2}}$.

In our experiment, our coldest sample is with k_BT/μ_{-1} around 0.7. We apply a short microwave pulse to selectively drive magnons from $|F = 1, m_F = 0\rangle$ to F $= 2$ manifold and then use resonant imaging light to image the atomic spatial distribution. For comparison, with the same detection method, we image the spatial distribution of the majority condensate. For the former, the data fits best to the elliptical hardwall box expression. The latter confirms the Thomas Fermi distribution. We thus conclude that thermal magnons live in a 3D box. Fig.1 of Ref. [30] shows the comparison of thermal magnon spatial distribution and the majority condensate.

The shape of the container for magnons can also affect the momentum distribution of the gas near the critical point. To calculate the momentum distribution in this effective potential, we integrate over position in phase space:

$$n_{\mathrm{th}}(p) = n_{\mathrm{in}}(p) + n_{\mathrm{out}}(p) = \frac{1}{h^3}\int \frac{1}{e^{(\frac{p^2}{2m}+V_{\mathrm{eff}})/k_BT}-1}d\mathbf{r} \tag{2.3}$$

Here $n_{\mathrm{in}}(p)$ is integrated within the majority condensate, n_{out} is integrated outside the majority condensate. We do a coordinate transformation: $x = X\sqrt{\frac{\hbar\overline{\omega}}{m\omega_x^2}}$, $y = Y\sqrt{\frac{\hbar\overline{\omega}}{m\omega_y^2}}$, $z = Z\sqrt{\frac{\hbar\overline{\omega}}{m\omega_z^2}}$. Then V($\mathbf{r}$)=V(R)=$\frac{1}{2}\hbar\overline{\omega}R^2$, where $\overline{\omega} = (\omega_x\omega_y\omega_z)^{1/3}$. With the assistance of this coordinate transformation, it is straightforward to evaluate this integral. Here we report the column momentum density of magnons near the critical point:

$$\begin{aligned} n_{\mathrm{in}}(p) &= (V_{\mathrm{in}}/\lambda_{\mathrm{dB}}h^2)g_{1/2}\left(z(p)\right) \\ n_{\mathrm{out}}(p) &= \lambda_{\mathrm{dB}}^{-1}h^{-2}\left(2\pi\right)^{3/2}\bar{\sigma}^3\sum_{j=1}^{\infty} z(p)^j\,\frac{2\sqrt{j\nu}+e^{j\nu}\sqrt{\pi}\,\mathrm{erfc}(\sqrt{j\nu})}{j^2\sqrt{\pi}} \end{aligned} \tag{2.4}$$

Here $V_{\mathrm{in}} = 4\pi\bar{R}^3/3$ is the condensate volume. $\bar{R} = \sqrt{2\mu_{-1}/m\bar{\omega}^2}$ is the geometric mean Thomas-Fermi radius with $\bar{\omega}$ the geometric mean trap frequency. $\lambda_{\mathrm{dB}} = (2\pi\hbar^2/mk_BT)^{1/2}$ is the thermal deBroglie wavelength, $\bar{\sigma} = \left(k_BT/m\bar{\omega}^2\right)^{1/2}$ is the geometric mean thermal radius in the harmonic trap, $\nu = \mu_{-1}/k_BT$, and $z(p) = \exp\left((\mu - p^2/2m)/k_BT\right)$ with μ the magnon chemical potential, which goes to zero at critical point. In the limit $\nu \to 0$, the sum on the second line above equals $g_2(z(p))$, yielding the result for a harmonically trapped gas. We conclude that as the effective potential magnons see becomes flatter, the momentum distribution of magnons near the critical point becomes peakier.

We probe the momentum distribution of magnons near critical point through our standard probe technique: momentum space focusing. Through imaging the momentum distribution of magnons as we drive across phase transition, we are able to determine the critical point position and thus, select out the momentum - space image just below the condensation transition. As shown in Fig.1 of Ref. [30], this distribution is indeed peakier than predicted for atoms in harmonic trap and is consistent with the expected momentum-space distribution for magnons in a flat effective potential.

It is interesting to compare our work to recent experiments where scalar BEC is studied in a box potential [34, 35]. In those experiments, the box potential is formed by a repulsive potential for the atoms, where the atomic cloud is confined to the dark region surrounded by the optical barriers. Gravitational force is canceled by a magnetic field gradient for atoms in a state with non-zero magnetic moment. The momentum distribution was also examined near the critical point, and a similarly sharply peaked momentum distribution was observed.

Boxlike potential signature: Critical magnon number

The shape of the container can affect the density of states of particles inside, and thus lead to different critical magnon number prediction for the same $\frac{k_BT}{\mu_{-1}}$. Here we calculate the critical magnon number in this effective potential. As $k_BT \gg \hbar\omega_{x,y,z}$, a semi-classical approach is applied to obtain the critical density.

$$n_{th}(\mathbf{r}) = \frac{1}{\lambda_{dB}^3} g_{\frac{3}{2}}(z(\mathbf{r})) \tag{2.5}$$

where $\lambda_{dB} = (2\pi\hbar^2/mk_BT)^{1/2}$, $z(\boldsymbol{r})$=$exp(-V_{\text{eff}}/k_BT)$. The Bose function is given by $g_{\frac{3}{2}}(z) = \sum_{j=1}^{\infty} \frac{z^j}{j^{3/2}}$.

$$N_{\text{critical}} = N_{\text{in}} + N_{\text{out}} = \int n_{th}(\mathbf{r}) d\mathbf{r} \tag{2.6}$$

Here N_{in} is critical magnon number within the majority condensate, N_{out} is critical magnon number out of the majority condensate. Here we report the final result after integration:

$$\begin{aligned} N_{\text{in}} &= \lambda_{\text{dB}}^{-3} V_{\text{in}} \zeta(3/2) \\ N_{\text{out}} &= \lambda_{\text{dB}}^{-3} \, (2\pi)^{3/2} \, \bar{\sigma}^3 \times \sum_{j=1}^{\infty} \frac{2\sqrt{j\nu} + e^{j\nu}\sqrt{\pi}\,\text{erfc}(\sqrt{j\nu})}{j^3\sqrt{\pi}} \end{aligned} \tag{2.7}$$

with $\zeta(x)$ the Riemann zeta function. In the limit $\nu \to 0$, $\sum_{j=1}^{\infty} \frac{2\sqrt{j\nu}+e^{j\nu}\sqrt{\pi}\,\text{erfc}(\sqrt{j\nu})}{j^3\sqrt{\pi}}$ equals $\zeta(3)$, yielding the critical number of bosons in a harmonic trap.

In our experiment, we study the variation of the critical magnon number with temperature. At each temperature T_{f}, ranging from 30 to 114 nK, we examine the momentum distribution of the $m_F = 0$ atoms as a function of total magnon number. This momentum distribution is measured by the momentum space focusing technique across the magnon BEC transition, shown in Fig. 2.3 a.

We use the following procedure to determine critical magnon number from the experimentally measured momentum-space column density images. Excluding data from the central region of the image, we fit the momentum-space column density to several parametrizations of the distribution of a non-condensed Bose gas at variable magnon chemical potential and temperature T_{f}. These parametrizations include $g_\alpha\left(z(\mathbf{p})\right)$ with α chosen among several value, which describes the expected momentum distribution of bosons in various power-law potentials, and also the distribution expected for bosons trapped in the effective potential V_{eff}. Here, $z(\mathbf{p}) = \exp\left[(\mu - p^2/2m)/k_BT_{\text{f}}\right]$ with $\mu = \mu_0 - \mu_{-1}$ being the magnon chemical potential referenced to μ_{-1} and ignoring the Zeeman energy ($\mu = 0$ at the magnon condensation transition), and $\mathbf{p}$ being the momentum in the imaged plane. The size of the excluded region is chosen such that these functions give about the same temperature. The magnon condensate number is then determined by subtracting the fitted function from the observed distribution and summing over the image, including the central region. This magnon condensate number rises linearly from zero with increasing total magnon number above a number $N_{\text{mag,c}}$ that we identify as the critical magnon number for condensation. Different parameterizations of the non-condensed magnon distribution give critical magnon numbers that vary by around 10% at the same T_{f} for our coldest samples, shown in Fig. 2.3 c inset.

In Fig. 2.3 c, we compare $N_{\mathrm{mag,c}}$ to predicted values for ideal-gas Bose-Einstein condensation in one of three potentials: a harmonic trapping potential, a hard-walled box potential with a volume matching that of the $m_F = -1$ condensate, and the effective trapping potential V_{eff}, using the experimentally determined $\omega_{x,y,z}$, μ_{-1}, and T_{f} at each setting. The measurements agree well with predictions based on the condensation of magnons in the effective potential V_{eff}. At low temperature ($k_B T_{\mathrm{f}} \ll \mu_{-1}$), the measured critical magnon number tends toward that predicted for a hard-walled box potential while at high temperatures ($k_B T_{\mathrm{f}} \gg \mu_{-1}$), $N_{\mathrm{mag,c}}$ tends toward the prediction for a harmonically trapped gas, as expected.

Here we comment on the importance and advantage of box potential. While ultracold atomic systems serve as a clean and controllable experimental platform to be able to make direct comparison with theory, the gas is usually trapped in a harmonic trap in experiment. On the other hand, the theory is usually dealing with spatially uniform systems. One way to get around it is to use local density approximation (LDA). However, it could be limited, especially for studies of critical behavior where the correlation length diverges at critical point. There is beautiful recent work done on critical behavior of Bose gas trapped in a box potential formed optically [36]. Compared to them, our box for magnons is nature-made and thus we are able to study critical behavior of magnons in a box-like potential without too many technique hurdles.

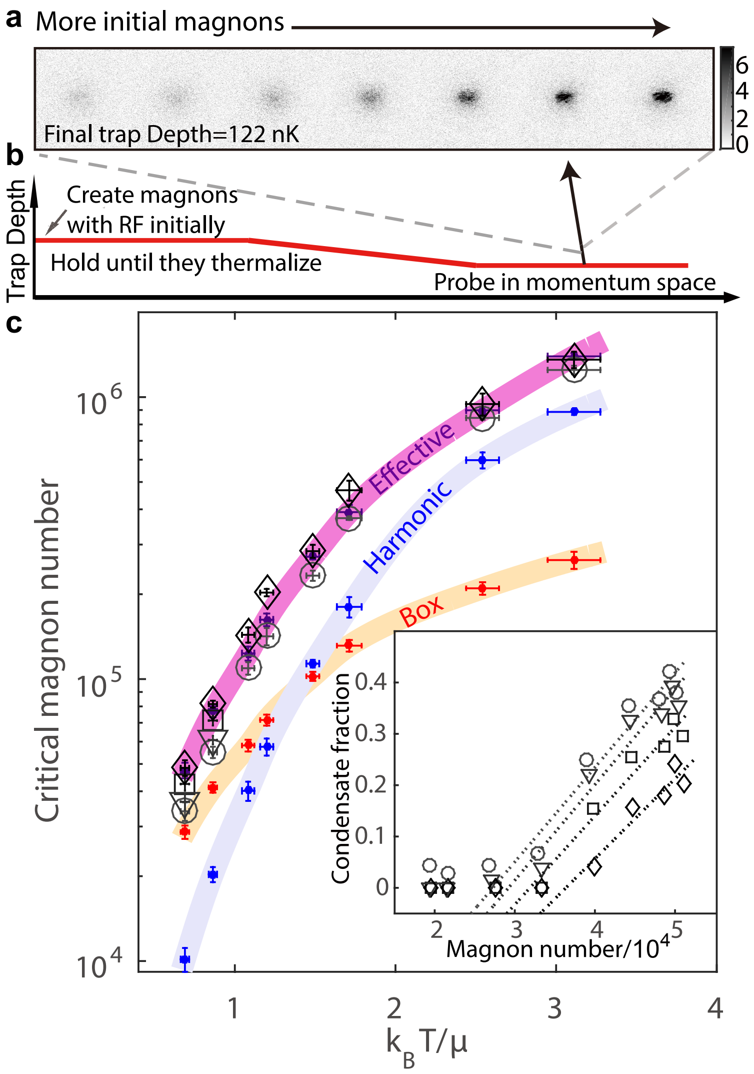

Figure 2.3: Momentum space magnon gas distribution across the condensation phase transition. This phase transition is achieved by creating more magnons at high trap depth with longer rf pulse. Then the trap is lowered, with the final temperature of the magnon gas T_f determined by this final trap depth. (a) Momentum distribution of magnons through phase transition at a final trap depth 122 nK. (b) Corresponding experimental sequence. (c) The measured critical magnon number $N_{\mathrm{mag,c}}$ (black markers) is compared to the expected value (blue, red, purple points, respectively) for magnons in a harmonic, box (size defined by condensate volume), and V_{eff}. Shaded lines are guides to the eye. Error bars on model predictions account for statistical uncertainties in experimental parameters. Inset: The magnon condensate number, shown for $k_B T_\mathrm{f}/\mu_{-1} = 0.7$, is the integrated residual above the fits to the non-condensed magnon momentum distributions using one of four fit functions: $g_\alpha(z(\boldsymbol{\rho}))$ with $\alpha = 1$ (squares), 1.5 (triangles), or 2 (circles), or the predicted distribution in the effective potential (diamonds). A linear fit shows the magnon condensate number increasing linearly above $N_{\mathrm{mag,c}}$; error bars are statistical. Extracted measured critical magnon numbers from the four fitting functions are shown in the main plot (diamonds, squares, triangles, circles with a decrease in grayscale).

2.4 Transverse magnetization

In Sec. 2.2, we show that the transverse magnetization serves as the order parameter for magnon-BEC transition. Therefore, a measurement of transverse magnetization across the phase transition is required. For simplicity, we first focus on measuring a single component of transverse magnetization, $\langle M_x \rangle = n(\boldsymbol{r})\theta cos\phi$. Here $n(\boldsymbol{r})$ is the density of the majority condensate under the assumption $\theta \ll 1$, see Eq. 2.1. This measurement shows an emergence of nonzero transverse magnetization. However, it is inhomogeneous spatially. To have a better understanding of the resultant inhomogeneous magnon quasi-condensate, we then decide to directly measure the wavefunction by simultaneously measuring $\langle M_x \rangle$ and $\langle M_y \rangle$. Here $\langle M_y \rangle = n(\boldsymbol{r})\theta sin\phi$.

As discussed below, in certain experimental sequences, we chose to measure just one component of the transverse magnetization. For later experiments, a more complex experimental procedure was used to measure both components of the transverse magnetization. We discuss the types of analysis that we were able to perform with either experimental method.

$\langle M_x \rangle$: Across phase transition

To measure the magnetization, we image the atom population in the three Zeeman sub-levels through the absorptive spin-sensitive *in situ* imaging (ASSISI), where a short microwave pulse is applied to bring the population in F = 1 manifold to F = 2 manifold, and later a brief resonant optical pulse is applied to get absorption image. This microwave pulse is sensitive to the 124 kHZ Zeeman splitting in F = 1 manifold, and thus is state-sensitive. The short microwave only excites a small fraction of atoms from F = 1 manifold, and thus this method is almost non-destructive. A detailed description and calibration can be found in Eds' thesis [1]. With this tool, we are able to simultaneously image the *in situ* spatial column density of atoms in the three m_F sublevels in F = 1 manifold.

Specifically, we measure the transverse column magnetization $\langle \tilde{M}_x \rangle$ by applying a $\frac{\pi}{2}$ pulse and then imaging the atom column density in the three Zeeman sub-levels through ASSISI. $\langle \tilde{M}_x \rangle$ is extracted by the relationship $\langle \tilde{M}(\boldsymbol{r})_x \rangle = \tilde{n}(\boldsymbol{r})_{+1} - \tilde{n}(\boldsymbol{r})_{-1}$. Here $\tilde{n}(\boldsymbol{r})_{+1}$ and $\tilde{n}(\boldsymbol{r})_{-1}$ are column density for atoms in $|+1\rangle$ and $|-1\rangle$ states. Fig. 2.4 shows both the real space images and Fourier space power spectra of $\langle \tilde{M}_x \rangle$ across phase transition. The Fourier images are concentrated in a narrow and nearly isotropic ring with spatial wavenumber k_r around 17 μm, corresponding to the order parameter domain size. These domains are only observed for magnon number above the critical number, thus confirm an emergence of non-zero inhomogeneous transverse spin through the phase transition.

These inhomogeneous patterns, however, could be caused or distorted by optical aberrations. To eliminate this possibility, we experimentally prepare some known spin textures to benchmark our method. These spin textures is formed by first applying a short rf pulse to rotate the spin-polarized gas in $|-1\rangle$, then applying magnetic gradient to wind spin helix, finally applying the same rf pulse to interfere the phase winding into density patterns before

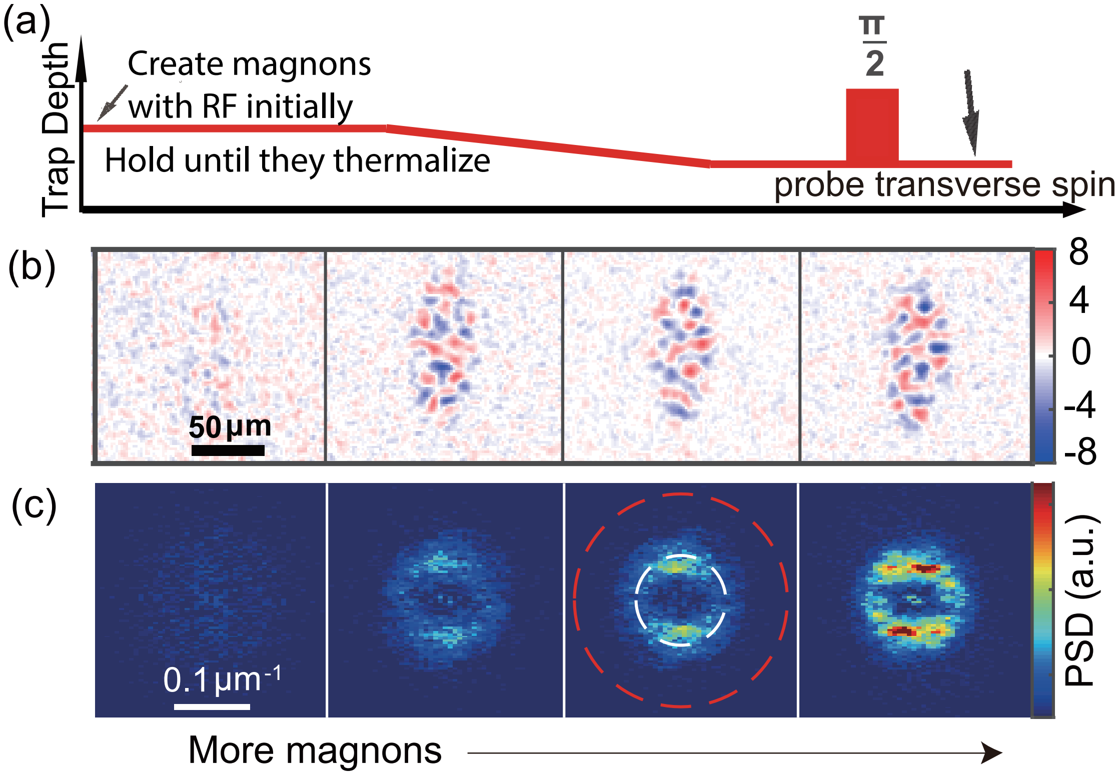

Figure 2.4: $\langle \tilde{M}_x \rangle$ measurement across phase transition. (a) Experimental scheme. (b) Real space images of $\langle \tilde{M}_x \rangle$ across phase transition. (c) Corresponding Fourier space power spectra across phase transition, averaged over 20 experimental repetitions. White dashed circle marks $\frac{2\pi}{k_r}$. Red dashed circle represents the imaging resolution.

imaging atom population in m_F sublevels with ASSISI. We can write down the wave function for this spin texture:

$$\Psi_{texture} = \sqrt{n} \begin{pmatrix} \frac{1}{2}(1+cos\theta)e^{-i\boldsymbol{k}\cdot\boldsymbol{r}} \\ -\frac{isin\theta}{\sqrt{2}} \\ \frac{1}{2}(-1+cos\theta)e^{i\boldsymbol{k}\cdot\boldsymbol{r}} \end{pmatrix} \tag{2.8}$$

By orienting the quantization axis through changing the bias field direction, we are able to make spin textures with different orientation $\hat{n_k}$. By changing the time duration for the applied magnetic field gradient, we are able to change the magnitude of $\boldsymbol{k}$. Therefore, these spin textures can be used as a test pattern for a imaging system. Actually, we extract the modulation transfer function (MTF) of our imaging system using these spin patterns. The similar MTF behavior for two orthogonally oriented test pattern rules out this possible optical aberrations, and confirms the validity of our method. Similar test pattern method with polarization contrast imaging method is well-documented in Jennie Guzman's thesis [37].

Probe transverse magnetization: Spin echo

To simultaneously measure $\langle \tilde{M}_x \rangle$ and $\langle \tilde{M}_y \rangle$, we add a second, carefully timed $\frac{\pi}{2}$ pulse, and then take *in situ* absorption images of the three Zeeman sublevels through ASSISI. To remove the inhomogeneous dephasing possibly coming from a static residual magnetic field gradient/curvature, we insert a π echo-pulse in-between the two $\frac{\pi}{2}$ pulse. In our experiment, we synchronize this pulse series to the 60 HZ AC line noise by upgrading our Cicero control software's Variable Timebase to the FPGA synthesized Variable Timebase (Opal Kelly FPGA board). This synchronization is crucial for us to be able to apply reliable π pulse. However, even with this synchronization, the experiment involving spin-echo pulses was only successful when conducted at night, when the magnetic field noise from building elevators and other sources was reduced. Fig. 2.6 shows this spin-echo sequence.

Before we apply this spin-echo method to study magnon quasi-condensate, we first calibrate this method through two test experiments. In the first experiment, we prepare a spin-polarized BEC in $|-1\rangle$, fix the time spacing τ between the first $\frac{\pi}{2}$ pulse and the π pulse, while vary the time spacing $\tau + \Delta\tau$ between the π pulse and the second $\frac{\pi}{2}$ pulse, and then monitor the population evolution in the three Zeeman sublevels. We are expecting to observe coherent oscillation in the Zeeman level population, with $|-1\rangle$ and $|+1\rangle$ states' population oscillating out of phase at Larmor frequency, and population in the $|0\rangle$ state oscillating in-between at twice of that frequency. Our test experiment confirms this expectation, suggesting our spin-echo method works fine, see Fig. 2.5. A similar experiment without spin-echo pulse shows randomly scattered data in the three Zeeman sublevels, instead of the nice oscillations, suggesting that, at the time scale of several ms, the limiting factor that scrambles the phase is static magnetic field noise.

In the second test experiment, we apply this spin-echo method to image known manually-made spin textures, which has been used for our imaging system calibration in previous sub-section. The procedure of winding spin textures for this purpose is as follows. We first prepare a spin-polarized gas in $|-1\rangle$ state. Then we apply a short rf pulse to tilt the spin slightly, such that creating a similar amount of atoms in $|0\rangle$ state as those in the magnon gas. Next, a magnetic field gradient is applied, whose orientation is controlled by re-orienting the quantization axis, and whose magnitude is controlled by varying the time of the applied gradient. Here we write down the wavefunction for this spin texture with $\theta \ll 1$:

$$\Psi_{texture} = \sqrt{n} \begin{pmatrix} 1 \\ \frac{\beta}{\sqrt{2}} e^{i\boldsymbol{k}\cdot\boldsymbol{x}} \\ 0 \end{pmatrix} \tag{2.9}$$

To image the magnetization of this spin pattern, we apply the first $\frac{\pi}{2}$ pulse after which we take an *in situ* image for $|-1\rangle$ state population. Then we apply a π pulse and take an *in situ* image for $|-1\rangle$ state distribution again. Then after a careful timing of $\Delta\tau$, we take *in situ* images for the atomic distributions in the three Zeeman sublevels. Here we play a trick on the measurement of $\langle \tilde{M}_x \rangle$. The atomic distribution in $|+1\rangle$ state after the first $\frac{\pi}{2}$ pulse equals to the distribution in $|-1\rangle$ state after the π pulse. Therefore, with two $|-1\rangle$

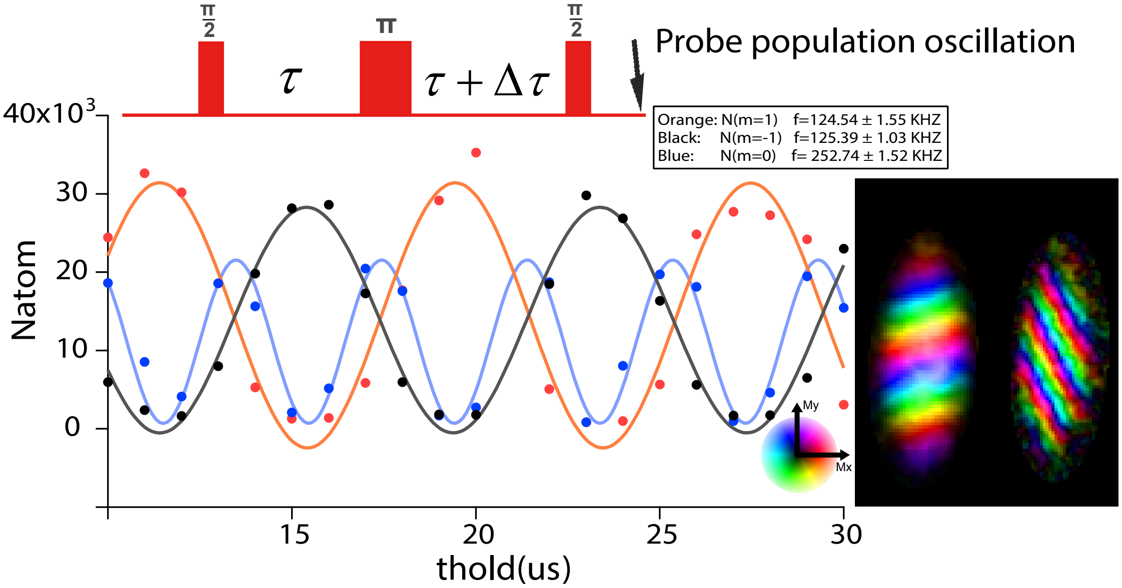

Figure 2.5: Spin echo: coherent population oscillation. The population in $|-1\rangle$ and $|+1\rangle$ states oscillates out of phase at Larmor frequency with $|0\rangle$ oscillates in-between at twice of the frequency. Inset: two examples for the known spin textures imaged by our spin echo method.

state images before and after the π pulse, we are able to reconstruct $\langle \tilde{M}_x \rangle$. This trick helps us shrinking τ, which is good against decoherence, because[2] only one image is needed to be taken per τ. Specifically, in our experiment, $\tau = 1.56$ ms with a π pulse length equal to 430 μs. Here we show the resultant spin textures imaged by our spin echo method for two different $|k|$ with different orientations in Fig. 2.5 inset, as well as a spin echo scheme for spin texture test experiment in Fig. 2.6.

Probe transverse magnetization: Magnon quasi-condensate

We then apply this spin echo method to measure the complete order parameter of magnon condensation. Instead of imaging the magnetization of a known spin texture as described in the previous sub-section, here we change our imaging object to the spatially inhomogeneous magnon quasi-condensate. The corresponding experimental sequence is shown in the inset of of Fig. 2.7 b. The resultant transverse column magnetization $\langle \tilde{M}_T(\mathbf{r}) \rangle$ of magnon quasi-condensate is displayed in Fig. 2.7 a, with hue and brightness representing orientation and amplitude, as indicated by color wheel. Here we briefly comment this measurement and the measurement results.

---

[2] The camera needs a finite amount of time to take a new image, the microwave takes a finite amount of time to shift to another tone.

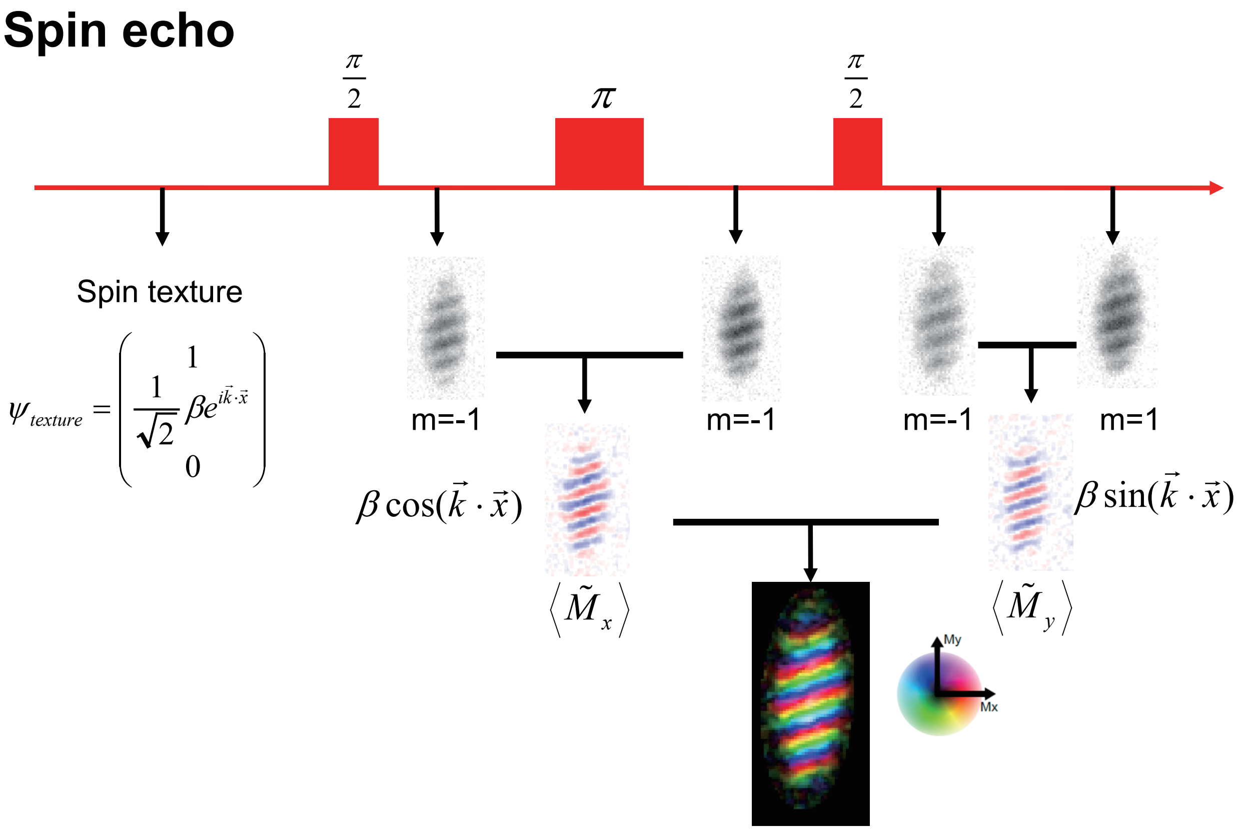

Figure 2.6: Visualize spin echo scheme for spin texture test. After the preparation of spin texture, we apply a $\frac{\pi}{2}$ pulse and then take an image for column density in $|-1\rangle$ state. Then, after a π pulse, we take a second image for column density in $|-1\rangle$ state. These two images are used to reconstruct $\langle\tilde{M}_x\rangle$. Next, after a careful timing, we apply a second $\frac{\pi}{2}$ pulse and take images for column density in $|-1\rangle$ and $|+1\rangle$ states. These two images are used to reconstruct $\langle\tilde{M}_y\rangle$. Finally, we combine $\langle\tilde{M}_x\rangle$ and $\langle\tilde{M}_y\rangle$ to get the total column transverse magnetization $\langle\tilde{M}_T\rangle$, with hue and brightness representing orientation and amplitude, as indicated by color wheel.

First, this measurement characterizes the emergent small population of magnon quasi-condensate interferometrically [3]. The signal from the small population of magnon quasi-condensate in the $|0\rangle$ state is amplified by a local oscillator, the majority condensate, through the relation $\langle M_T(\mathbf{r})\rangle = \langle M_x(\mathbf{r}) + iM_y(\mathbf{r})\rangle = \sqrt{2}\psi^*_{-1}(\mathbf{r})\psi_0(\mathbf{r})$. This measurement requires uniform phase for the majority condensate. We thus prepare our condensate through very gradual evaporation such that there is no vortex generated across the BEC phase transition,

---

[3] The fraction of all trapped atoms within the magnon condensate, determined from the transverse magnetization, varies from 1.8% to 3.7%. For identically prepared samples, from measurements of the magnon momentum-space distribution, we estimate this fraction to be 2.6%.

which is confirmed by our high resolution imaging system after a long time of flight (TOF).

Second, we measure the column transverse magnetization $\langle \tilde{M}_T \rangle$ with a relation $\langle \tilde{M}_T(\boldsymbol{\rho}) \rangle = e^{i\varphi(\boldsymbol{\rho})} \sqrt{2\tilde{n}_{-1,\mathrm{c}}(\boldsymbol{\rho})\tilde{n}_{0,\mathrm{c}}(\boldsymbol{\rho})}$. Here, $\tilde{n}_{m_F,\mathrm{c}}$ is the column density of the m_F component of the condensate, φ is the magnon condensate phase (up to a uniform offset), and $\boldsymbol{\rho}$ is the position in the imaged plane. This is an automatic result from absorption imaging method where the density of atomic cloud is integrated through the imaging axis z. The Thomas-Fermi radius R_z is around 3 μm, which is comparable to 3.7 μm spin healing length, indicating our quasi-condensate could be effectively 2D with respect to spin. This 2D expectation is confirmed by our measurements, where we see spin domains in our column-integrated images.

Third, as shown in Fig. 2.7 a, there are vortex-like singularities, around which the phase ϕ of the transverse magnetization winds around by $\pm 2\ \pi$. Fig. 2.7 b shows the phase winding along a path encircled the singularity region. Both the number of the singularities and the sign of phase winding vary randomly, confirmed by several repetitions of the experiment. We note here that these vortex-like features are not real vortexes, which induce a density depletion at the core region. Instead, these singularities can be identified as Mermin-Ho spin textures [38–40], in which the orientation of the magnetization spans a small cap about the longitudinal axis.

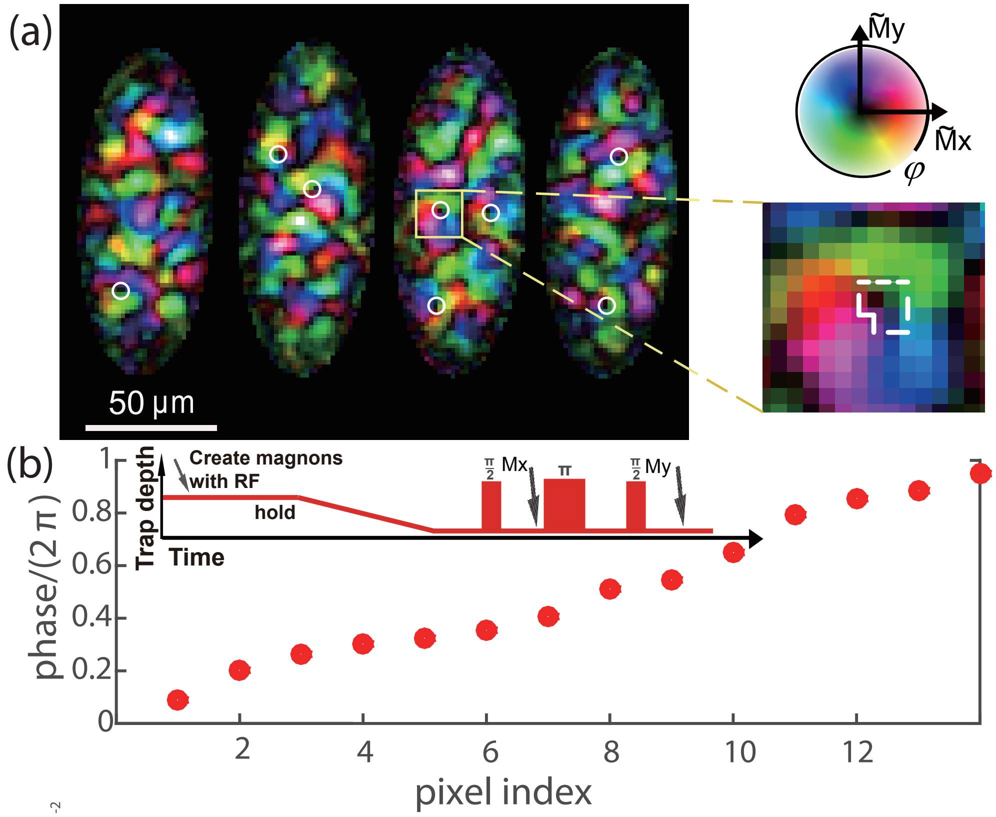

Figure 2.7: Magnon quasi-condensate. (a) Inhomogeneous transverse magnetization measured for four experimental repetitions, in coldest samples and with $\sim 10\%$ magnon fraction, with hue and brightness representing orientation and amplitude, as indicated by color wheel. Identified phase singularities are marked by white circles. The inset highlights one such singularity, with the dashed white line showing a path encircled the singularity. (b) Phase change of the magnon order parameter along the path encircled the singularity region, highlighted in the inset of (a). Inset: experimental sequence for measurements of the complete order parameter of magnon condensation.

2.5 Coarsening

From previous sections, we show that we are able to make magnon quasi-condensate with inhomogeneous transverse magnetization. Here we present our study on coarsening dynamics of this magnon quasi-condensate.

For a second order phase transition, as the system is driven across the phase transition, spontaneous symmetry breaking happens where system can end up with different choices of local vacuum, unless the critical point is traversed infinitesimally slowly. Near the critical point, the correlation length ξ increases and finally diverges at the critical point. Meanwhile, the relaxation time τ, or the time needed to reach equilibrium, increases and finally diverges at critical point. The latter is called "critical slowing down". Therefore, one can expect at some point near phase transition the system can no longer be adiabatic, resulting in the freezing of the order parameter, as well as the development of boundary defects after the phase transition. Kibble-Zurek theory [41–43] connects the domain size and the defect density to the quench rate and reveals the universality of this relationship, dictated by the corresponding fixed point, such as the symmetry that is broken and the dimension of the system. In recent years, the Kibble-Zurek mechanism has been extensively studied in cold atomic system[36, 44–48].

Here we present a short derivation of the domain size's dependence on the quench rate. Defining ϵ as a measurement of how close we are approaching critical point with $\epsilon = \frac{T-T_c}{T}$, near the critical point, we have

$$\begin{aligned} \xi &= \frac{\xi_0}{|\epsilon|^{\nu}} \\ \tau &= \frac{\tau_0}{|\epsilon|^{\gamma}} \end{aligned} \tag{2.10}$$

Here ξ is the correlation length, τ is the relaxation time, ν and γ are universal critical exponents. For mean-field theory, we have $\nu = \frac{1}{2}$, $\gamma = 1$. For F model(Renormalization group) applied for 3D U(1) symmetry, we have $\nu = \frac{2}{3}$, $\gamma = 1$ [49, 50]. In the Kibble-Zurek picture, we consider the situation where the temperature of a system is swept in time through the phase transition temperature. We then have $\epsilon = \frac{t}{t_Q}$ where t is the time with $t = 0$ being the time at which the phase transition is crossed, and $t_Q = \frac{t}{\epsilon} = T_c/(dT/dt)$ quantifies the rate at which the transition is crossed. Now we define v_ξ as the speed the order parameter needed to stay adiabatic as it is approaching critical point, and define s as the real speed of the system as it is approaching critical point. At time $t = \hat{t}$, $v_\xi = s$, indicating the system at the edge of being adiabatic and the freezing of the order parameter with finite domain size.

$$\begin{aligned} &v_\xi|_{\hat{t}} = s|_{\hat{t}} \\ &v_\xi|_{\hat{t}} = \frac{d\xi}{dt}|_{\hat{t}} = \frac{d\xi}{d\epsilon}\frac{d\epsilon}{dt}|_{\hat{t}} = \frac{\nu\xi_0}{|\epsilon|^{\nu+1}}\frac{1}{t_Q} \\ &s = \frac{\xi}{\tau}|_{\hat{t}} \\ &|\epsilon| = \left(\frac{\tau_0}{t_Q}\right)^{\frac{1}{1+\gamma}}\left(\frac{t}{\tau}\right)^{\frac{1}{1+\gamma}}|_{\hat{t}} = \left(\frac{\tau_0}{t_Q}\right)^{\frac{1}{1+\gamma}} \end{aligned} \tag{2.11}$$

Combining the expressions above, we obtain

$$\xi(\hat{t}) \propto \xi_0 \left(\frac{t_Q}{\tau_0}\right)^{\frac{\nu}{1+\gamma}} = \xi_0 \left(\frac{t_Q}{\tau_0}\right)^{d} \tag{2.12}$$

F model predicts d=$\frac{1}{3}$. In our experiment, we measure the domain size by the inverse length scale in Fourier space transverse spin image. By varying t_Q from 3 s to 18 s, we are expecting to see the domain size change by a factor of 1.8. However, our experiments shows there is no

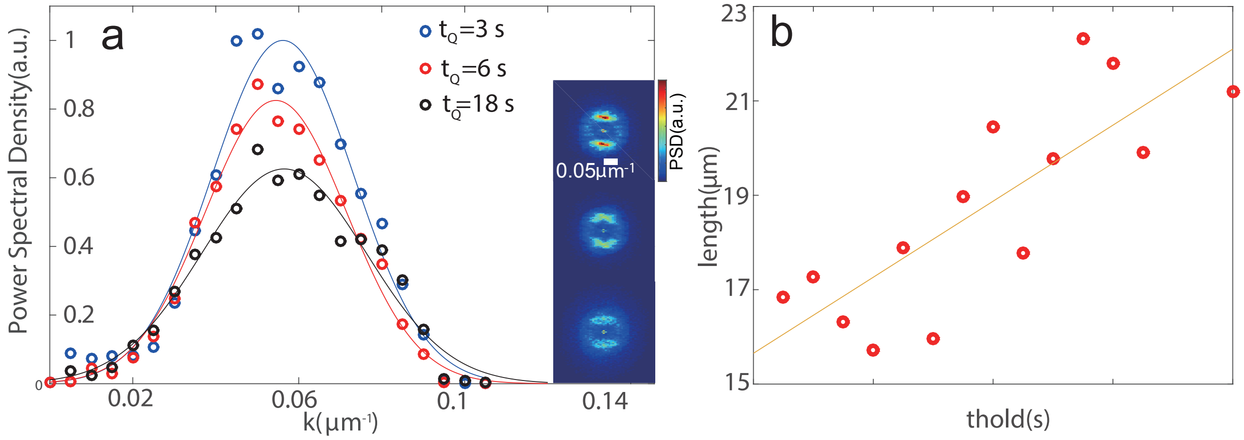

Figure 2.8: Coarsening. (a) Domain size changing as a function of t_Q. Blue, red and black circles represent power spectral density of magnon quasi-condensate for t_Q = 3, 6, 18 s correspondingly. (b) Domain size evolution as a function of hold time in trap.

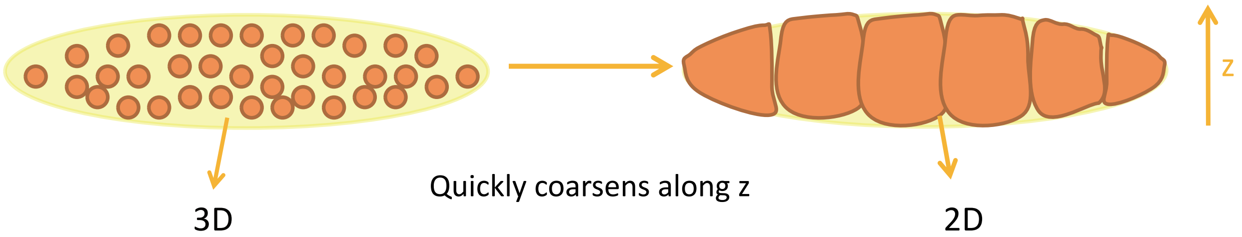

Figure 2.9: A cartoon picture shows the possible quick coarsening along z.

significant change in the domain size, shown in Fig. 2.8 a. This deviation may be attributed to a possible dimensional crossover, where the system quickly coarsens along z, the tightest trapping direction, with the Thomas-Fermi radius comparable to spin healing length, shown in Fig. 2.9. After the dimension crossover from 3D to 2D, the system can coarsen significantly slowly, confirmed by the observation that domain size changes from 17 μm to 21 μm over 10 s evolution in trap, shown in Fig. 2.8 b.

Some recent studies on the evolution of system far from equilibrium shows that it can give rise to universal behavior before the system reaches the thermal equilibrium. This universal evolution is shown to be governed by the so-called "non-thermal fixed point" [51], and is observed in a quenched 1-D Bose gas [52], as well as Rb spinor Bose gas driven far from equilibrium [53]. Both display transportation of excitations towards lower momenta. Our magnon quasi-condensate is also a system far away from thermal equilibrium. And, as mentioned above, we observe the domain size increases, thus momenta lower, during the evolution. However, due to the limited imaging resolution, we are not able to resolve the evolution of high k features of magnon quasi-condensate. On the other hand, our system can coarsen rapidly along the tightest trapping direction, with a dimension crossover from 3D to 2D. With the dependence of dimensionality of the universal theory, our experimental system can be an interesting platform to study evolution of system far away from equilibrium.

2.6 Conclusion

This chapter presents our results on magnons in spin-1 Bose gas, which is the third result of our magnon series. By probing the spatial distribution of thermal magnons, the momentum distribution near the critical point, and the critical magnon number for condensation, we confirm experimentally that magnons live in a flat potential within the majority condensate. Driving the system across the magnon condensation transition, we observe an accumulation of inhomogeneous transverse magnetization. With the spin-echo technique, we are able to image the full magnetization of magnon quasi-condensate and observe the Mermin-Ho spin textures, in which the orientation of the magnetization spans a small cap about the longitudinal axis. We then monitor the evolution of this magnon quasi-condensate in trap. Magnon condensation in a spinor gas offers a new system in which to study the Bose-Einstein condensation of quasi-particle excitations and of quantum gases in a uniform potential. Detailed measurements of the non-equilibrium dynamics of the magnon quasi-condensate present challenges for further study. Measurements of the real-time evolution of the gas magnetization, using repeated non-destructive spin-sensitive imaging [32, 54] with finer spatial resolution than achieved here, may address these challenges.

Chapter 3

Experimental upgrades for two-element laser cooling and trapping of ^{7}Li and ^{87}Rb

This chapter focuses on our efforts incorporating ^{7}Li into a ^{87}Rb BEC machine. These efforts include a change of a single species oven dedicated to ^{87}Rb into a dual species one for both ^{7}Li and ^{87}Rb. The design details have been well-documented by Ryan Olf in his thesis [2]. Therefore, here we mainly focus on the performance of this oven. To load a dual species magneto-optical trap (MOT), we then adapt a ^{87}Rb slower to a ^{7}Li one. Here we record our dual-species MOT loading sequence and the performance of this dual-species Zeeman slower. Then we come to ^{7}Li laser system, including ^{7}Li MOT, ^{7}Li slower, ^{7}Li MOT repump laser operating frequencies, as well as ^{7}Li laser locking scheme.We describe also the implementation of gray molasses near the D1 line to cool ^{7}Li atoms well below the Doppler temperature.

The next two chapters document our two experiments on this mixture machine. Specifically, Chapter 4 describes co-trapping of the two species magnetically. Chapter 5 describes co-optical trapping of the two. In the present chapter, we detail out the procedures for magnetically trapping and optically trapping, as well as some improvements that can be made to help improving the atom number stability. Finally, we propose a path towards quantum degeneracy for both species.

3.1 Dual species oven and Zeeman slower

In the late 2015 and early 2016, we did an oven change from a single species ^{87}Rb to a dual species one with ^{7}Li and ^{87}Rb. This new oven is the improved version recorded in Ryan's thesis. Here I will briefly summarize the features.

Due to the stark difference in vapor pressure of the two, ^{7}Li and ^{87}Rb are separately stored in two cups and heated separately, connected by a intermediate nozzle, welded in

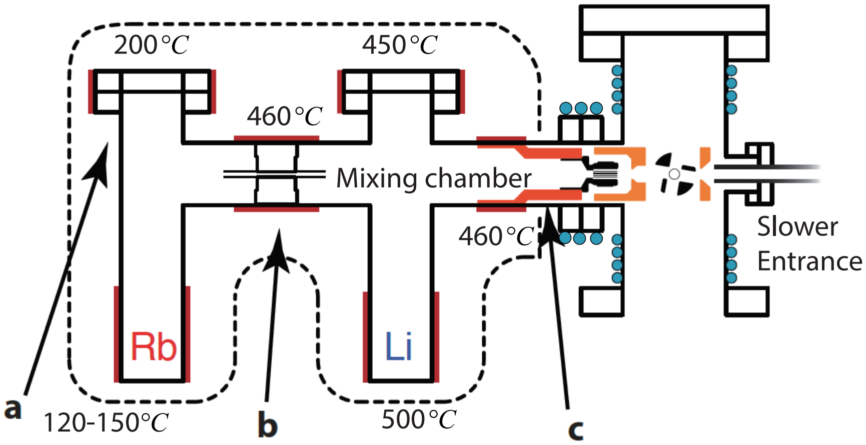

Figure 3.1: Dual species oven. ^{87}Rb and ^{7}Li reservoirs are stored separately in two cups, connected by an intermediate nozzle, before they are mixed in the mixing chamber, collimated by the main nozzle, and enter the slower. Red shaded areas are the band heaters from Mi-Plus with the nearby temperature representing corresponding area's operation temperature. Blue circles on the chamber connecting the main nozzle and the slower entrance mark the cross-sections of water cooling coils, which keep the heat from the oven from heating the rest of the chamber. (a): The large separation between reservoir and flange allows them to be heated more. This configuration is also compatible to the long ^{7}Li ampoule. (b): Intermediate nozzle welded in place to connect the ^{87}Rb reservoir and the mixing chamber. c: The main nozzle assembly involves large gap between the nozzle heater and the high vacuum chamber, reducing the thermal gradient across the nozzle flange. In addition, we add water cooling coils around the nozzle flange to lessen the thermal burden from the nozzle heater, shown by the blue circles around the nozzle flange.

place. The atomic vapor is mixed within the hot mixing chamber, and is then collimated by another capillary-array nozzle, called main nozzle. This nozzle design is well-documented in G. Edward Marti's thesis. For temperature control, we use Mi-Plus band heaters with built-in thermocouples from TEMPCO and a PID controller from Omega Engineering, and heat the oven at multiple places, shown in Fig. 3.1. We use a nickel gasket for the ^{7}Li oven flange and a silver-plated copper gasket for main nozzle flange. During our almost three years of operation, we did not encounter vacuum problems. The operating temperature for ^{7}Li is 500 degree C, with a standby temperature of 350 degree C. For the work in Chapter 4, we operate ^{87}Rb at 150 degree C. For the work in Chapter 5, we operate ^{87}Rb at 120 degree C. Fig. 3.1 shows a scheme for this dual species oven under operation.

Here I briefly mention the ^{7}Li source we use. In previous work, we loaded ^{7}Li into the oven by working with a chunk of ^{7}Li in glove bag filled with argon (^{7}Li reacts quickly in air). In contrast, in loading lithium into the oven in 2015, we adopted a different procedure. We

Figure 3.2: ^{7}Li ampoule.

used a 5 gram sample of Li that was loaded into a glass ampoule and backfilled with argon at Ames Laboratory. Compared to ^{87}Rb ampoule, this one is a lot longer. Actually, we ask them to shorten the tube due to some space concerns in our oven. It turns out that the best they can do is to shorten it to around 5". The heat of softening the glass and getting it to seal could cause melting of the Li and thus result in a possible reaction with the tube and risk of a pyrophoric reaction with air if the tube is breached.

The Zeeman slower we used was initially designed to operate as a simultaneous Zeeman slower for both ^{7}Li and ^{87}Rb [55]. The design is based on the idea that ^{7}Li and ^{87}Rb will respond differently to a rapid gradient of the magnetic field near the end of the slower: ^{7}Li atoms will continue to be slowed and to remain in resonance with slowing light through the rapidly increasing field, while the heavier ^{87}Rb atoms will fall out of resonance and proceed directly into the MOT. By this principle, both ^{87}Rb and ^{7}Li atoms can be slowed aggressively, with high deceleration, toward the end of the slower.

This slower has three stages. Here we label the stages by the coil name, stretch coil (stage I), main coil (stage II) and boost coil (stage III). Our slower is an increasing field version. The purpose of the stretch coil is to shorten the dead length between the slower entrance and the nozzle exit. The main coil is dedicated to slow ^{87}Rb . To minimize the transverse heating of ^{7}Li , ^{7}Li is abruptly slowed down in stage III by the boost coil. On the other hand, ^{87}Rb is non-adiabatic, thus should ignore the field change. However, as pointed out by Ref.[55], the existence of field curvature generated by the boost coil induces "laser heating" for ^{87}Rb because now the laser is blue detuned. Therefore, this slower cannot be operated to load the two simultaneously. Instead, in our experiment, we load ^{7}Li and ^{87}Rb sequentially.

Our test of this slower shows stage II and III are crucial while stage I is doing little for ^{7}Li and ^{87}Rb loading. Thus, we set stage I to be idle during the experiment. However, even after trying to optimize the performance of the slower by varying very many settings, we still found the slower to perform poorly for lithium, producing only a very small flux of slow lithium atoms. Our best loading rate is 10^6 s^{-1}, which is a lot smaller than the best value reported in Ref. [55], around 10^7 s^{-1}.

We suspect that this poor performance is caused by a defect in the slower coils – probably a short circuit that bypasses some of the electromagnet coils – that may have been produced when the entire apparatus was transported from a different laboratory to the present one in the year around 2009. This poorly functioning slower lengthens our experimental cycle time and also adds burden to our water-cooling system, which is later upgraded to a new cooling system with 300 psi inlet pressure including a heat exchanger and a booster pump. Meanwhile, this slower works fine for ^{87}Rb, with a loading rate of around 7×10^7 s^{-1} for a 150 degree C ^{87}Rb reservoir, although it still does not reach its best loading rate reported in Ref. [55][1], which is around 3×10^8 s^{-1}.

3.2 Laser cooling optics for ^{7}Li

As mentioned in G. Edward Marti's thesis, the initial purpose of this apparatus is to work with both ^{7}Li and ^{87}Rb in a micro-fabricated ring trap. Therefore a laser table dedicated to ^{7}Li laser cooling had already been built around 2009. However, the ^{7}Li laser setup was unused for many years. When we started using it again in 2016, we found that many components had not aged well, and that a fair bit of work was required to make the laser system operate properly. The efforts required to make the laser system work again included the following:

1) Rebuild the ^{7}Li spectroscopy cell.
2) Replace the laser diode and the optomechanics inside the 9 year old TA 100 for our ^{7}Li master laser.
3) Introduce a new tapered amplifier for 671 nm dedicated to ^{7}Li repump laser.
4) Build a new laser system dedicated to ^{7}Li gray molasses cooling.
5) Re-design the laser system optical layout.

Rebuilding the ^{7}Li spectroscopy cell: A heat-pipe for performing spectroscopy on a ^{7}Li vapor was built and tested when the ^{7}Li laser system was originally built in around 2009. A ^{7}Li heat pipe operates by producing a high temperature and high vapor pressure of ^{7}Li in the center of a long cell, in the presence of a argon buffered gas, which acts to confine the vapor pressure in the center of the long cell. ^{7}Li atoms diffusing through the inert gas

---

[1] This discrepancy may be attributed to different ^{87}Rb vapor pressure in the oven.

will preferentially re-deposit onto the metal walls of the heat pipe, which are kept at room temperature such that they will absorb and rarely re-emit ^{7}Li vapor. These walls are coated also with a metal (steel) mesh, which allows the liquid ^{7}Li metal to wick back to the center of the heat pipe and regenerate the vapor. At a high-enough inert-gas pressure, the ^{7}Li atoms will not diffuse all the way to the ends of the heat pipe, where two optical windows are placed to allow light to pass through the lithium vapor and out toward a detector.

However, at the time we turned it on in 2016, there was no ^{7}Li inside. We suspect that this absence of ^{7}Li is caused by running the heat-pipe continuously over the past seven years. Therefore, we decided to refill some ^{7}Li into the pipe, and then had some vacuum issue, preventing us from pumping the system down to mTorr level. Finally, we decided to change the design, buy new parts and load ^{7}Li back in. This new design mainly includes adding a four-way cross to the previous long heat pipe to incorporate a thermocouple gauge for pressure monitoring, as well as extending the pipe length more to prevent ^{7}Li from migrating towards the optical window. The ^{7}Li chunk is loaded into the center of the cell. We thus only heat the center to keep the rest of cell cold. For the vacuum gaskets, we use silver-plated copper gaskets. In principle, one can use nickel gaskets to preventing ^{7}Li from reacting to copper and causing leak. Fig. 3.3 shows the scheme of our new ^{7}Li cell. All ^{7}Li laser cooling light is referenced to a single master laser, which will be introduced below. With the help of this ^{7}Li cell, we lock our master laser to ^{7}Li ground state hyperfine crossover line through frequency modulation spectroscopy [56]. After some optimization according to this crossover signal and the related error signal (make it larger and symmetric), we settle on operating this cell at 310 degree C with an argon background pressure of 30 mTorr.

Replacing the laser diode and the optomechanics inside the 9 year old TA 100 for our ^{7}Li master laser: For ^{7}Li master laser, we use TA100 from Toptica, which is their initial design for 671 nm wavelength. This TA100 contains an external cavity diode laser (ECDL) and a 500 mW tapered amplifier, designed in a way that its ECDL seeds its TA. In our application, however, we manually split it into two, with its ECDL serving as ^{7}Li master laser, and its TA dedicated to our ^{7}Li MOT cooling laser. This ECDL, after several months of operation, stopped lasing in single mode in the frequency range covering ^{7}Li D_2 line. We finally replaced it with an AR-coated diode from Toptica (LD-0670-0035-AR-2). We also replaced the entire optomechanics setup including the grating mount (GH I/DL 100) and diode collimator mount (DKH I/DL 100). After these replacements, we have 20 mW output after the isolator with a mode hop free range bigger than 1 GHZ in the frequency range covering ^{7}Li D_2 line.

Introduce a new tapered amplifier for 671 nm dedicated to ^{7}Li repump laser: The tapered amplifier chip is from Eagleyard 670 nm 500 mW chip (EYP-TAP-0670-00500) on a C-mount. We use our group's TA design, recorded in James Michael Higbie's thesis, built by Thomas Mittiga.

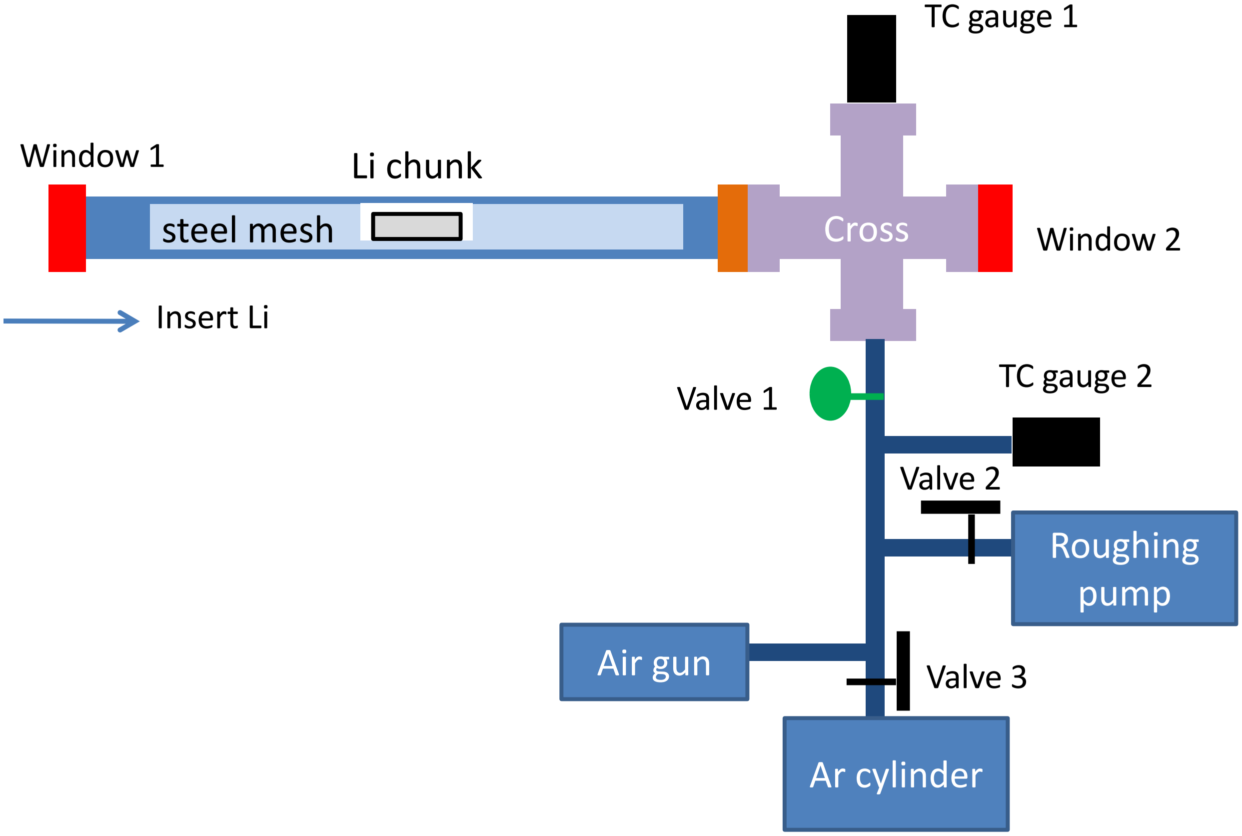

Figure 3.3: ^{7}Li spectroscopy cell. We load ^{7}Li from the left viewport, using a steel mesh with a hole cut in the middle where we place the ^{7}Li chunk. Thermocouple gauges (TC gauge) are used for pressure monitoring. An argon cylinder is used to flow argon into the system with a needle valve for flow control. The air gun is used for argon gas check to make sure that we are not using an empty argon cylinder. We use a roughing pump to pump down the system, and later add a foreline turbo pump when we flow argon to change the buffer gas pressure for optimization purpose. This foreline turbo pump is used to prevent the oily roughing pump from contaminating the cell vacuum.

Build a new laser system dedicated to ^{7}Li gray molasses cooling: In the years since the optical setup was first developed, several research groups reported on the achievement of very low temperatures for a laser cooled ^{7}Li gas using gray molasses with light that is blue detuned from the D_1 line [57, 58]. Without this approach, ^{7}Li laser cooling had been limited to Li -gas temperatures above the Doppler temperature limit owing to the failure of standard polarization gradient cooling caused by the unresolved excited-state hyperfine structure in ^{7}Li . To adopt this technique, we purchased and built a new laser system dedicated to ^{7}Li gray molasses cooling.

The laser is purchased from Toptica (DLC DL PRO) and offset-locked to ^{7}Li master.

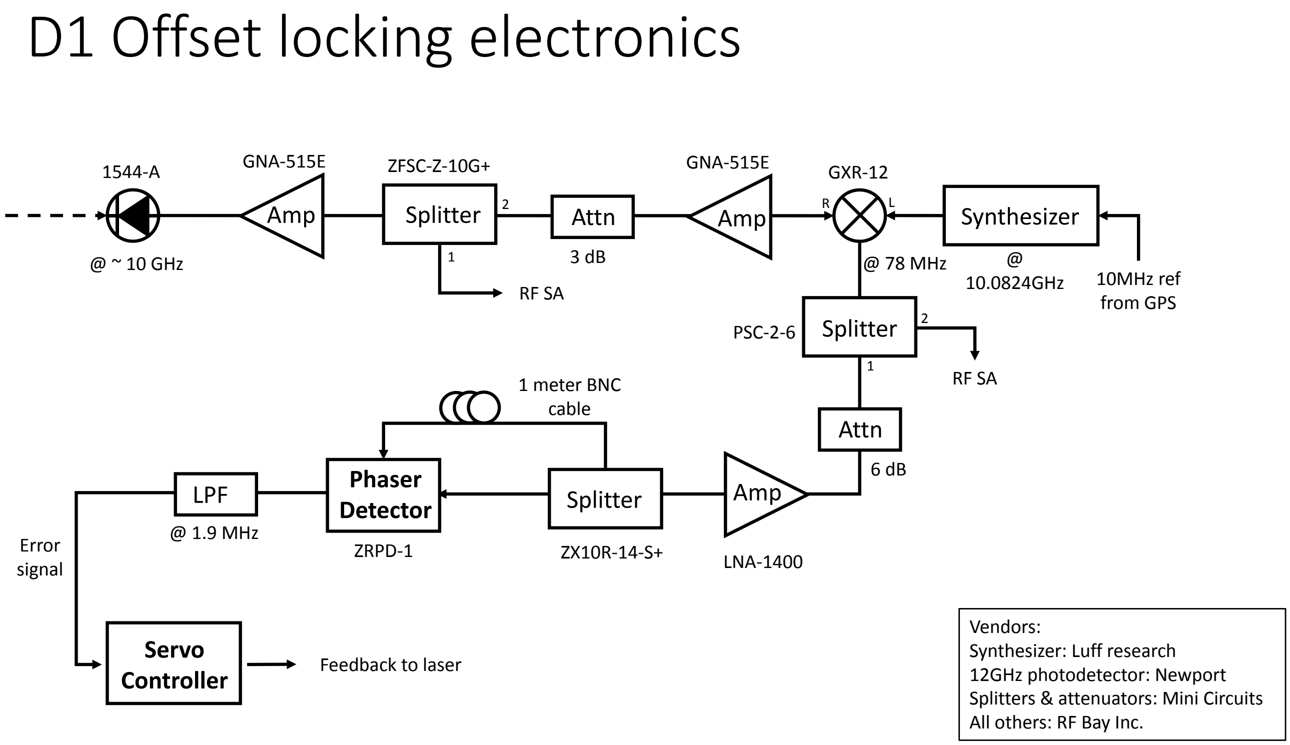

Figure 3.4: ^{7}Li D$_1$ offset lock scheme.

We use a simple delay-line locking scheme introduced in Ref.[59]. We interfere light from the D$_1$ laser with light from the D$_2$ maser laser, recording the beat note using a 12 GHZ photodetector from Newport (Model 1544). This beat note signal is then amplified and mixed with a programmable synthesizer from Luff research (SLSM5-950010500) at 10.0824 GHZ. Then the IF port of this mixer is amplified and sent into a power splitter. Both arms propagate through coaxial cable with one arm 1 meter longer than the other. Since the time delay introduced by the cable is independent of the frequency, the phase shift is proportional to the beat frequency, therefore providing an error signal for the servo. The two arms are then recombined on a phase detector, which detects the phase difference. Before sending into the servo as an error signal, a low pass filter is used to to block the high-frequency output from the mixer. Because the DL PRO laser from Toptica is inherently very stable, we require only feedback on the slow piezo branch to stabilize it at the desired frequency. Finally, we are able to offset lock the laser 10.004 GHZ from ^{7}Li master towards ^{7}Li D$_1$ line. Fig. 4 details out our offset locking scheme.

Gray molasses cooling lasts for a couple of ms. Therefore, we decided to use an acousto-optical modulator (AOM) to control the intensity of the D$_1$ laser cooling pulse; the AOM provides intensity control at sub-μs resolution, suited to our needs. We inject lock another home-built solid state laser (HL6555G) to this offset-locked D_1 laser and then send it through an AOM before seeding a TA (SYS BOOSTA 670 L) purchased from Toptica. The output of the TA first passes through an electro-optical modulator (EOM) from Qubig (EO-Li7-M3-Vis) to put on a 4% sideband at 802.7 MHZ[2] and is then coupled into a polarization-maintaining fiber and delivered to the experimental table with around 130 mW for our molasses cooling.

Gray molasses functions by trapping atoms within dark states with a narrow velocity distribution. These dark states remain dark, in the presence of laser light that is incident from all directions, only in the case that the magnetic field applied to the atoms is near zero. In our experiment, we compensate the gradient caused by the eddy current from the sudden turn-off of MOT magnetic field gradient. For the work in Chapter 4, we do a 2 ms gray molasses cooling. For the work in Chapter 5, we grab ^{7}Li directly from gray molasses stage. To optimize this efficiency, we end up doing a 20 ms gray molasses cooling with trap laser light on. During this process, we adjust our compensation field settings to follow the eddy current. Fig. 3.5 shows our optical set up for this gray molasses cooling.

Re-design the laser system optical layout: Fig. 3.6 shows our optical table layout. This layout includes three home-built 671 nm solid state lasers (HL6555G), injection-locked by the maser ECDL whose frequency is shifted according to our requirements for Li MOT, Li repump and Li slower. Then the three lasers serve as the seed to three TAs before coupled into a single mode polarization maintaining (PM) fiber and delivered to our experimental table. For the slower light, we additionally send it through an EOM to put on sidebands on repump frequency (813.75 MHZ[3]) before delivering it to the experimental table. The total powers for the three are around 100 mW measured at the experimental table. Fig. 3.7 shows ^{7}Li energy levels and relevant laser frequencies in our experiment. Fig. 3.8 shows a schematic diagram of the laser system, including the locking scheme.

One feature of this design is that we shift the frequency of the injection laser instead of the seed itself. We choose this configuration to have enough seed power for TAs. However, in this configuration, the TAs are always seeded, which constrain the time scale for laser controlling. We end up using mechanical shutter, with a control time scale of ms.

---

[2] update to 803 MHZ for the work in Chapter 5 for better optical trapping

[3] This number is adjusted for better ^{7}Li MOT loading

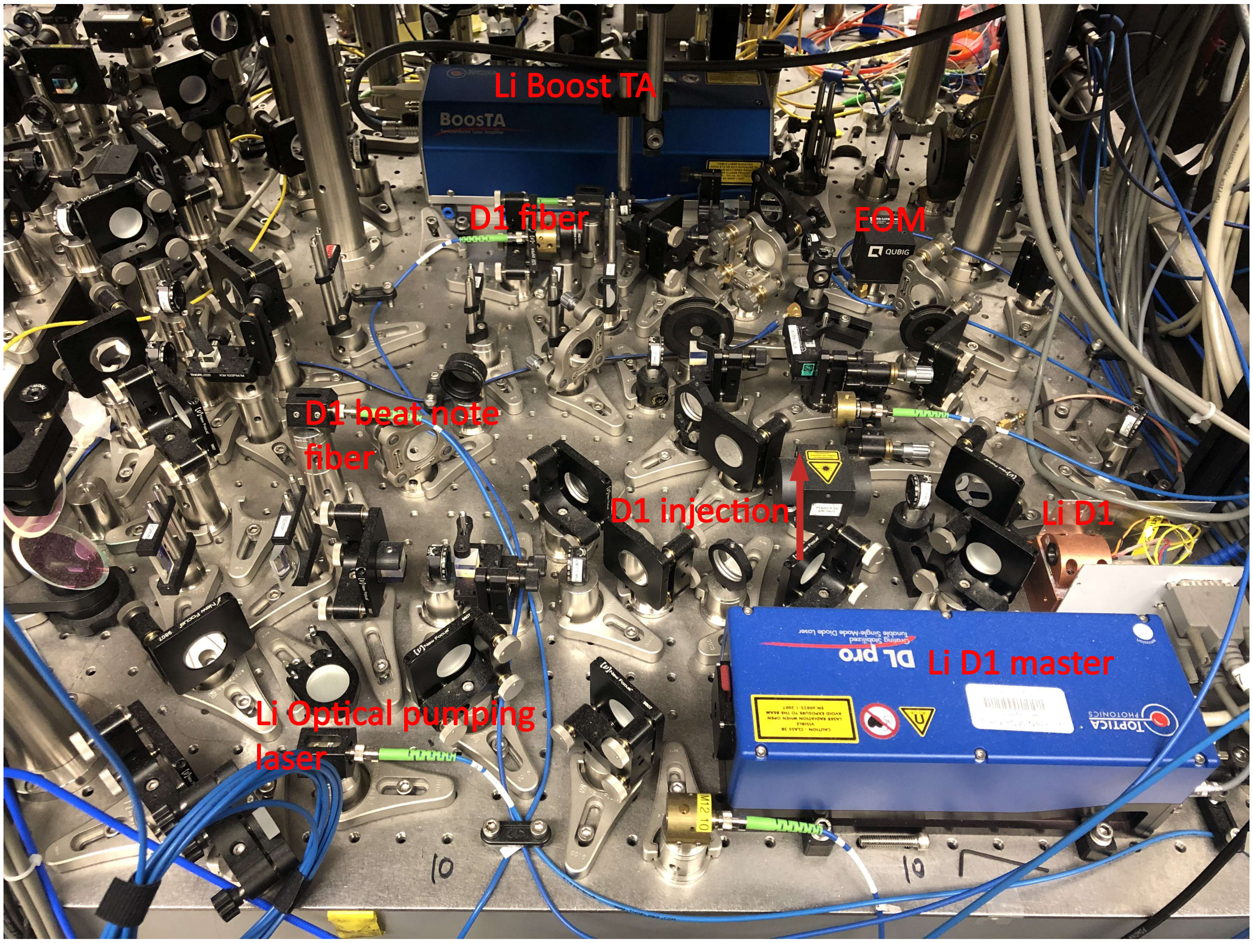

Figure 3.5: ^{7}Li D_1 optical table lay out.

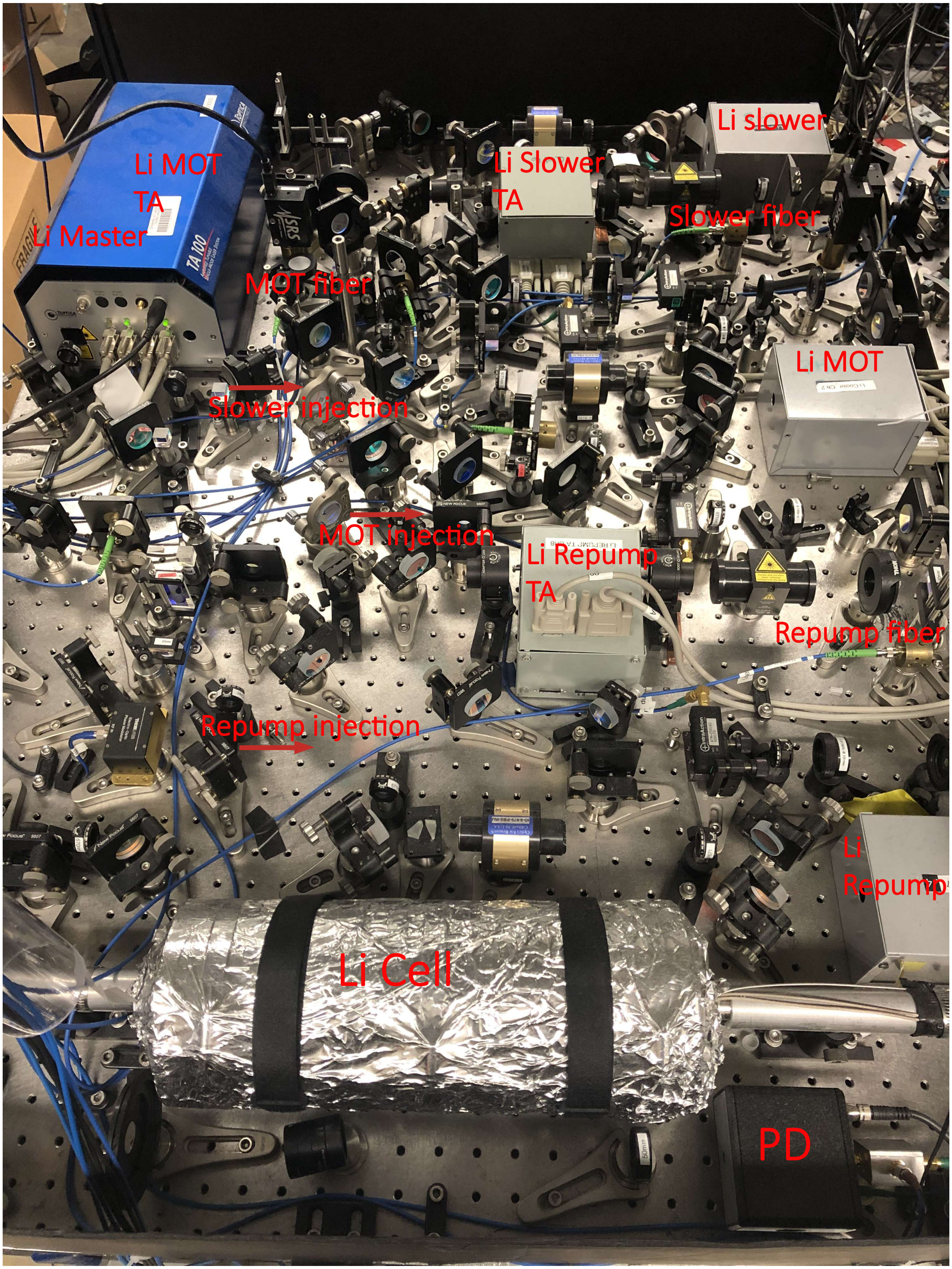

Figure 3.6: ^{7}Li optical table lay out.

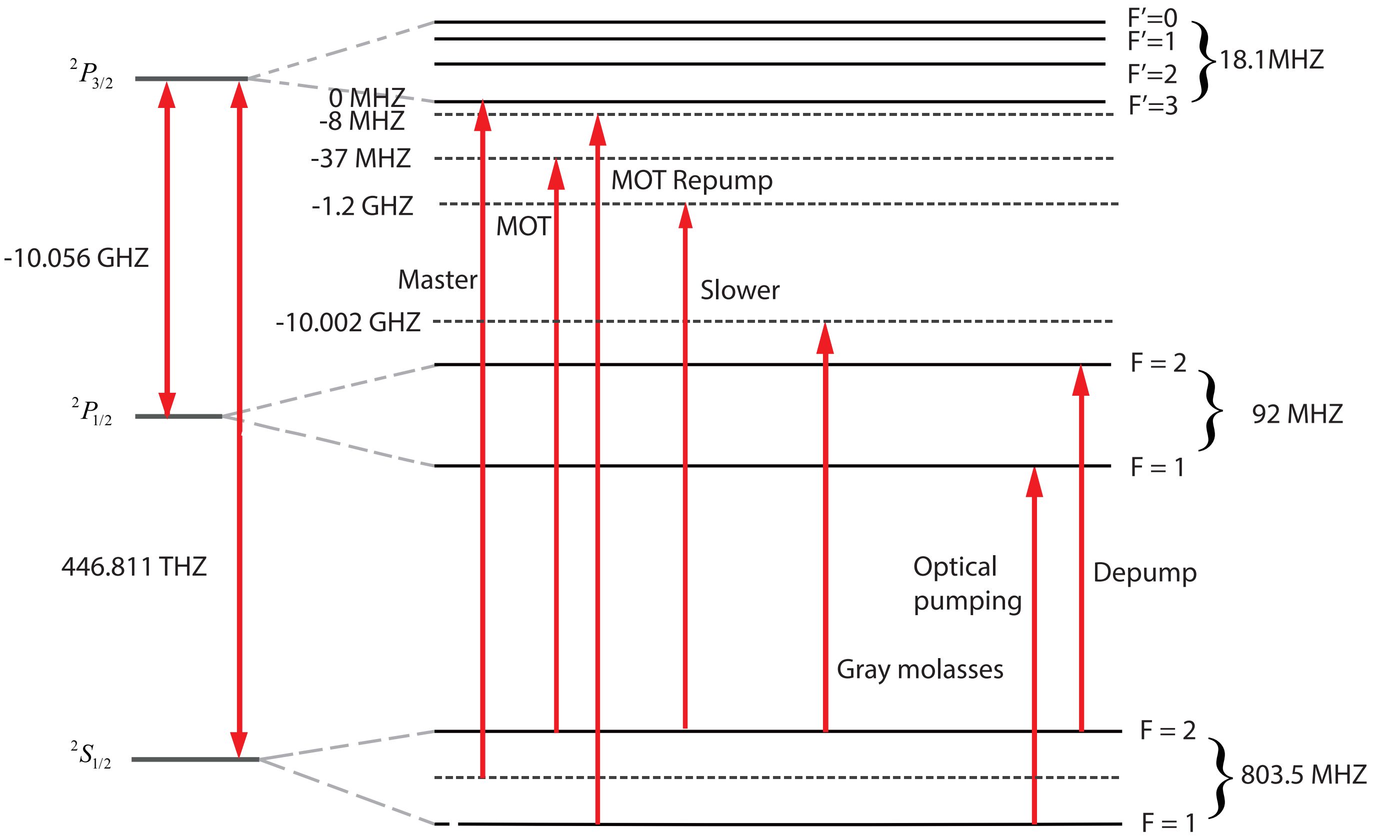

Figure 3.7: ^{7}Li laser frequencies with respect to its energy level.

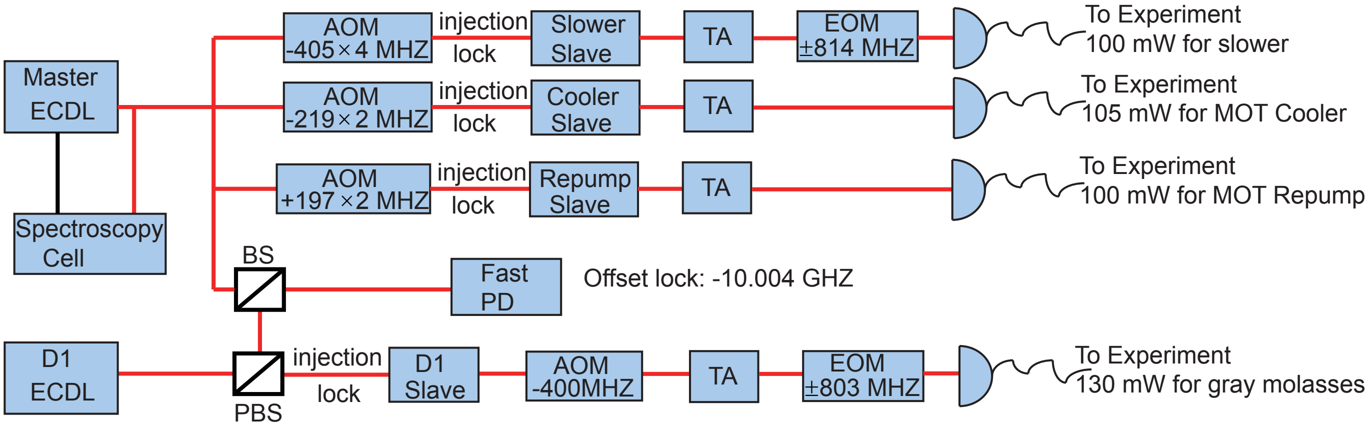

Figure 3.8: Schematic diagram of ^{7}Li laser system. The master ECDL is locked to the ^{7}Li ground state hyperfine crossover line through frequency modulation spectroscopy. Then this master laser is split and frequency shifted by AOMs to the required frequency for ^{7}Li slower, MOT cooler and MOT repump. Three home-built slave lasers are injection locked by these frequency shifted lights from the master, before they seed three TAs and are delivered onto the experimental table by PM fibers. D_1 ECDL is offset-locked to the master. Another home-built slave laser is injection locked by this D_1 ECDL, and then frequency shifted by an AOM before it seeds a TA. The output of the TA first passes through an EOM to put on a 4% sideband before delivered onto the experimental table for ^{7}Li gray molasses cooling.

3.3 Experimental Sequence

National Instrument data acquisition boards and Cicero software are used for experimental sequence control. In our experiment, we load a ^{7}Li MOT first for 90 s. Then while holding the ^{7}Li MOT, the slower configuration changes to support ^{87}Rb MOT loading for a couple of seconds.

We observed that ^{7}Li atoms are rapidly lost when they are trapped in the presence a rubidium MOT, owing to lossy light-induced collisions between excited-state Rb atoms and ground-state Li atoms [60]. To get around of this unpleasant loss, we add a pusher beam to spatially separate ^{87}Rb MOT from ^{7}Li MOT during ^{87}Rb MOT loading process. This pusher beam is formed directly by the ^{87}Rb imaging light.

We optimize this pusher beam with the following procedures. First, we increase the pusher beam power until we lose our ^{87}Rb MOT, caused by the severe MOT power imbalance. Second, we scan the pusher beam frequency near the pusher power threshold to figure out the frequency corresponding to the largest "pushing force", where we encounter ^{87}Rb number loss at the lowest beam power. Third, we park the pusher beam at this frequency and do a fine power scan while monitoring ^{87}Rb number in the MOT. From this measurement, we know the "safe zone" to operate this pusher beam where we have stable ^{87}Rb number. Finally, we add ^{7}Li into the experimental sequence and find a sweet pot within the "safe zone", where we have stable atom number in the spatial separated dual species MOT for both ^{7}Li and ^{87}Rb. After this optimization, we end up using around 1 mW imaging light with a beam diameter around 1.4 cm. Fig. 3.9 shows the experimental pusher performance after the optimization. This pusher beam is crucial for the experiment discussed in Chapter 4, where our ^{87}Rb MOT atom number is on the order of 10^9. For the experiment discussed in Chapter 5, where we load atoms in the ODT directly from the molasses stage, we have around 10^8 ^{87}Rb atom in the MOT. There, it turns out that the initial slight spatial offset of the two MOT is enough to avoid this inelastic loss of ^{7}Li. We thus disable the pusher beam during the ^{87}Rb MOT loading.

Then this pusher beam is gradually turned off in 20 ms before the 2 ms compressed MOT where the ^{87}Rb MOT trap laser frequency detuned further away from the resonance together with a decrease in ^{87}Rb repump laser intensity. This 20 ms is determined such that ^{87}Rb polarization gradient cooling stage's performance is similar to the case without applying the pusher beam. At the same time, ^{7}Li MOT trap laser frequency detuning is decreased to 18 MHZ. Then the ^{7}Li MOT trap laser and repump laser is turned off by the mechanical shutter. Meanwhile, the MOT gradient is rapidly turned off before we start the gray molasses cooling stage for ^{7}Li and polarization gradient cooling for ^{87}Rb. At the end of this molasses cooling, both gases are at a temperature of around 40 μK. Fig. 3.10 shows our experimental sequence.

Magnetic trapping: After the molasses cooling process, both species are depumped into $F = 1$ manifold. Then we apply a short two-color optical pumping beam for both species to pump them into $|F = 1, m_F = -1\rangle$ state before turning on our spherical quadrupole trap. This optical pumping help enhance the trapped atom number in the magnetic trap by about

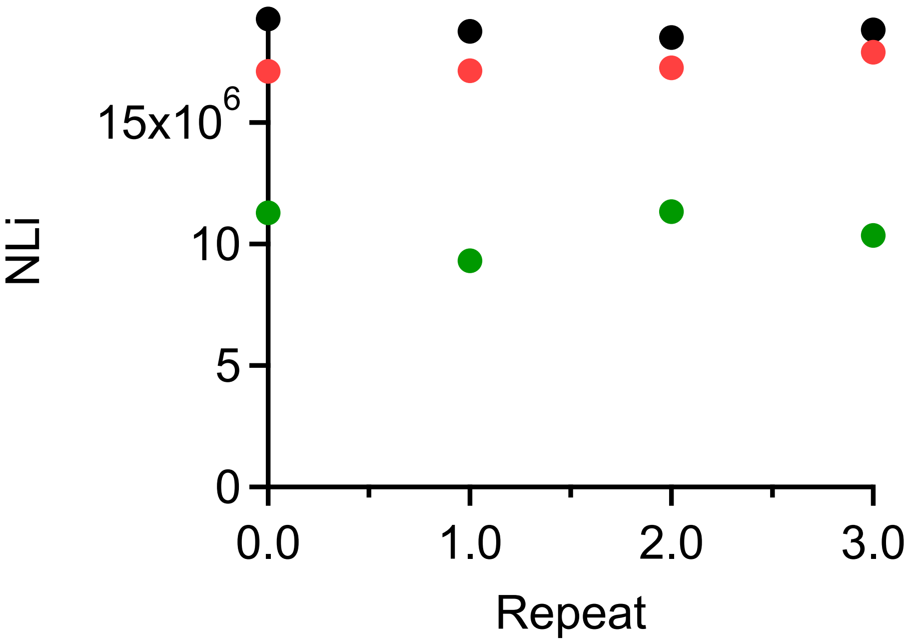

Figure 3.9: Pusher beam behavior after optimization. In this experiment, we have around 10^7 ^{7}Li coexisting with 10^9 ^{87}Rb in the MOT. Black circles, red circles and green circles represent ^{7}Li atom number in the MOT without ^{87}Rb, with ^{87}Rb and pusher, with ^{87}Rb but without the pusher, respectively.

a factor of two for both species.

Optical trapping: During the molasses loading, a 10 W 1064 nm single beam dipole trap (ALS-IR-1064-50-A-SF) with a waist of around 34 μm is turned on to directly grab both ^{87}Rb and ^{7}Li. Then we apply again a short two-color optical pumping beam for both species. This time, however, the optical pumping is done in the dipole trap, rather than in free space, produced by the ALS laser. A detailed discussion about this approach is in Chapter 5.

Here we comment on the atom number stability of this all-optical approach. We observe a daily slow drift in total atom number on the order of several hours. This slow drift can be related to the polarization fluctuations of our MOT beams. Due to historical reason, we are using some cheap optics from Foctek puchased back in 2006-2008, including polarization beam splitter (PBS), as well as dual-color waveplates for ^{7}Li and ^{87}Rb, for our MOT optics. For this all optical approach, we align our trap laser to the densest part of the atomic molasses. Therefore, the total atom in the dipole trap depends on the relative position of dipole trap and atom molasses. We confirm this polarization fluctuation, which leads to the MOT beam intensity balance fluctuation, by imaging the molasses position after we observe a atom number change bigger than 20%. Indeed, the molasses position shifts. We later

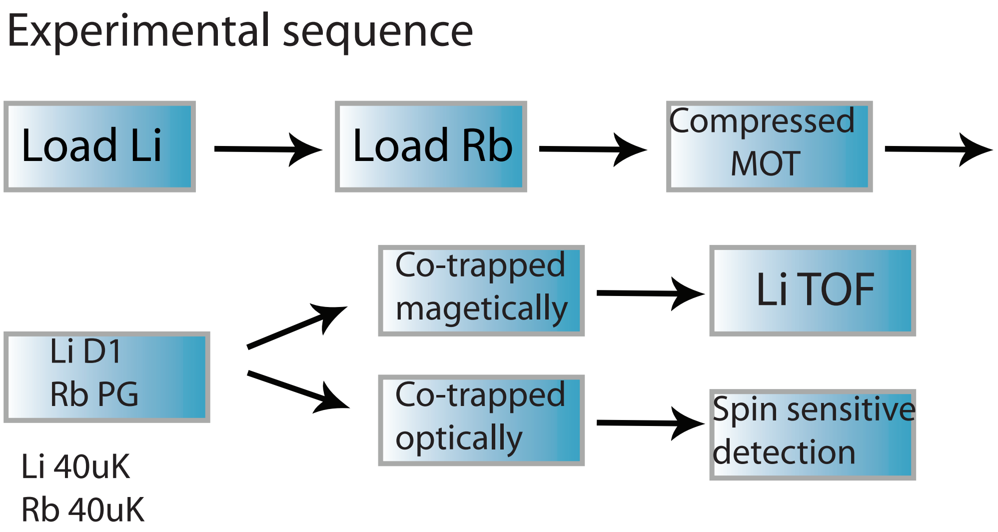

Figure 3.10: Experimental sequence for Li-Rb, including both magnetic and optical approach.

monitor the long term drift by constantly monitoring the molasses position and confirm the time scale. The atom number drifts also become more severe when there is a large temperature fluctuation in the lab. We improve the situation by adding clean-up cubes after the PM fiber as well as replacing Thorlabs PM fiber by PM fiber from OZ optics. However, to achieve better atom number stability, we suggest replacing all the cheap optics by better ones, including the cubes and dual-color waveplates. Additionally, using good optics is more crucial for dual-species experiment because the relative position of the two MOT might matter. For instance, one might want to avoid loss by spatially separated the two as we do for ^{7}Li and ^{87}Rb, and might want to manipulate them at the same time, thus requires perfect and stable overlap of the two.

3.4 Path towards quantum degeneracy

In this section, we review our two attempts in bringing both species down to quantum degeneracy. The starting condition is around 10^9 ^{87}Rb and 4×10^7 ^{7}Li at molasses stage at a temperature of about 40 μK.

Attempt I: We first attempted to produce a quantum-degenerate gas mixture through sympathetic evaporation in a spherical quadrupole magnetic trap. Since we had a large ^{87}Rb population and small ^{7}Li population, the idea was to evaporate away the ^{87}Rb atoms selectively, and then have ^{7}Li atoms cool by collisions with the cold ^{87}Rb gas.

We confirmed that we were able to produce ultracold ^{87}Rb gases within the magnetic trap. For this purpose, to avoid the Majorana losses, we added a green laser, focused it to the center of the spherical quadrupole trap, with total power of 10 W and a waist of 19 μm. With this green plug, we were able to evaporate ^{87}Rb down to less than 1 μK. For comparison, without this plug, we were only able to cool it down below 100 μK without the unwanted atom loss.

However, our experiment showed that ^{7}Li was disengaged from ^{87}Rb evaporation, suggesting a weak interspecies cross section. Taking advantage of the small cross section of ^{7}Li (around 5 a_B) and the non-ergodicity of the spherical quadrupole trap, we did a cross dimensional relaxation measurement to quantify the cross section between the two at a collisional energy of a couple of hundred μK. A careful comparison between experiment and theory showed that we measured a cross section significantly larger, although it was still not large enough for sympathetic cooling to work within the 60 s life time of the two. This investigation is recorded in Chapter 4.

The interspecies cross section for the two species at $|F = 2, m_F = 2\rangle$ might be enough for sympathetically cooling. Previous research [61] shows a severe inelastic process between $|F = 2, m_F = 1\rangle$ ^{87}Rb and $|F = 2, m_F = 2\rangle$, thus a clean up of this unwanted state is required. However, unlike Ioffe-Pritchard-type trap, it is not really possible to get rid of $|F = 2, m_F = 1\rangle$ ^{87}Rb in a spherical quadrupole trap. Finally, after using our experimental setup to measure the Li-Rb interaction strength (see Chapter 4), we abandoned this approach and tried an all-optical approach instead.

Attempt II: Here we describe our attempt to achieve quantum degeneracy in a Li-Rb gas mixture through an all-optical approach, where we directly grab both species from molasses stage in a optical dipole trap (ODT) formed by a 1064 nm laser beam.

Following our work on magnetically trapped gases, our hope for this all-optical approach was that the high density of the optically trapped gas would yield a sufficiently high interspecies thermalization rate, in spite of the small ($\approx$ -20 a$_B$) interspecies scattering length for Li-Rb collisions in the $|F = 1, m_F = -1\rangle$ state, to allow for sympathetic cooling. We initially used a multimode laser from IPG (YLR-100-1064-LP). However, we found that this multi-frequency trapping light led to stimulated Raman scattering, which produced Rb atoms in the $F = 2$ state after they had been purified in the $F = 1$ state. It was known (and we confirmed) that Li atoms undergo rapid hyperfine relaxation collisions with Rb atoms in the $F = 2$ state, and, given that we were working with a small minority of Li atoms, even a small admixture of $F = 2$ atoms in the Rb gas causes extreme losses in the Li gas population. We therefore upgraded it to a single frequency 1064 nm laser (ALS-IR-1064-50-A-SF). For comparison, with similar overlap density of ^{7}Li and ^{87}Rb (per ^{7}Li) and the same trapping power as well as dipole trap geometry, we had less than 1 s life time in the trap formed by the multimode laser and around 11 s life time in the trap formed the single frequency laser. The measured ^{7}Li lifetime in the single frequency dipole trap alone was around 16 s.

Before we studied the sympathetic cooling of ^{7}Li in the ^{87}Rb bath in the ODT, we first confirmed our capability to cool ^{87}Rb down to quantum degeneracy by adding a second beam along another optical axis 120° to the original one formed by a single frequency 1064 nm laser light from Nufurn, to create a cross dipole trap (CODT). This CODT led to a 10 fold enhancement in ^{87}Rb density and with the help of this CODT, we were able to create a small ^{87}Rb BEC with total atom number on the order of 10^4.

The next challenge we faced was that of evaporating ^{87}Rb atoms preferentially from the optical trap. The detuning of 1064 nm trapping light from the principal atomic transition is smaller for ^{87}Rb (lines at 795, 780 nm) than it is for ^{7}Li (lines at 671 nm). Thus, the optical trap produced by 1064 nm wavelength light is deeper for ^{87}Rb than it is for ^{7}Li Ė vaporatively cooling by lowering the depth of this trap would cause Li atoms, rather than Rb atoms, to be preferentially evaporated, contrary to the scheme we were hoping to implement. Therefore, our attempt included adding a second color of trap beam at 767 nm, along the path of the second ODT, with similar waist at the atoms as 1064 nm Nufurn laser light, making one arm of the CODT bichromatic. The 767 nm trap beam generated a potential barrier for ^{87}Rb while making ^{7}Li trap deeper. Through adjusting the power of the three ODTs, in principle, we should be able to evaporate ^{7}Li-^{87}Rb system in a bichromatic dipole trap where ^{7}Li saw a deeper trap depth compared to ^{87}Rb. Fig. 3.11 shows our design scheme for this bichromatic CODT trap.

Unfortunately, in our experimental attempt to implement this two-color optical trap, we found, again, that Raman scattering produced Rb atoms in the $F = 2$ level. This time, the Raman process was mainly from the spontaneous Raman process caused by the 767 nm [62], due to its closeness to the ^{87}Rb principal atomic transition. For example, for a design parameter of 0.45 W 767 nm dipole trap with a beam waist of 30 μm, the spontaneous Raman scattering rate is about 0.5, corresponding to about 10% ^{87}Rb atoms scattered into $F = 2$ within one second. In our experiment, we had around 10 times larger ^{87}Rb population compared to ^{7}Li. Therefore, this slow 10% generation of ^{87}Rb in $F = 2$ could be detrimental to the co-trapped ^{7}Li. In the end, we stopped this investigation and instead, switched direction to study the spin-dependent interaction between the two, recorded in Chapter 5.

Here we conclude with some suggestions on methods to bring the two towards quantum degeneracy :

Method I: Following the step of Ref. [61], one can build a Ioffe-Pritchard-type trap/Cloverleaf trap and do sympathetic cooling with both species in $|F = 2, m_F = 2\rangle$. This sympathetic cooling should be able to bring the temperature of the two down to μK level. Then, from there, they can be easily grabbed into an optical dipole trap for evaporation cooling. Some complexity can emerge when the dipole trap is shallow enough so that the gravitational sag will cause the two cloud to spatially separate from each other. If this is a problem, a bichromatic dipole trap can be turned on to compensate this effect. Due to the fact that the cloud is cold enough, the power of the trap laser should be tiny so that the spontaneous or stimulated Raman process should not be a concern. Another knob to compensate the gravity sag could be magnetic field gradient. The difference in hyperfine splitting of the two leads to different response to field gradient.

Method II: Perform cooling process separately for the two as recorded in Ref. [26]. For ^{7}Li, one can follow an all optical approach taking advantage of the broad Feshbach resonance, and then shift it away in an optical dipole trap before ^{87}Rb loading process. Finally, one needs to move ^{7}Li back to overlap with ^{87}Rb.

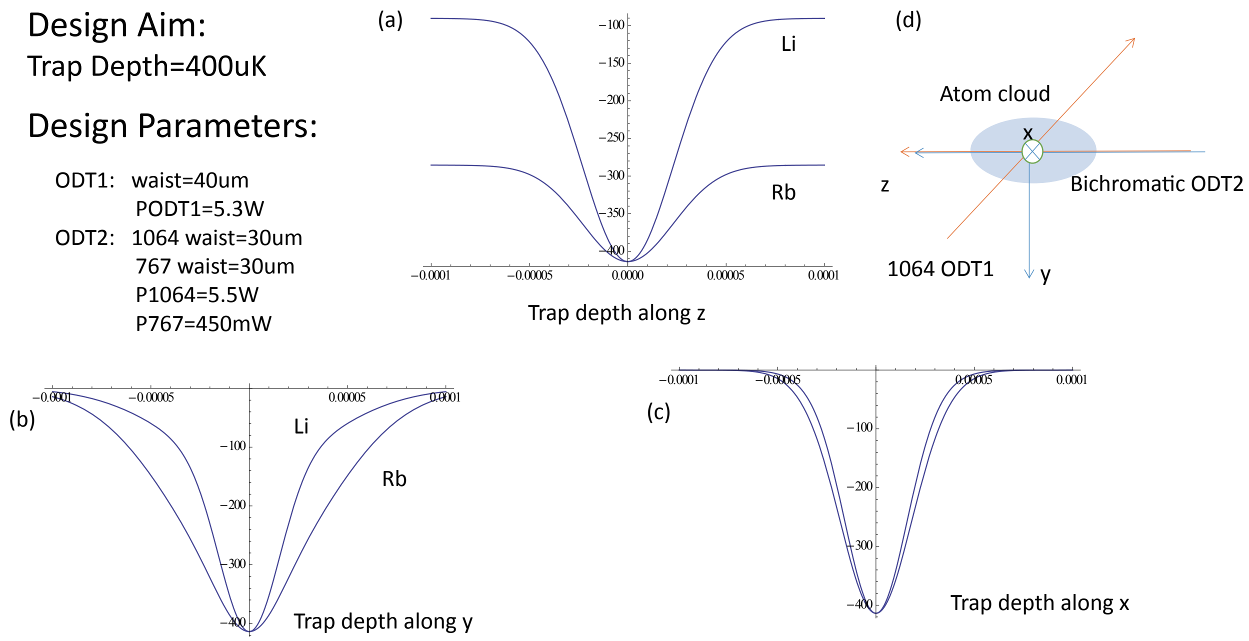

Figure 3.11: Bichromatic CODT scheme. (a), (b) and (c) are the trapping potentials for ^{7}Li and ^{87}Rb along z, y and x axis, correspondingly. Y axis of the plots is trap depth in the unit of μK. X axis of the plots represents the spatial extension along z, y and x axis in the unit of meter. The trap geometry is shown in (d), with 1064 ODT1 representing the first ALS single frequency 1064 nm ODT, bichromatic ODT2 representing the co-propagating two-color second ODT formed by the 1064 nm Nufurn laser and 767 nm laser light, and xyz the coordinate axis for the lab frame.

Chapter 4

Cross dimensional relaxation of ^{7}Li through collisions with a ^{87}Rb gas

Presented in this chapter is our study of ^{7}Li-^{87}Rb mixture system co-trapped in a spherical quadrupole trap, with both species in $|F = 1, m_F = -1\rangle$. As described in the previous chapter, our goal was to realize sympathetic cooling of ^{7}Li through evaporation of a majority ^{87}Rb gas, using element-selective microwave evaporation from a plugged spherical quadrupole magnetic trap.

However, the main finding of our work was that ^{7}Li was disengaged from ^{87}Rb. In a set of experiments where we prepared ^{87}Rb reservoir at different temperature ranging from 170 μK to 400 μK and then monitored the evolution of ^{7}Li in this ^{87}Rb bath, our observation showed that ^{7}Li stayed at almost the same energy distribution during this seconds long hold with ^{87}Rb, indicating a small cross section between the two. Nevertheless, even though our hopes of achieving sympathetic cooling and quantum-degenerate gas mixtures through this approach were not realized, we were able to use the observed slow dynamics of the co-trapped ^{7}Li-^{87}Rb gas mixtures for a useful measurement, including:

- Non-ergodicity of ^{7}Li in spherical quadrupole magnetic trap
- A time scale separation in cross dimensional relaxation and thermalization
- Non-exponential relaxation of ^{7}Li [1]

These features give us the convenience to quantify the cross section between the two at a collisional energy of hundreds of μK and a simplification in comparing the experimental data to theory. In the following sections, we will dive into a detailed explanation of these features and our measurement results for the interspecies cross sections, as well as a careful

---

[1] Our experimental data could be too noisy to confirm this non-exponential behavior, although our theoretical simulation strongly suggests its existence.

comparison with theory, indicating our results, although small enough to discourage sympathetic cooling, are significantly larger than the theoretical prediction at our collisional energy. The result of this measurement is presented in a recently published work [63]. In this chapter, I describe some further details of the experimental work that are not described in our publication.

4.1 Non-ergodic behavior of ^{7}Li in spherical quadrupole trap

A mismatch between the oblate equal-potential lines of spherical-quadrupole trap and the prolate spatial distribution of ^{7}Li after gray molasses cooling leads to an initial anisotropy in ^{7}Li momentum distribution. Our observation shows that this initial anisotropy lasts for 40 s, around the vacuum life time. See Fig. 4.1 a. With the fact that the interactions for ^{7}Li in $|F = 1, m_F = -1\rangle$ are extremely small such that the ^{7}Li gas on its own can be taken as a non-interacting gas at our experimental density, this observation still surprised us at the very beginning. Unlike the harmonic trap where the three principal axes are decoupled from each other, the spherical quadrupole trap seems to couple the motion in its three axes, with an atom at low energy moving in a potential of the form:

$$U(x, y, z)_{\text{lin}} = \mu B' \sqrt{z^2 + (x^2 + y^2)/4} \tag{4.1}$$

where x, y and z are Cartesian coordinates, B' is the magnetic field gradient along the trap axis, and $\mu = \mu_B/2$ is the atomic magnetic moment at low field in the $|F = 1, m_F = -1\rangle$ hyperfine state, with μ_B being the Bohr magneton. We neglect the small nuclear magnetic moments. To understand this non-ergodic behavior, we set up a very simple simulation using Newtonian equations of motion for particles moving in the spherical quadrupole trap with an initial momentum anisotropy. Our numerical simulations confirm that the particle's motion is quasi-periodic and non-ergodic. We later found out that another group also observed similar behavior in spherical quadrupole trap for fermionic ^{6}Li [21, 22] and a theoretical paper confirmed the quasi-periodic motion in the trap [64].

This non-ergodicity of the spherical quadrupole trap is related to the cylindrical symmetry along z axis. Our simulation shows that the motion of the particle becomes ergodic after adding an energy barrier along one in-plane axis, which breaks this cylindrical symmetry. This model prediction was verified nicely in our own experiments. Specifically, we studied the evolution of the ^{7}Li gas trapped in the spherical quadrupole trap, while also breaking the cylindrical symmetry by adding a repulsive optical potential from a 10 W 532 nm laser light (Sprout-G 15 W) focusing down to a waist of around 19 μm towards the center of the trap along one in-plane axis. The ^{7}Li cloud was held in this hybrid trap for 4 s, much longer than the trap period, before released from the trap. With this light on, we observed the ^{7}Li cloud distribution matched its equilibrium value. See Fig. 4.1 b.

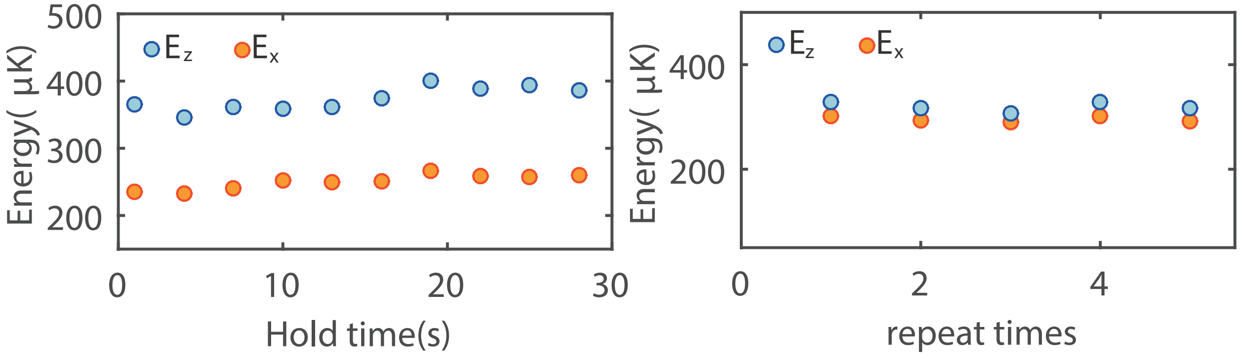

Figure 4.1: Non ergodicity. (a) ^{7}Li alone in spherical quadrupole trap at $B' = 240$ G/cm. (b) ^{7}Li alone in spherical quadrupole trap with optical plug barrier potential $B' = 240$ G/cm.

The non-ergodicity of ^{7}Li gas on its own in spherical quadrupole trap provided a straightforward method to measure the cross section between ^{7}Li and ^{87}Rb. By colliding with ^{87}Rb, the initial anisotropy in ^{7}Li momentum distribution can relax towards equilibrium where the axial and in-plane mean kinetic energy are at equal value. By monitoring this relaxation process, we should be able to extract the cross section between the two at our experimental collisional energy.

4.2 Relaxation vs Thermalization

In our experiment, we have more than 10 times larger ^{87}Rb in atom number compared to ^{7}Li co-trapped in a spherical quadrupole trap. ^{7}Li starts with an initial anisotropy in its momentum distribution. Then we monitor the relaxation process of ^{7}Li in ^{87}Rb bath. Here we clarify the two relevant physical processes, relaxation and thermalization.

- Relaxation: the evolution of ^{7}Li cloud initial momentum anisotropy towards equilibrium through collisions with ^{87}Rb bath.
- Thermalization: ^{7}Li reaches the same temperature as ^{87}Rb through collisions.

Here I quote a paragraph in Ref.[63] with a nice explanation to distinguish the two:

> *The time scale for the two process can be very different for a mass-imbalanced system. In the limit that the ^{87}Rb mass is infinite, a ^{7}Li atom undergoing an s-wave collision with a ^{87}Rb atom would emerge with a completely isotropic momentum probability distribution, so that cross dimensional relaxation occurs in just a single collision for a homogeneous system. In that same collision, the ^{7}Li atom would exchange no energy with the ^{87}Rb atom, meaning that the collisions could not alter the total energy, and hence the temperature, of the ^{7}Li gas.*

> *The true mass ratio between ^{87}Rb and ^7Li (87/7) is large, implying that cross-dimensional relaxation of ^7Li still occurs within on the order of just one collision per atom with the ^{87}Rb gas. In contrast, thermalization to a common temperature of the ^7Li and ^{87}Rb gases requires a larger number of collisions, roughly 2.7/ξ = 9.8, where $\xi = \frac{4m_{Li}m_{Rb}}{(m_{Li}+m_{Rb})^2}$ [61], assuming, again, s-wave interactions with constant cross section.*

To understand the relationship between the relaxation rate and collision rate, as well as the mass ratio dependence, we perform a Monte Carlo simulation with the experimental parameters to simulate this relaxation process and extract the relaxation coefficient α, which relates the cross dimensional relaxation time τ to the collisional rate Γ by $\tau = \frac{\alpha}{\Gamma}$. The details in the Monte Carlo simulation are discussed in later sections. We can obtain an analytic expression between the relaxation time τ and the cross dimensional relaxation cross section σ_{cdr} with the assistance of α. We note that in our experimental setup, and as expected given the large mass ratio, cross dimensional relaxation occurs much faster than does thermal equilibration. Thus, the distributions of both ^{7}Li and ^{87}Rb arrive at thermal equilibrium distribution with their own temperature. We estimate Γ, the per-particle collision rate for atoms of type i colliding with atoms of type j, defined as follows:

$$\Gamma = \frac{1}{N_i}\sigma_{cdr}v_{rel}\int d^3\boldsymbol{r}n_i(\boldsymbol{r})n_j(\boldsymbol{r}) \tag{4.2}$$

Here, $n_{i,j}(\boldsymbol{r})$ are the thermal equilibrium density distributions of atoms i, j, at the temperatures $T_{i,j}$. For Li-Rb collisions, we let i refer to ^{7}Li and j refer to ^{87}Rb , and allow $T_i = T_{Li}$ and $T_j = T_{Rb}$ to differ from one another. For non-degenerate gases in spherical quadrupole trap, we have $n_i(\boldsymbol{r}) = \frac{N_i}{32\pi}(\frac{k}{T_i})^3 e^{-\frac{k\sqrt{(x^2+y^2)/4+z^2}}{T_i}}$, where $k = \frac{\mu B'}{k_B}$, B' is magnetic field gradient along the trap axis, and $\mu = \mu_B/2$ is the atomic magnetic moment at low field in the $|F = 1, m_F = -1\rangle$ hyperfine state, with μ_B being the Bohr magneton. The integral in Eq. 4.2 can be analytically evaluated, $\Gamma = \sigma_{cdr}v_{rel}\frac{k^3}{32\pi}\frac{N_{Rb}}{(T_{Li}+T_{Rb})^3}$, where $v_{rel} = \sqrt{\frac{8k_B}{\pi}\left(\frac{T_{Li}}{m_{Li}} + \frac{T_{Rb}}{m_{Rb}}\right)}$. From all above, we derive an analytical expression for σ_{cdr}:

$$\tau = \frac{\alpha_{LiRb}}{\sigma_{cdr}}\frac{1}{v_{rel}}\frac{32\pi(T_{Li} + T_{Rb})^3}{k^3 N_{Rb}} \tag{4.3}$$

For Rb-Rb collisions, we have:

$$\tau = \frac{\alpha_{RbRb}}{\sigma_{cdr}}\frac{1}{v_{rel}}\frac{32\pi(T_{Rb} + T_{Rb})^3}{k^3 N_{Rb}} \tag{4.4}$$

Here, $v_{rel} = 4\sqrt{\frac{k_B T_{Rb}}{\pi m_{Rb}}}$. The Monte Carlo simulation is done at a series of cross sections σ_{cdr}. For Li-Rb case, $\sigma_{cdr} = 4\pi a^2$, where a=10a_B, 12a_B, 15a_B, 17a_B. For Rb-Rb case, $\sigma_{cdr} = 8\pi a^2$, where a=70a_B, 100a_B, 150a_B, 200a_B. For each σ_{cdr}, with the assistance of experimentally

B'	328 G/cm	249 G/cm	170 G/cm
α_{RbRb}	2.68(6)	-	-
α_{LiRb}	1.72(6)	1.71(9)	1.72(6)

measured temperature and atom number, α is determined. Then these α values are fitted to a straight line to get an averaged α. The errors are statistical from Monte Carlo simulation. The following table reports our Monte Carlo results:

For comparison, the Monte carlo simulation performed by JILA group for ^{6}Li ^{87}Rb ends up with an α=1.64±0.14, for ^{87}Rb ^{87}Rb ends up with 2.67±0.13 [65, 66]. This calculation confirms our understanding of the relaxation from two aspects. First, the relaxation process for ^{7}Li in ^{87}Rb bath is much more efficient than thermalization process. The former requires around 1.7 collisions. The latter requires around 10 collisions. Second, relaxation process is more efficient for the lighter atom in a mass-imbalanced system, compared to the particle with similar mass. ^{7}Li relaxation by colliding with ^{87}Rb takes about 1.7 collisions. ^{87}Rb relaxation with itself takes about 2.7 collisions.

In our experiment, we clearly observe this separation of time scale in relaxation and thermalization. Shown in Fig. 4.5 inset, we can see that ^{7}Li has already relaxed towards equilibrium momentum distribution while remaining at a temperature dramatically different from its ^{87}Rb bath. Moreover, from our initial exploration, we already knew that the cross section is small between the two. Therefore, a cross dimensional relaxation experiment is more suitable for this highly mass imbalanced system, compared to a heat-transfer measurement, which is a common method for cross section measurement [61, 67].

Another observation that is worth mentioning here after we add ^{87}Rb to ^{7}Li in the spherical quadrupole trap is that we observe that the presence of F = 2 ^{87}Rb limits ^{7}Li life time a lot, indicating a large inelastic collision cross section between the two. The presence of $F = 2$ state ^{87}Rb atoms in the magnetic trap was found to be caused by a light leakage of laser light at ^{87}Rb repump frequency around the experimental chamber. Once we extinguished that light more effectively, we observed the lifetime of the trapped ^{7}Li gas was greatly increased. This phenomenon is later confirmed by our later experiment with both species co-trapped in a multimode fiber laser. See discussions in last section of Chapter 3.

4.3 Monte Carlo simulations of cross-dimensional relaxation

In this section, we detail out our procedure in simulating the relaxation process through a Monte Carlo method. The main motivation of this calculation is to do direct comparison to theory. The beauty of cold collisions, where only few partial waves are included, offer a superior platform where relative simple calculations can be made for direct comparison of experiment and theory. In our experiment, we do cross dimensional relaxation experiment for both ^{87}Rb-^{87}Rb and ^{7}Li-^{87}Rb systems. The former benchmarks our experimental method as ^{87}Rb-^{87}Rb cross section is well-known [68]. Theory is able to predict the cross section between ^{7}Li and ^{87}Rb over our experimental collision energy mainly based on previous measurements of Feshbach resonances [69, 70].

Our experiments were performed on gases that collide with low collision energies, on the order of hundreds of μK. At these low values, only the few lowest partial waves need to be considered. Specifically, for ^{7}Li-^{87}Rb system, we need to count s wave and p wave. For ^{87}Rb-^{87}Rb system, we need to count s wave and d wave. Here we detail out our Monte Carlo simulation for ^{7}Li-^{87}Rb system. ^{87}Rb-^{87}Rb system is very similar except that $\sigma_{cdr} = 8\pi a^2$ for homonuclear system. First, we present a detailed overview of this Monte Carlo simulation. Second, we present the angular distribution sampling method in this simulation. Third, we detail out the collision process treatment between ^{7}Li and ^{87}Rb. Fourth, we comment on the deviation of ^{7}Li potential from Eq. 4.1. Finally, we detail out our method for the mean kinetic energy extraction of the system.

Overview

The simulation is done under two assumptions. First, we assume that during the cross dimensional relaxation of ^{7}Li, ^{87}Rb remains in equilibrium and acts as a bath. Second, we assume that the cross-dimensional relaxation of ^{7}Li occurs exclusively through collisions with ^{87}Rb. That is, we neglect completely the rare collisions that may occur between ^{7}Li atoms. The first assumption is justified by the relatively large scattering cross section between ^{87}Rb atoms and relatively small scattering cross section between ^{7}Li and ^{87}Rb, as well as small ^{7}Li atom number (about 1.8×10^7) compared to ^{87}Rb (about $6{\times}10^8$). In experiment, we also directly image ^{87}Rb cloud distribution during ^{7}Li cross dimensional relaxation. Indeed, ^{87}Rb remains in equilibrium during ^{7}Li cross dimensional relaxation. The second assumption is justified by the relative small scattering cross section between ^{7}Li (around 1.76×10^{-14} cm^2), the low density of ^{7}Li compared to ^{87}Rb, and the relatively inefficiency in enhancing energy redistribution through collision between ^{7}Li compared to ^{7}Li and ^{87}Rb. The latter is benefited by the large mass imbalance. We directly measure ^{7}Li cloud thermal distribution through the standard time of flight (TOF) method without the presence of ^{87}Rb experimentally. There is no energy redistribution during 40 s hold in the spherical quadrupole trap, which is around the vacuum life time. (See Fig. 4.1 a).

The simulation is initialized by assigning a random position $\boldsymbol{r}_{Li}$ and velocity $\boldsymbol{v}_{Li}$ to ^{7}Li from separable Gaussian distributions. The standard deviation in position space, σ_{xy} and σ_z, is determined by evolving ^{7}Li in spherical quadrupole trap, under $U(x, y, z)$ mentioned in the main text, for sufficient long time, much longer than the trap period, such that the resultant E_{xy} and E_z match the initial condition of the experiment. The standard deviation in velocity space, $\sigma_{v_{xy}}$ and σ_{v_z}, is determined by experimentally measured E_{xy} and E_z. Here E_{xy} (E_z) is the ensemble-averaged radial (axial) kinetic energy.

Then a ^{87}Rb atom is sampled and assigned a random velocity from Gaussian distribution. The standard deviation of velocity, σ_v, is determined by experimentally measured ^{87}Rb temperature. Then the relative velocity is calculated, including both magnitude v_{rel}=$|\boldsymbol{v}_{Li}-\boldsymbol{v}_{Rb}|$ and direction $\hat{n}_{rel}$=(sinθ_{vrel}cosϕ_{vrel},sinθ_{vrel}sinϕ_{vrel},cosθ_{vrel}). In the collisional energy range of our experiment, only s wave and p wave collisions between ^{7}Li and ^{87}Rb are relevant. The (FEM) - R matrix calculation predicts both s wave and p wave phase shift as a function of v_{rel}. The total collision cross section is calculated by σ_{tot}=$\frac{4\pi}{k^2}$ $(sin^2\eta_{swave}+3sin^2\eta_{pwave})$. We determine ^{87}Rb equilibrium spatial distribution $n_{Rb}(\boldsymbol{r})$ by experimentally measured ^{87}Rb atom number N_{Rb}, ^{87}Rb temperature T_{Rb} and magnetic field gradient B' along the trap axis. We have $n_{Rb}(\boldsymbol{r})$= $\frac{N_{Rb}}{32\pi}\left(\frac{k}{T_{Rb}}\right)^3 e^{-\frac{k\sqrt{(x^2+y^2)/4+z^2}}{T_{Rb}}}$, where $k=\frac{|m_F|g_F\mu_B B'}{k_B}$. The collision rate Γ is calculated by $\Gamma=\sigma_{tot}(v_{rel})\cdot v_{rel}\cdot n_{Rb}(\boldsymbol{r}_{Li})$. The collision probability p_{coll} is given by Γdt. The time interval dt is chosen such that p_{coll} is much smaller than 1. In the current simulation, p_{coll} is set to be in the range of 2×10^{-3} to 5×10^{-3}. If p_{coll} is greater than a random number drawn from a uniform distribution on (0,1), a collision takes place. The relative velocity is rotated into a direction $\hat{n}$=($\sin\theta\cos\phi$, $\sin\theta\sin\phi$, $\cos\theta$), where θ is sampled from probability density distribution P(θ) and ϕ is sampled from a uniform distribution on (0,2π). Here P(θ)$\propto$ $\frac{d\sigma}{d\theta}\sin\theta$.

No matter whether a collision takes place or not, this ^{7}Li atom is evolved in the spherical quadruple trap for dt. The new position vector $\boldsymbol{r}_{Li}$ and velocity $\boldsymbol{v}_{Li}$ are recorded. A new ^{87}Rb is sampled from its equilibrium distribution. Then we ask whether a collision will happen. This process is repeated until the total evolution time reaches t_f, which is chosen to be 80 s. Finally, 10^4 ^{7}Li is involved and released from the spherical quadrupole trap. After a same amount of time of flight as in the experiment, this ^{7}Li cloud distribution is recorded. We extract the mean kinetic energies in each of the three Cartesian directions from this simulated cloud distribution using the same data processing procedure for our experimental data, and will be described in detail in later sub-section. The ratio of axial and radial energies $\frac{E_z}{E_x}$ is plotted against evolution time t and fitted to the ratio of decaying exponentials to get relaxation time τ^{th}. We compare this τ^{th} to the experimentally measured relaxation time τ^{ex}. In the experiment, ^{87}Rb has finite trap life time, with about 14% decreasing in atom number. This finite life time is also considered in the Monte Carlo simulation. We calculate Rb density n_{Rb}(t) using the corresponding N_{Rb}(t).

Angular distribution sampling

In this section, we will go through the mathematical details of angular sampling of ^{7}Li -^{87}Rb collision. The scattering amplitude using partial wave expansion is

$$f(\theta)=\frac{1}{2ki}\sum_{l=0}^{\infty}(2l+1)(e^{2i\eta_l}-1)P_l(\cos\theta) \tag{4.5}$$

From $|f(\theta)|^2$, we get differential cross section $\sigma(\theta,\phi)$. Integrate over (θ,ϕ) to get total cross section σ_{tot}:

$$\begin{aligned}\sigma_{tot} &= \int |f(\theta)|^2 d\Omega \\ &= 2\pi\int_0^\pi \frac{1}{4k^2}|\sum_{l=0}^{\infty}(2l+1)(e^{2i\eta_l}-1)P_l(\cos\theta)|^2\sin\theta d\theta \\ &= 2\pi\int_0^\pi \frac{d\sigma}{d\theta}\sin\theta d\theta\end{aligned} \tag{4.6}$$

In our experiment, only s wave and p wave are relevant.

$$\begin{aligned}\frac{d\sigma}{d\theta}\sin\theta &= \frac{1}{4k^2}|(e^{2i\eta_0}-1)+3(e^{2i\eta_1}-1)\cos\theta|^2\sin\theta \\ &= \frac{1}{k^2}|e^{i\eta_0}\sin\eta_0+3e^{i\eta_1}\sin\eta_1\cos\theta|^2\sin\theta \\ &= \frac{1}{k^2}\sin^2\eta_0(1+9u^2+6u\cos(\eta_0-\eta_1))\sin\theta\end{aligned} \tag{4.7}$$

Here, u=$\frac{\sin\eta_1}{\sin\eta_0}\cos\theta$, η_0, η_1 are corresponding phase shifts for s wave and p wave. P(θ)=$const.(1+9u^2+6u\cos(\eta_0-\eta_1))\sin\theta$. Here, $const.$ is a constant and chosen such that $\int_0^\pi P(\theta)d\theta$=1. Thus we have $const. = \frac{1}{2(1+3(\frac{\sin\eta_1}{\sin\eta_0})^2)}$. This probability density distribution P(θ) is not easy to sample directly as its CDF (cumulative distribution function) is difficult to invert. Therefore, instead of sample this θ distribution directly, we use an indirect method to sample it. This method requires another probability density distribution $g(x)$, which is easy to sample and similar to the target probability density distribution $f(x)$. $f(x)$, $g(x)$ satisfy $sup_x\frac{f(x)}{g(x)} \leq c$. $F(x)$ and $G(x)$ are corresponding CDFs for $f(x)$ and $g(x)$. The following procedure is used to generate random number X from $f(x)$.

1. Generate a random number Y from $g(x)$.
2. Generate a random number U from uniform distribution on (0,1).
3. If U< $\frac{f(Y)}{cg(Y)}$, return X=Y. Otherwise, repeat 1.

Here is a brief proof for this sampling method:

$$\begin{aligned}P(U<\frac{f(Y)}{cg(Y)}) &= P(U<\frac{f(Y)}{cg(Y)}|Y=y)P(Y=y) \\ &= \int_{-\infty}^{\infty}\frac{f(y)}{cg(y)}g(y)dy = \frac{1}{c}\end{aligned} \tag{4.8}$$

$$\begin{aligned}&P(Y\leq y|U<\frac{f(Y)}{cg(Y)}) \\ &= P(U<\frac{f(Y)}{cg(Y)}|Y\leq y)P(Y\leq y)/P(U<\frac{f(Y)}{cg(Y)}) \\ &= \frac{F(y)}{cG(y)}G(y)/(\frac{1}{c}) = F(y)\end{aligned} \tag{4.9}$$

Applying this sampling method to our case, we choose g(θ) to be P$(\theta)_{swave}$=$\frac{1}{2}$sinθ. θ_{swave} is sampled by arccos(1-2·Random(0,1)). Here Random(0,1) is a random number sampled from a uniform distribution on (0,1).

$$\begin{aligned}\frac{P(\theta)}{P(\theta)_{swave}} &= \frac{const.(1+9u^2+6ucos(\eta_0-\eta_1))sin\theta}{\frac{1}{2}sin\theta}\\ &= 2const.(1+9u^2+6ucos(\eta_0-\eta_1))\\ &\leq 2const.(1+9(\frac{sin\eta_1}{sin\eta_0})^2+6|\frac{sin\eta_1}{sin\eta_0}cos(\eta_0-\eta_1)|)\\ &= c\end{aligned} \tag{4.10}$$

Therefore, we have

$$\frac{P(\theta)}{cP(\theta)_{swave}} = \frac{1+9u^2+6ucos(\eta_0-\eta_1)}{1+9(\frac{sin\eta_1}{sin\eta_0})^2+6|\frac{sin\eta_1}{sin\eta_0}cos(\eta_0-\eta_1)|} \tag{4.11}$$

Finally, we summarize our sampling method:

1. Generate a random number Y from P$(\theta)_{swave}$.
2. Generate a random number U from uniform distribution on (0,1).
3. U< $\frac{P(\theta)}{cP(\theta)_{swave}}$, return X=Y. Otherwise, repeat 1.

In Fig. 4.2, we show the sampling result at two different collisional energy using the phase shift predicted by quantum defect theory (QDT) [71]. Fig. 4.2 a shows s wave phase shift η_0 (red) and p wave phase shift η_1 (blue) as a function of relative speed v_{rel}. Fig. 4.2 b plots -$\frac{\sin\eta_0}{k}$(red) and -$\frac{\sin\eta_1}{k}$(blue) in the unit of Bohr radius a_B as a function of relative speed v_{rel}. Fig. 4.2 c shows the θ sampling result at v_{rel}=0.01 m/s, where η_0=0.0012 and η_1=-2.7086×10^{-6}. At this v_{rel}, s wave scattering dominates. The sampling result is proportional to $P(\theta)_{swave} = \frac{1}{2}\sin\theta$. Fig. 4.2 d shows the θ sampling result at v_{rel}=2.1516m/s, where $\eta_0 = -8.6282 \times 10^{-7}$ and $\eta_1 = 0.0632$. Therefore, p wave dominates. The sampling result is proportional to $P(\theta)_{pwave} = \frac{3}{2}\cos^2\theta\sin\theta$.

Collision simulation

To simulate the collision between ^{7}Li and ^{87}Rb, we work in center of mass frame, with the center of mass velocity $\boldsymbol{v}_{\text{center}} = \frac{m_{Rb}\boldsymbol{v}_{Rb}+m_{Li}\boldsymbol{v}_{Li}}{m_{Rb}+m_{Li}}$. Using relative velocity $\boldsymbol{v}_{rel}$=$\boldsymbol{v}_{Rb} - \boldsymbol{v}_{Li}$ and $\boldsymbol{v}_{\text{center}}$ to express ^{7}Li velocity, we have $\boldsymbol{v}_{Li} = \boldsymbol{v}_{\text{center}} - \frac{m_{Rb}}{m_{Rb}+m_{Li}}\boldsymbol{v}_{rel}$. Due to the conservation of total momentum and energy, $\boldsymbol{v}_{\text{center}}$ remains constant before and after collision. The magnitude of the relative velocity v_{rel} stays at a constant value before and after collision. Meanwhile, it rotates to a different direction corresponding to $\theta(v_{rel})$ distribution introduced in the previous section. Therefore, to get the final velocity of ^{7}Li after collision, we first record the initial relative velocity, including both magnitude v_{rel} and direction $\hat{n}_{rel}$. Then we sample the angular distribution $\theta(v_{rel})$ from the θ distribution introduced in the previous section and ϕ from a uniform distribution on (0,2π). The relative velocity $\boldsymbol{v}_{rel}$ rotates from

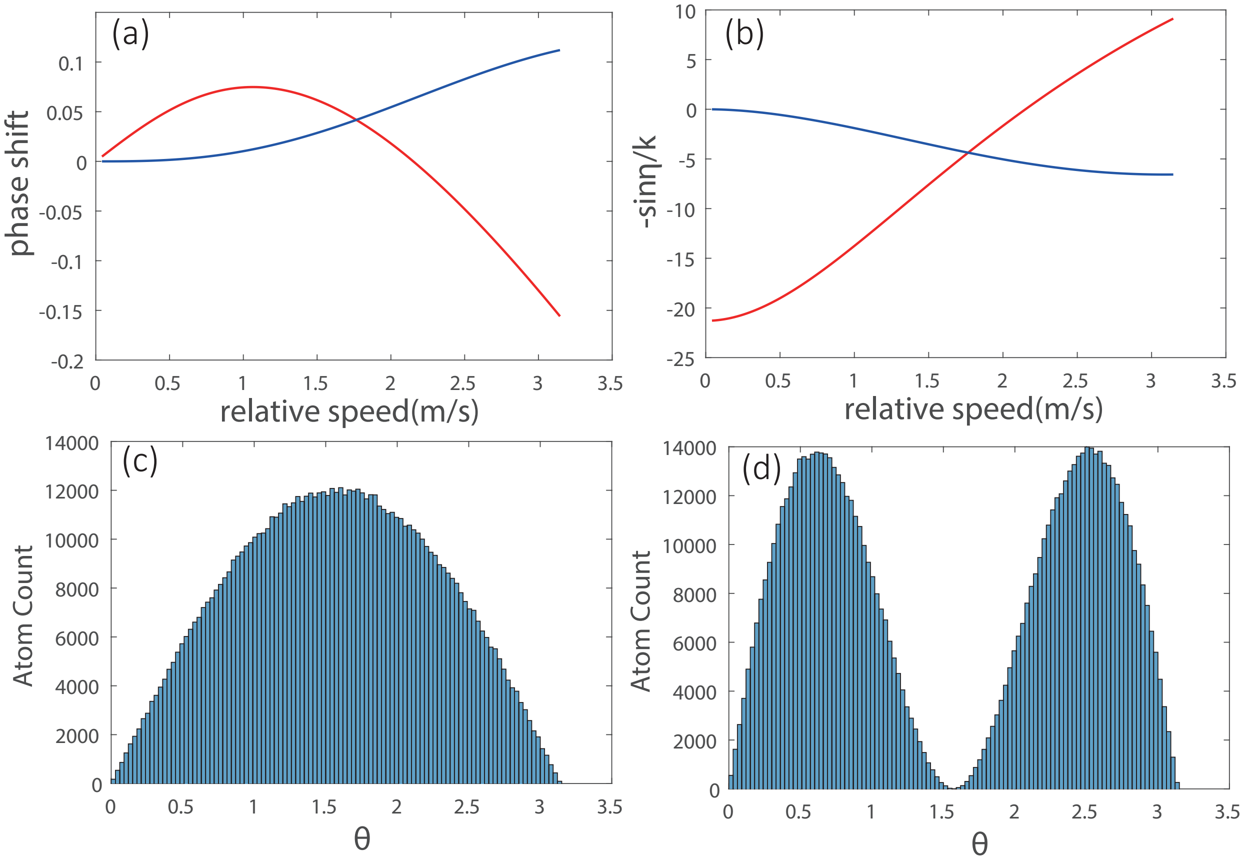

Figure 4.2: Angular sampling. (a) Phase shift predicted by quantum defect theory (QDT) as a function of relative speed v_{rel}. Red: s wave phase shift. Blue: p wave phase shift. (b) -$\frac{\sin\eta}{k}$ in the unit of bohr radius a_B as a function of relative speed v_{rel}. Red: s wave. Blue: p wave. (c) θ sampling result at v_{rel}=0.01m/s. A total of 8×10^5 ^{7}Li is sampled. (d) θ sampling result at v_{rel}=2.1516m/s. A total of 8×10^5 ^{7}Li is sampled.

its initial direction $\hat{n}_{rel}$ to final direction $\hat{n}$ according to the angular sampling result (θ, ϕ). Once the relative velocity $\boldsymbol{v_f}_{rel}$ is determined, the final velocity of ^{7}Li after collision is calculated by $\boldsymbol{v_f}_{Li} = \boldsymbol{v}_{center} - \frac{m_{Rb}}{m_{Rb}+m_{Li}}\boldsymbol{v_f}_{rel}$. Here we go through the mathematical details of each step.

We work in a coordinate system xyz (lab frame), where z is chosen to be parallel to gravity. The initial relative velocity $\boldsymbol{v}_{rel} = (v_{Rbx}-v_{Lix}, v_{Rby}-v_{Liy}, v_{Rbz}-v_{Liz}) = (v_{relx}, v_{rely}, v_{relz})$. The magnitude $v_{rel} = \sqrt{(v_{Rbx}-v_{Lix})^2 + (v_{Rby}-v_{Liy})^2 + (v_{Rbz}-v_{Liz})^2}$. The direction $\hat{n}_{rel} = (\sin\theta_{vrel}\cos\phi_{vrel}, \sin\theta_{vrel}\sin\phi_{vrel}, \cos\theta_{vrel})$. Here θ_{vrel}=arccos($\frac{v_{relz}}{v_{rel}}$). To bring ϕ in the range of (0,2π), we calculate ϕ by:

$$\phi = \begin{cases} arctan\frac{v_{rely}}{v_{relx}} & \text{if } v_{relx} > 0,\, v_{rely} > 0 \\ 2\pi + arctan\frac{v_{rely}}{v_{relx}} & \text{if } v_{relx} \geq 0, v_{rely} < 0 \\ \pi + arctan\frac{v_{rely}}{v_{relx}} & \text{if } v_{relx} < 0 \end{cases}$$

We define a new coordinate system $x'y'z'$, where z' is chosen to be in the direction of $\boldsymbol{v}_{rel}$. In lab frame, $\hat{z'} = \hat{n}_{rel}$=(sinθ_{vrel}cosϕ_{vrel},sinθ_{vrel}sinϕ_{vrel},cosθ_{vrel}), $\hat{y'}$=(-sinϕ_{vrel},cosϕ_{vrel},0), $\hat{x'}$=(cosθ_{vrel}cosϕ_{vrel},cosθ_{vrel}sinϕ_{vrel},-sinθ_{vrel}). The final direction $\hat{n}$ of $\boldsymbol{v}_{rel}$ after a collision in lab frame satisfies: $\hat{n}\cdot\hat{x'}$=sinθcosϕ, $\hat{n}\cdot\hat{y'}$=sinθsinϕ, $\hat{n}\cdot\hat{z'}$=cosθ. Here (θ,ϕ) corresponds to the angular sampling result at this v_{rel}. Finally, we get the relative velocity in lab frame $\boldsymbol{v_f}_{rel}$=$v_{rel}\hat{n}$.

^{7}Li : Breit-Rabi Potential

The potential form in Eq. 4.1 is only accurate in the regime where the linear Zeeman shift is far smaller than the atomic hyperfine splitting. Outside this regime, a more accurate form of the potential can be derived using the Breit-Rabi formula [72]. This intermediate-field correction to the magnetic trap potential is relevant to our trapped ^{7}Li gas, given the small hyperfine splitting in the ^{7}Li ground state.

This relevance can be seen clearly from a simple estimation. For ^{7}Li in spherical quadrupole trap in $|F = 1, m_F = -1\rangle$ at a temperature of 290 μK, according to equipartition theorem for a linear potential, we expect $E_{tot} = (3/2k_BT + 3k_BT)$, which is around 1.3 mK. Compared to the depth of the spherical quadruple trap for this state, which is around 2.6 mK, this energy is already substantial. We perform a more accurate Monte-Carlo type simulation where we propagate 5×10^4 ^{7}Li in the trap with Breit-Rabi potential and record the total energy. The calculation result is shown in Fig. 4.3 a. There we plot the total energy as a function of gas temperature. The solid black line represent the equipartition theorem estimation, which is fairly close to the simulation at low energy, as expected. The total energy deviates to larger values at higher temperature due to a softening of the trapping potential. Fig. 4.3 b shows a comparison of the linear potential and the more accurate Breit-Rabi potential. For ^{7}Li , the difference between the two happens at a relative low field compared to ^{87}Rb . Fig. 4.3 c shows the result of a Monte-Carlo type of simulation with our experimental condition at 170 G/cm. This simulation is done with around 1.5×10^4 particle evolving in the spherical quadrupole trap and shows the magnetic field distribution ^{7}Li cloud samples. Again, it confirms the relevance of Breit-Rabi potential.

This consideration with more accurate potential form for ^{7}Li has two effects in our experiment. First, this softer potential makes the ^{7}Li cloud spread more spatially, thus decreasing the overlap density with ^{87}Rb bath. Second, in our experiment, we image the ^{7}Li cloud distribution after a finite TOF. This TOF is so short that the ^{7}Li cloud does not expand to a size that is much larger than its size in the magnetic trap before expansion. Thus the images contain both spatial and momentum information. To interpret these images

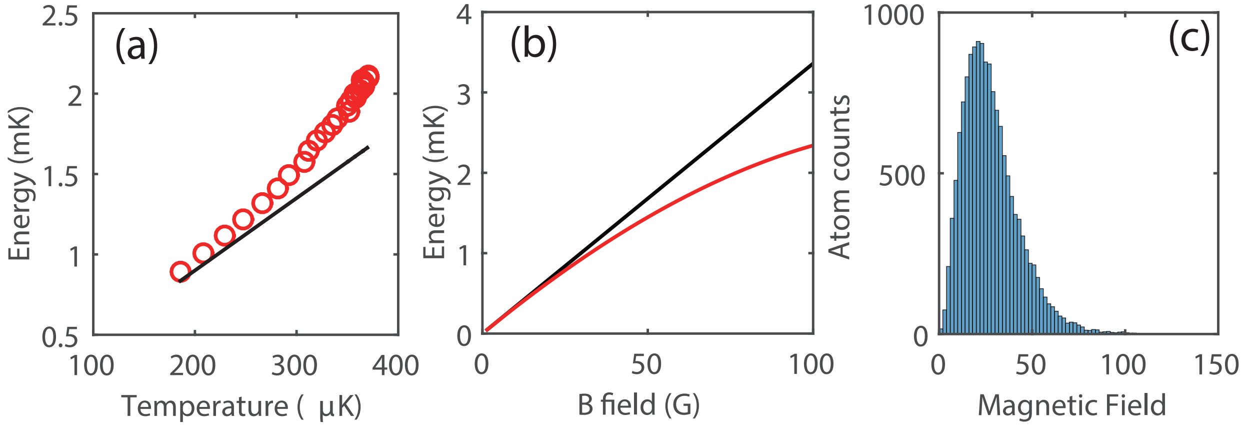

Figure 4.3: Breit-Rabi correction for ^{7}Li . (a) Total energy as a function of ^{7}Li temperature in Breit-Rabi potential. Solid black line is the equipartition theorem for a linear potential. (b) Comparison of potential form. Black: linear potential. Red: with Breit-Rabi correction. (c) Magnetic field distribution ^{7}Li cloud samples for 170 G/cm.

correctly, we need to take into account this more accurate potential, which is the topic for next sub-section.

Mean kinetic energy extraction

In the experiment, as mentioned in the above sub-section, the momentum distribution of ^{7}Li is measured by switching off the magnetic trap, allowing the gas to expand for a finite amount of time, and then imaging its distribution through absorption image. Due to this finite TOF, the distribution probed in the experiment contains both spatial and momentum of the gas held in the magnetic trap. Specifically, the in-plane kinetic energy E_{xy} depends on both the cloud width σ_{xy} along one in-plane axis after a finite TOF and also the axial kinetic energy E_z. Meanwhile, the axial kinetic energy E_z is a function of the cloud width σ_z along z after a finite time of flight and the in-plane kinetic energy E_{xy}:

$$\begin{aligned} E_{xy} &= f_1(E_z, \sigma_{xy}) \\ E_z &= f_2(E_{xy}, \sigma_z) \end{aligned} \tag{4.12}$$

To figure out the function form of f_1 and f_2, we numerically simulate a series of ^{7}Li clouds with different E_{xy} and E_z, let them evolve in the spherical quadrupole trap for a time period much longer than the trap period until they reach a steady state, and then turn off the magnetic trap, after a same amount of TOF as that spent in the experiment, record the ^{7}Li clouds distributions. Specifically, the gradual turn-off of the trapping fields is counted in this numerical simulation. The initial ^{7}Li cloud distribution, including both spatial and momentum, is sampled from Gaussian distribution, which is a good description of ^{7}Li D$_1$ gray molasses. Under the assumption that both f_1 and f_2 are smooth functions, we numerically calculate f_1 and f_2 through interpolation. Once f_1 and f_2 are known, with experimentally measured σ_{xy} and σ_z, we extract E_{xy} and E_z. The error from this extraction (around 1.5%) is included as systematic error and propagated to contribute to the systematic error of the measured σ_{cdr}.

We then make a more refined comparison between experiment and theory accounting for both the anisotropy and energy-dependence of the differential cross section, including contributions from both s wave and p wave. The simulated cloud's starting condition is chosen to be the same as that in the experiment. Then this cloud is evolved under collisions with ^{87}Rb governed by the differential cross section in the spherical quadrupole trap. After the same amount of time of evolution as in the experiment, this simulated cloud is released from the trap. After a same amount of time of flight, its distribution is recorded. With f_1 and f_2, its E_{xy} and E_z are calculated and compared to the real values.

Because of the energy-dependence of cross section and the existence of collisionless trajectories, the low energy ^{7}Li and those with better overlap with ^{87}Rb tend to collide more frequently, leading to a deviation of the cloud distribution from Gaussian. Therefore, a deviation of E_{xy} and E_z from their real values is expected. Specifically, we observe a small reduction, about 4%, in the ratio of E_z/E_{xy}, leading to an around 20% faster relaxation rate. As our experiment is performed after a finite TOF and $E_{xy/z}$ is reconstructed through f_1 and f_2, we compare our experimental result with the reconstructed theoretical data from a finite TOF.

4.4 Summary of published results

In this section, I summarize the results published in Ref.[63]. The experimental results there are analyzed by the methods introduced in the previous sections. All figures presented here are from Ref.[63] except Fig. 4.7 and Fig. 4.8.

1) ^{87}Rb-^{87}Rb cross dimensional relaxation (CDR) measurement.

2) ^{7}Li-^{87}Rb CDR measurement.

3) Non-exponential relaxation of ^{7}Li.

4) Theoretical investigation.

^{87}Rb-^{87}Rb cross dimensional relaxation (CDR) measurement: In this experiment, we placed around 1.7×10^7 ^{87}Rb atoms in the spherical quadrupole trap with B'=328 G/cm, at a temperature around 220 μK, and observed their collisional thermalization from an initial distribution where E_z is about 20% larger than E_x. Fig. 4.4 shows the experimental measurements and the Monte Carlo simulated results using the theoretical predicted ^{87}Rb-^{87}Rb cross sections. The good agreement between the experiment and theory benchmarks our experimental method.

^{7}Li-^{87}Rb CDR measurement: In these experiments, we monitored the evolution of the momentum distribution of around 2×10^7 ^{7}Li atoms, co-trapped with about 6×10^8 ^{87}Rb atoms. There, we observed the initial momentum anisotropy of ^{7}Li gas began to relax toward an isotropic distribution through collisions with the ^{87}Rb atoms, shown in Fig. 4.5. The comparison of the experiment (red circles) and Monte Carlo simulation (gray circles) using the theoretically predicted cross section reveals the fact that the relaxation rate measured by our experiment is significantly larger than the theoretical prediction.

Non-exponential relaxation of ^{7}Li: The relaxation of ^{7}Li momentum distribution should be non-exponential. There are two reasons. First, at the collisional energy probed by our experiment, the cross-section has a rapid energy dependence, see what predicted by theory (Fig. 4.6), leading to the difference in the relaxation rate for ^{7}Li in different velocity class. Second, there exist particle trajectories for trapped ^{7}Li atoms, e.g. those with large axial angular momentum, whose trajectory-averaged rubidium gas density is lower than the volume average. ^{7}Li atoms in such trajectories collide less frequently than those that experience higher ^{87}Rb gas density. The evidence of this non-exponential decay is found in our Monte Carlo simulation with theoretically predicted cross section, shown in Fig. 4.7, where we find that the fitted value for τ varies with the range of data used for the fit, with later-time data giving systematically longer relaxation times.

Theoretical investigation: The theoretical investigation is done by our theory collaborators Yimeng Wang and Chris Greene. Fig. 4.6 shows the s wave and p wave interspecies cross section for ^{7}Li-^{87}Rb as a function of collisional energy. These cross sections are calculated by a finite element method (FEM)-R matrix calculation [73]. The shaded gray area represents the smallest and largest theoretically allowable s wave cross section with $\chi_5^2 < 20$. Here $\chi_5^2 = \sum \frac{(B_{\mathrm{calc}} - B_{\mathrm{exp}})^2}{(\delta B)^2}$, where the sum is taken over the five measured Fano-Feshbach resonances, with B_{calc} being the theoretically predicted and B_{exp} the experimentally measured magnetic field position of the resonance, and $\delta B = 0.5$ G being the experimentally reported uncertainty [70].

This theoretical investigation is done at low fields. As the scattering cross section is a function of magnetic field, we study the field dependence of cross section for s wave, shown in Fig. 4.8. This investigation shows the cross section has a weak field dependence. It only changes about 10% up to 60 G, which covers the entire sampling range of our experiment (See Fig. 4.3 c).

On top of the cross sections, we plot our experimentally determined $\sigma_{\mathrm{cdr}}^{\mathrm{exp}}$s (red circles) and the Monte Carlo simulated $\sigma_{\mathrm{cdr}}^{\mathrm{th}}$s (gray circles) at the averaged collisional energy in our experiment, with $\sigma_{\mathrm{cdr}}^{\mathrm{exp}}$ around 2.5 times of the simulated $\sigma_{\mathrm{cdr}}^{\mathrm{th}}$.

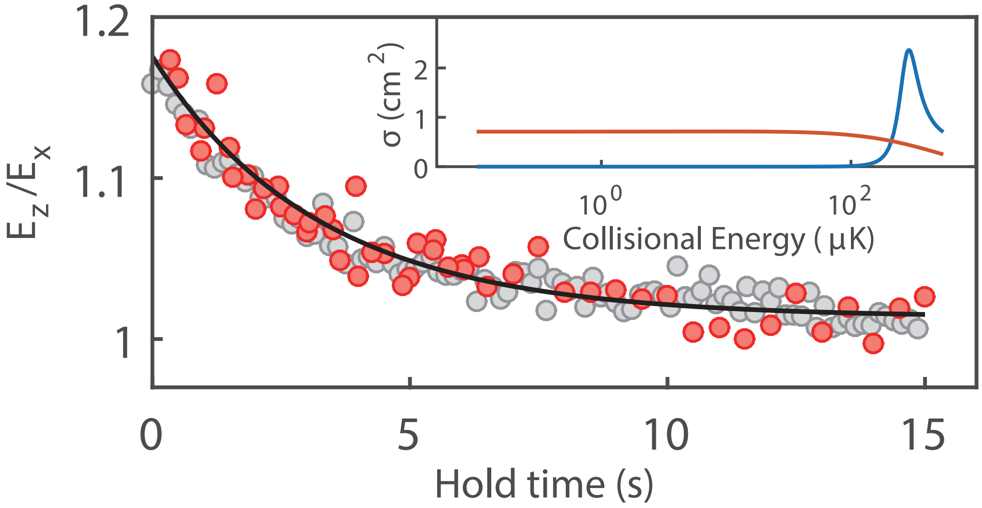

Figure 4.4: Cross-dimensional relaxation of ^{87}Rb after introducing an anisotropy between the kinetic energies in the axial (E_z) and radial (E_x) directions. Measured (red circles) and simulated (gray circles) ratios E_z/E_x vs. Hold time in the $B' = 328$ G/cm spherical quadrupole trap. The inset shows the theoretically calculated ^{87}Rb-^{87}Rb cross section as a function of collisional energy [74]. The solid orange line represents the s wave cross section. The solid blue line represents the d wave cross section.

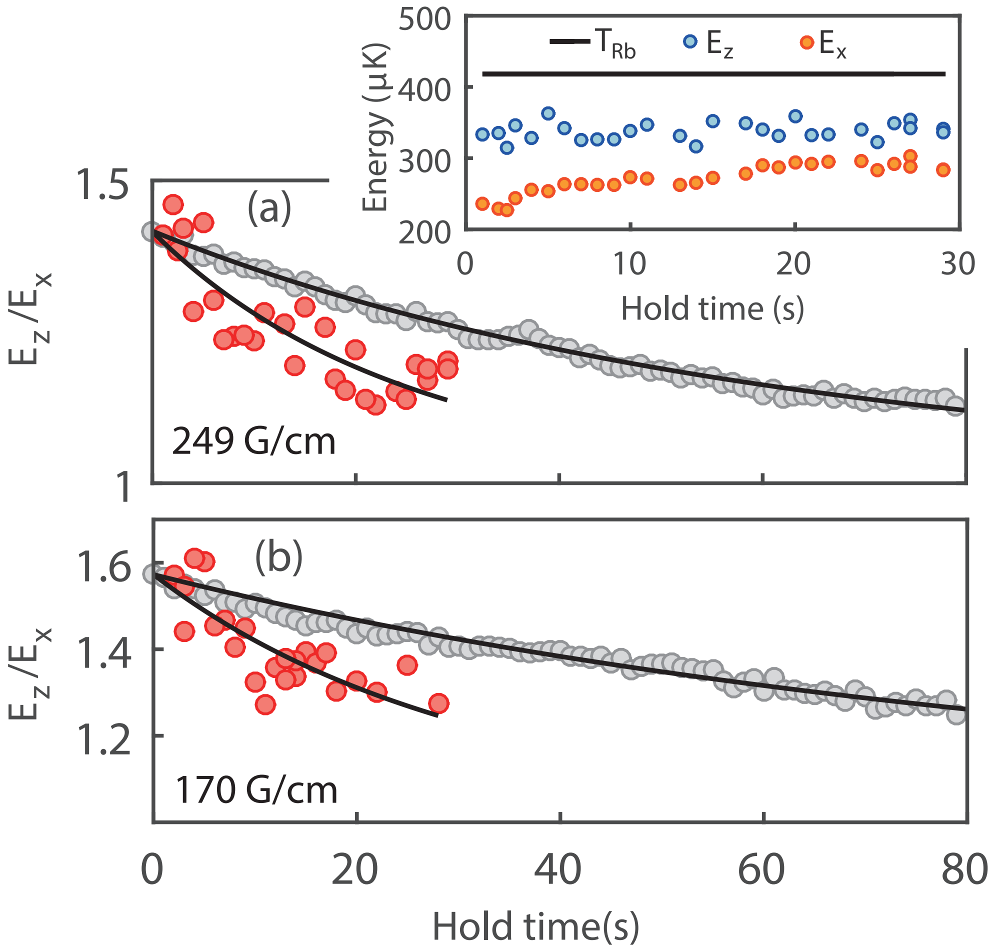

Figure 4.5: Cross-dimensional relaxation of ^{7}Li atoms within a co-trapped ^{87}Rb gas. Red circles show the measured kinetic energy ratio (E_z/E_x) for the lithium gas. Gray circles show results of Monte Carlo simulations accounting for experimental parameters and the theoretically predicted energy-dependent differential cross section derived using the ^{7}Li-^{87}Rb molecular potential modeled in Ref. [70]. Results at two trap strengths are shown: $B' = 249$ G/cm (a) and $B' = 170$ G/cm (b). Inset: neither E_z (blue) nor E_x (orange), at $B' = 249$ G/cm trap strength, reaches the isotropic kinetic energy of the co-trapped rubidium gas (solid black line) during the accessible evolution time.

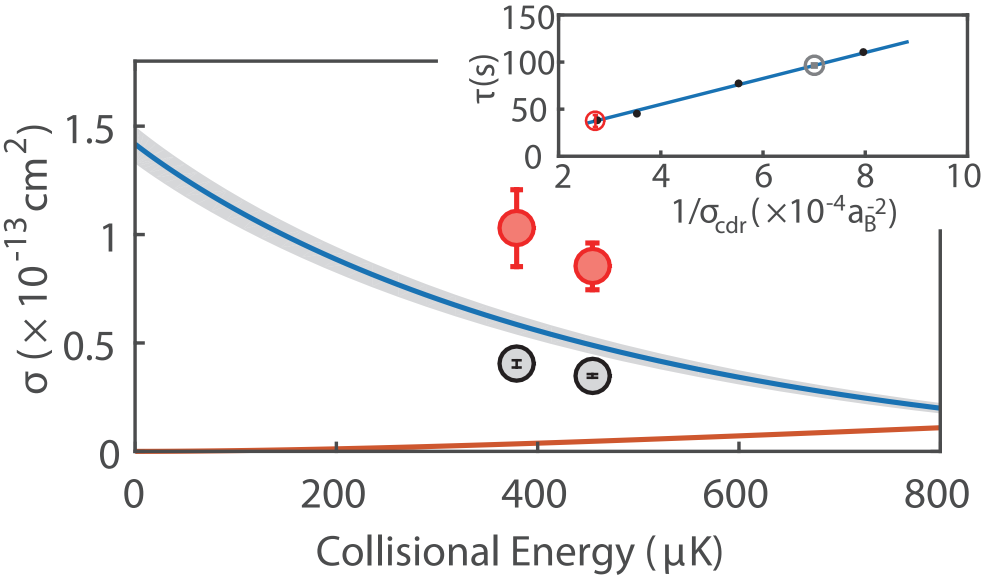

Figure 4.6: Comparison between experimental measurements and theoretically predicted cross section for ^{7}Li-^{87}Rb collisions. The solid blue (orange) lines give the s-wave (p-wave) cross section calculated using the Maier *et al.* model potential. The shaded gray area represents the smallest and largest theoretical allowable s-wave cross section with $\chi_5^2 < 20$. For comparison, we show σ_{cdr} obtained either experimentally (red circles, with one-sigma statistical error bars) or theoretically (gray circles, based on the Maier *et al.* model potential). These are plotted at the thermally averaged collision energies determined by experimental conditions. The corresponding cross-dimensional relaxation times derived from experiment and theory are shown in the inset (same color scheme). We show also Monte Carlo simulated results (black symbols) under experimental conditions using a series of energy-independent isotropic cross sections, from which a linear relationship between $\sigma_{\mathrm{cdr}}^{-1}$ and the cross-dimensional relaxation time τ is obtained.

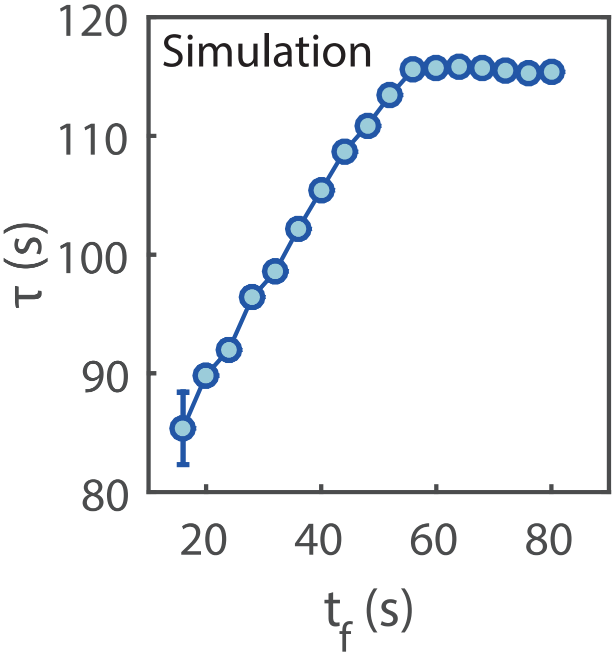

Figure 4.7: Non-exponential behavior of cross-dimensional relaxation. The ratio E_z/E_x for Li atoms cotrapped with Rb atoms (Fig. 4.5 b, $B' = 170$ G/cm) is fitted with the exponential relaxation function over a time interval ranging from 0 to t_f. The relaxation time τ obtained is plotted for fits to Monte Carlo simulation data. Error bars are statistical.

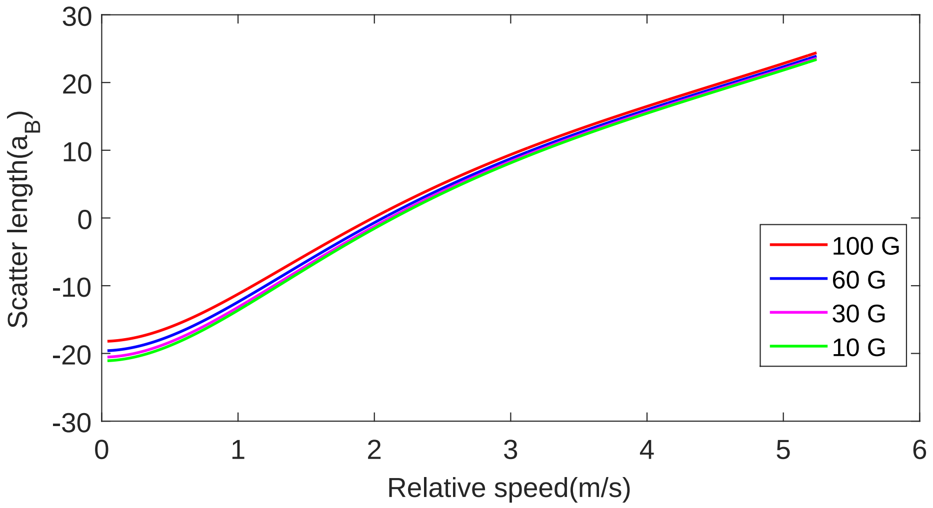

Figure 4.8: s wave cross section as a function of collisional energy for different magnetic field ranging from 10 G to 100 G.

4.5 Conclusion

We have characterized collisions at a collision energy that is in the range of several 100's of μK by observing cross-dimensional relaxation of gases trapped in a spherical quadrupole magnetic trap. Several features of this mass-imbalanced system have been addressed and observed, including the non-ergodicity of the spherical-quadrupole trap, a separation of time scale between relaxation and thermalization, and a non-exponential relaxation of energy anisotropy. The measured rates, however, are significantly faster than theory predication. A detailed theoretical investigation shows that it is hard to incorporate our measurements to the existing model potential. Therefore, more measurements are needed to improve our understanding both experimentally and theoretically. For instance, by accelerating the two clouds at a different collisional energy and then imaging the collisional halo, one should be able to determine the phase shift for different partial waves as well as Ramsauer minimum [75]. Experimental measurements on Fano-Feshbach resonances in ^{7}Li-^{87}Rb collisions could be refined by applying methods such as rf-modulation or interferometric measurements [76] to identify and measure the energies of shallow molecular bound states. Such experiments could supplement the existing measurements [70] to determine the resonance positions with more certainty.

Chapter 5

Thermal spin dynamics in heteronuclear atomic mixtures

Control and manipulation of the spinor degree of freedom, associated with both electrons and atoms, is of both fundamental and applied importance, and is being intensely studied in physics today. The former is related to the highly visible subfield in solid state system, spintronics [77]. The latter demonstrates itself in the study of spinor quantum gases [78], where topics like quantum magnetism [79], spin exchanging and mixing dynamics [29, 80–82], domain formation [30, 83], etc, are addressed and studied.

Typical questions that are posed in both fields for fundamental studies are (a) how to polarize a spin system? (b) how does the spin evolve in the system? (c) how can spin be detected? The answers to these questions are in some cases the same, and in other cases different, for case of either electronic or atomic spin systems. Optical pumping techniques where circularly polarized photons transfer their angular momentum to electrons or atoms are widely adopted. Meanwhile, electrical spin injection is more desirable for device application in spintronics. After the initialization of non-equilibrium spin, it will evolve/relax back to equilibrium. Spin detection, in spintronics, relies on sensing the changes in the signals caused by the presence of non equilibrium spin. On the other hand, in cold atom systems, techniques like Stern-Gerlach method where magnetic field gradient is applied to spatially separate states with different magnetic moments [29], as well as state-sensitive microwave addressing, are frequently applied.

This chapter describes our work on spin dynamics in a thermal heteronuclear atomic mixtures formed by ^{7}Li and ^{87}Rb . We address (a) by using the two color optical pumping method to polarize both ^{7}Li and ^{87}Rb . For (c), we use two different techniques. For ^{87}Rb gases, we use state-sensitive microwave excitation and absorption imaging [1]. For ^{7}Li gases, we develop a different technique where different Zeeman sublevels are culled from the gas before imaging the remaining atomic populations. In the next few sections, we start from the theoretical understanding of the spin-dependent interaction of heteronuclear atomic mixtures deep in s-wave regime. Then we discuss our experimental scheme and a theoretical model in studying and understanding this spin-dependent dynamics. Next, we show our experimental techniques for spin initialization and detection, as well as our experimental results in studying ^{7}Li spin dynamics in ^{87}Rb bath, and the comparison between experiment and theory. Finally, we discuss our efforts in searching for coherence and future aspects along this heteronuclear spinor gases research line.

5.1 Theoretical Background: Heteronuclear spin-dependent interaction

For binary mixtures of atomic spin-1 gases, at the low energy limit where only s-wave is relevant, the two-body interaction can be well described by the contact interactions, which stay invariant under both spatial and spin rotation [78]:

$$V_{\text{LiRb}}(\boldsymbol{r}) = \sum_{F=0}^{2f} g_F \left|F, m_F\right\rangle \left\langle F, m_F\right| \delta(\boldsymbol{r}) \tag{5.1}$$

Here the coupling constants $g_F = 2\pi\hbar^2 a_F/\mu$ are determined by the s-wave scattering lengths a_F of the corresponding F channels and the two-body reduced mass μ, with $\hbar$ the reduced Planck's constant.

Collisions under this interaction potential have two different flavors. First, this two-body interaction can give rise to a mean-field effect [29, 80–82, 84], leading to a coherent spin population oscillation, through spin-dependent forward scattering, where $(k_1, k_2) = (k'_1, k'_2)$. Here $\hbar k$ and $\hbar k'$ are initial and final momentum for this two-body collision, with labels 1 and 2 representing the two particles involved in the collision. The strength of this mean field interaction is proportional to Δa_F. Here Δa_F is the difference in the a_Fs. For example, $\Delta a_F = a_{F=2} - a_{F=1}$ for spin exchange process introduced below, and estimated to be around 6 HZ for our density. The prerequisite to observe this oscillation is spin coherence. As discussed below, we were unable to maintain transverse spin coherences in our system for more than a few ms, owing to a lack of sufficient control over magnetic field inhomogeneity. Because of this, we were not able to observe coherent spin oscillations that would result from this forward-scattering effect.

A second manifestation of the interactions between atoms is from non-forward scattering, where $(k_1, k_2) \neq (k'_1, k'_2)$. For this non-forward scattering, we further classify it into two categories, spin-conserving and spin-nonconserving scattering process. For the former, we have $(s_1, s_2) = (s'_1, s'_2)$, with s and s' are initial and final spin state for the two-body collision. The collision rate for this type of collision is proportional to a_F^2, and is estimated to be around 3 HZ at our density with the current available theoretical model. This scattering process leads to a momentum redistribution without changing spin configuration. For the latter, we have $(s_1, s_2) \neq (s'_1, s'_2)$. This process can lead to interspecies spin relaxation, which is the topic of our current experiment. Here we detail out our derivation in the spin-dependent cross section.

Let us consider some principles from two-body quantum scattering. One can write the asymptotic wave function at $r \to \infty$ for two colliding particles in the form:

$$|\psi(\boldsymbol{r}, \boldsymbol{s_1}, \boldsymbol{s_2})\rangle \xrightarrow{r\to\infty} e^{ikz}\,|x_i\rangle + f(\theta,\phi)_{fi}\,|x_f\rangle\,\frac{e^{ikr}}{r} \tag{5.2}$$

Here $|x_i\rangle$ is the incoming spin state, $|x_f\rangle$ is the outcoming spin state. The corresponding cross section $\sigma(\theta,\phi)_{fi} = |f(\theta,\phi)_{fi}|^2$.

Our experiment is performed with atoms at a collision energy of 10's of μK, thus deep in the s-wave regime, and well-described by the above two body contact interaction V_{LiRb}. With this contact interaction under low energy collision events, we can apply Born approximation:

$$f(\theta,\phi)_{fi} = -\frac{\mu}{2\pi\hbar^2}\int e^{-i\boldsymbol{q}\cdot\boldsymbol{r}'}\,\langle x_f|\,V(\boldsymbol{r}', \boldsymbol{s_1}, \boldsymbol{s_2})\,|x_i\rangle\,d\boldsymbol{r}' \tag{5.3}$$

Here $\boldsymbol{q}$ is the incoming particle momentum change by scattering. Inserting the two body contact interaction:

$$f(\theta)_{fi} = -\sum_{F=0}^{2f}\langle x_f|\,a_F\,|F, m_F\rangle\,\langle F, m_F|x_i\rangle \tag{5.4}$$

And, $\sigma_{fi} = 4\pi|f(\theta)_{fi}|^2$.

The spin-dependent interaction is written here in terms of scattering amplitudes for collisions with different total spin F. However, it is hard to develop an intuition from this expression as written. Instead, let us consider several different allowed collision processes. We note that the collision interaction is spherically symmetric, and, hence, that it conserves the total projection of the two-body angular momentum onto a chosen quantization axis (call it $\mathbf{z}$). From this statement, we identify three elementary processes that conserve the total m_F of the colliding pair shown in Fig. 5.1:

$$\begin{aligned}
&\mathrm{Exchange}: |1_{Rb}, 0_{Li}\rangle \leftrightarrow |0_{Rb}, 1_{Li}\rangle\,, |{-1}_{Rb}, 0_{Li}\rangle \leftrightarrow |0_{Rb}, -1_{Li}\rangle\\
&\mathrm{Mix}: |1_{Rb}, -1_{Li}\rangle \leftrightarrow |0_{Rb}, 0_{Li}\rangle\,, |{-1}_{Rb}, 1_{Li}\rangle \leftrightarrow |0_{Rb}, 0_{Li}\rangle\\
&\mathrm{Singlet-pairing}: |1_{Rb}, -1_{Li}\rangle \leftrightarrow |{-1}_{Rb}, 1_{Li}\rangle
\end{aligned} \tag{5.5}$$

Here, $|m_{Rb}, m_{Li}\rangle$ represents the m_F sublevel of F = 1 manifold of ^{7}Li and ^{87}Rb. To obtain cross sections for the three spin process, we work under two different basis.

$$\begin{aligned}
&1: \text{Uncoupled hyperfine Basis}: |f_{Li}, m_{f_{Li}}; f_{Rb}, m_{f_{Rb}}\rangle\\
&2: \text{Coupled hyperfine Basis}: |F, m_F, f_{Li}, f_{Rb}\rangle
\end{aligned} \tag{5.6}$$

First we consider spin exchange process σ_{ex}. We consider the incoming state under basis 1, $|x_i\rangle = |1,1;1,0\rangle$. The outcoming state under spin exchange is $|x_f\rangle = |1,0;1,1\rangle$. Expanding $|x_i\rangle$ and $|x_f\rangle$ under basis 2:

$$\begin{aligned}
|x_i\rangle &= \frac{1}{\sqrt{2}}\,|2,1,1,1\rangle + \frac{1}{\sqrt{2}}\,|1,1,1,1\rangle\\
|x_f\rangle &= \frac{1}{\sqrt{2}}\,|2,1,1,1\rangle - \frac{1}{\sqrt{2}}\,|1,1,1,1\rangle
\end{aligned} \tag{5.7}$$

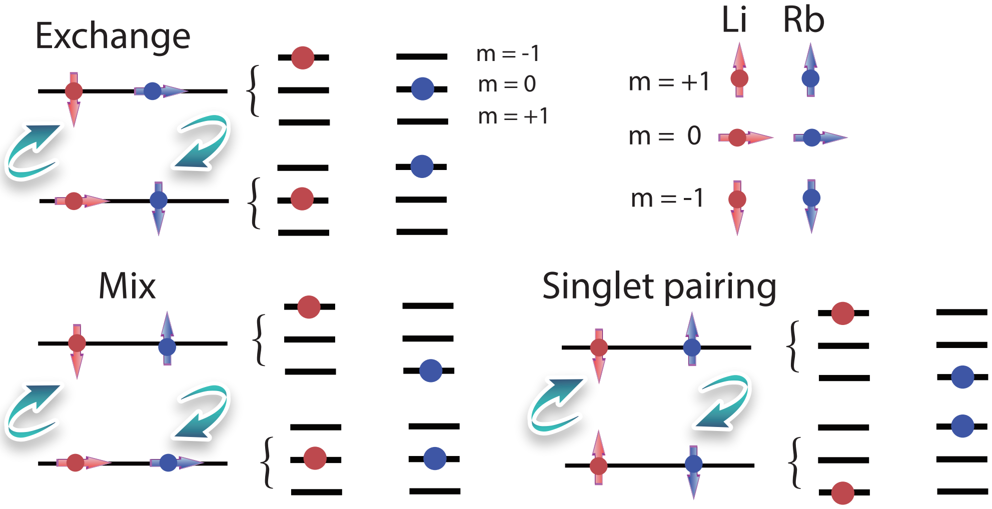

Figure 5.1: Three heteronuclear elementary collision processes.

Using Eq. 5.4, we get $|f(\theta)_{ex}|^2 = \frac{1}{4}(a_{F=2} - a_{F=1})^2$. Thus $\sigma_{ex} = \pi(a_{F=2} - a_{F=1})^2$.

Second we consider spin mixing σ_{mix}. We consider the incoming state under basis 1, $|x_i\rangle = |1,1;1,-1\rangle$. The outcoming state under spin mixing is $|x_f\rangle = |1,0;1,0\rangle$. Expanding $|x_i\rangle$ and $|x_f\rangle$ under basis 2:

$$\begin{aligned} |x_i\rangle &= \frac{1}{\sqrt{6}}|2,0,1,1\rangle + \frac{1}{\sqrt{2}}|1,0,1,1\rangle + \frac{1}{\sqrt{3}}|0,0,1,1\rangle \\ |x_f\rangle &= \sqrt{\frac{2}{3}}|2,0,1,1\rangle - \frac{1}{\sqrt{3}}|0,0,1,1\rangle \end{aligned} \tag{5.8}$$

Using Eq. 5.4, we get $|f(\theta)_{mix}|^2 = \frac{1}{9}(a_{F=2} - a_{F=0})^2$. Thus $\sigma_{mix} = \frac{4\pi}{9}(a_{F=2} - a_{F=0})^2$.

Third we consider singlet pairing σ_{sp}. We consider the incoming state under basis 1, $|x_i\rangle = |1,1;1,-1\rangle$. The outcoming state under singlet pairing is $|x_f\rangle = |1,-1;1,1\rangle$. Expanding $|x_i\rangle$ and $|x_f\rangle$ under basis 2:

$$\begin{aligned} |x_i\rangle &= \frac{1}{\sqrt{6}}|2,0,1,1\rangle + \frac{1}{\sqrt{2}}|1,0,1,1\rangle + \frac{1}{\sqrt{3}}|0,0,1,1\rangle \\ |x_f\rangle &= \frac{1}{\sqrt{6}}|2,0,1,1\rangle - \frac{1}{\sqrt{2}}|1,0,1,1\rangle + \frac{1}{\sqrt{3}}|0,0,1,1\rangle \end{aligned} \tag{5.9}$$

Using Eq. 5.4, we get $|f(\theta)_{sp}|^2 = \frac{1}{36}(a_{F=2} - 3a_{F=1} + 2a_{F=0})^2$. Thus $\sigma_{sp} = \frac{\pi}{9}(a_{F=2} - 3a_{F=1} + 2a_{F=0})^2$. Similar calculation on the three elementary collision processes in heternuclear system can be found in Ref. [85].

As discussed in Chapter 4, the theory describing Li-Rb collisions is well developed. In particular, starting from a model potential such as that presented by Maier *et al.* that takes into account the measured positions of Feshbach resonances and some photoassociation data,

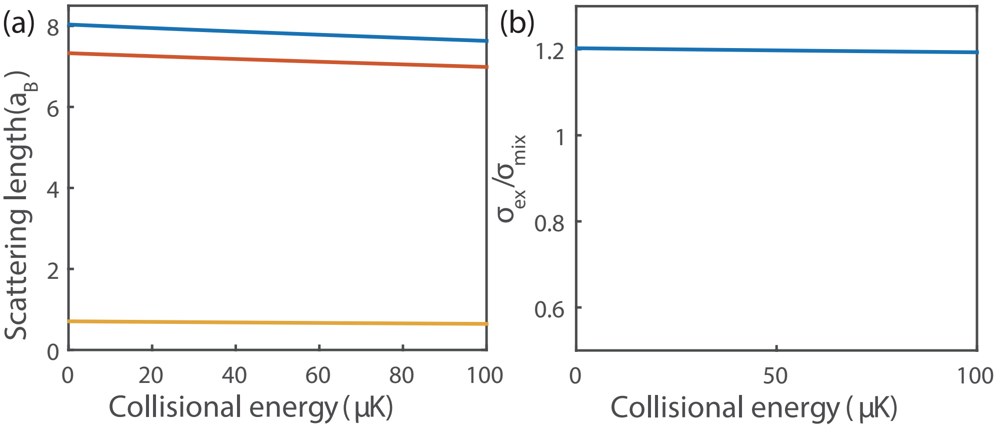

Figure 5.2: Energy dependence of the spin-dependent interaction. (a): Blue, red and yellow solid lines mark the s wave scattering length for exchange, mix and singlet pairing process. (b): The ratio of exchange cross section over mix cross section as a function of collision energy.

one can also obtain theoretical predictions for the spin-dependent scattering lengths a_0, a_1 and a_2. This calculation is done using the following procedures. At near-zero field, total F is a good quantum number. With (FEM)-R matrix calculation, we are able to obtain the S-matrix for a given collision process. These a_Fs are determined by the eigenvalues of the S-matrix.

Let us make two observations about these theoretical results. First, our experiments on optically trapped Li-Rb gas mixtures are performed at gas temperatures of 10's of μK. We see in Fig. 5.2 that the scattering lengths, and the corresponding scattering cross sections for spin-changing collisions, are almost constant over this energy range. This result greatly simplifies the theoretical modeling and comparison of our experiment.

Second, the take-away message of our cross-dimensional relaxation measurement is that, as far as we can tell, there seems to be something inconsistent between the experiment and theory. In light of this apparent discrepancy, we can regard the measurements of the cross-sections for spin-changing collisions as being a new bit of information in constraining our models for the LiRb molecular potential.

5.2 Experimental scheme and theoretical modeling

To study the heteronuclear spin dynamics between ^{7}Li and ^{87}Rb and measure the spin-dependent parameters corresponding to the three elementary collision processes, we prepare a cold mixture of ^{7}Li and ^{87}Rb co-trapped in a spin-independent optical dipole trap, with both gases in their $f = 1$ manifolds, with $T_{Li} = 36$ μK and $T_{Rb} = 87$ μK, and with the total ^{87}Rb number around ten times of ^{7}Li number.

We choose three different settings of the initial spin of the two gases in order to highlight different collision processes. In the first configuration, we have most ^{87}Rb population in $|-1\rangle$ and $|0\rangle$ state with around 10% in $|+1\rangle$. This configuration is the most sensitive to spin-exchange process. In the second configuration, we have 80% ^{87}Rb population in $|+1\rangle$. This configuration probes most the mix and singlet-pairing process. The third configuration leaves ^{87}Rb spin unpolarized. For all configurations of ^{87}Rb bath, we initialize ^{7}Li spin with 80% to 100% population in $|-1\rangle$ and then watch the evolution of ^{7}Li spin in ^{87}Rb spin bath. During this evolution, ^{87}Rb bath stays almost the same with around 15% loss in total atom number.

With the theoretical understanding of spin-dependent interaction described in previous section, we can develop a simple rate-equation model to describe the expected dynamics of spin populations in the co-trapped atomic gases. This rate-equation approach is done under three assumptions.

First, there is no transverse spin coherences in the system. This assumption is valid considering the kHZ decoherence rate for transverse coherence and the seconds-long time scale of our experiment.

Second, this rate equation model deals with atomic population only, and therefore do not trace the evolution of atoms at specific locations and momenta. This treatment is valid according to the following arguments. First, the fast radial trap frequency, around 2.6 kHZ for ^{87}Rb , which is the fastest timescale of this mixture system, induces an effective radial motion averaging for both species, removing the radial spatial dependence of the interaction. Second, the much higher ^{87}Rb -^{87}Rb collision rate compared to the axial trap frequency, which is around 15.6 HZ, guarantees an axial local equilibrium for ^{87}Rb . Third, the trap-induced axial motion of ^{7}Li is considerably faster than the interspecies spin relaxation processes, which again averages the spatial dependence of the interaction. The efficient momentum redistribution effectively removes the existence of ^{7}Li trajectories, whose trajectory-averaged ^{87}Rb gas density is lower than the volume average, as confirmed by our Monte Carlo simulation, where we evolve ^{7}Li particles in an equilibrium ^{87}Rb spin bath with interspecies spin-dependent collisions in the 3D harmonic trap. Together with the weak energy-dependence of the cross section, we are able to relate the relaxation rates to the corresponding cross section with a simple formula:

$$\Gamma = \sigma n_{overlap} v_{rel} \tag{5.10}$$

Here Γ is relaxation rate, σ is cross section, $n_{overlap}$ is overlap density between ^{7}Li and ^{87}Rb in optical dipole trap, v_{rel} is relative speed of the two.

Third, the ^{87}Rb gas is treated as a stationary spin bath, which is approximately correct for our system with the ^{87}Rb atom number ten times larger than the ^{7}Li number. The deviation from the stationary spin bath assumption will be discussed in later section.

Hence, we define Γ_{ex}, Γ_{mix} and Γ_{sp} as rates for the three processes, spin exchange, spin mixing and singlet pairing. $\boldsymbol{P} = (P_p, P_0, P_m)^\intercal$ are dynamic population percentages of ^{7}Li in the $|+1\rangle$, $|0\rangle$, $|-1\rangle$ states, correspondingly. $\boldsymbol{p} = (p_p, p_0, p_m)^\intercal$ are static population percentage of ^{87}Rb in the three corresponding m_F sublevels. For exchange process, we define spin exchange matrix $\mathbf{M}_{ex} = \begin{pmatrix} -p_0 & p_p & 0 \\ p_0 & -p_m - p_p & p_0 \\ 0 & p_m & -p_0 \end{pmatrix}$. In the same manner, we have spin mix matrix $\mathbf{M}_{mix} = \begin{pmatrix} -p_m & p_0 & 0 \\ p_m & -2p_0 & p_p \\ 0 & p_0 & -p_p \end{pmatrix}$, and singlet pairing matrix $\mathbf{M}_{sp} = \begin{pmatrix} -p_m & 0 & p_p \\ 0 & 0 & 0 \\ p_m & 0 & -p_p \end{pmatrix}$. The evolution of ^{7}Li spin in ^{87}Rb bath spin can be described by the rate equation:

$$\frac{d\boldsymbol{P}}{dt} = (\Gamma_{ex}\mathbf{M}_{ex} + \Gamma_{mix}\mathbf{M}_{mix} + \Gamma_{sp}\mathbf{M}_{sp})\boldsymbol{P} \tag{5.11}$$

In comparing our measured data to a theoretical model, we take into account one more effect, which is the decay of the ^{7}Li gas atom number over the duration of the measurements. Our model takes into account by assuming an exponential decay in the total atom number. $\boldsymbol{N} = N_0\boldsymbol{P}e^{-t/\tau}$ represents dynamic population of ^{7}Li during the evolution.

$$\frac{d\boldsymbol{N}}{dt} = -\frac{\boldsymbol{N}}{\tau} + N_0 e^{-t/\tau}\frac{d\boldsymbol{P}}{dt} \tag{5.12}$$

The absence of spin-dependent loss is justified by monitoring ^{7}Li lifetime in the three different ^{87}Rb bath configuration. Although ^{7}Li spin evolves into different configurations with different atom populations in the three relevant Zeeman sublevels, the lifetime is similar, suggesting the spin-independence of the loss process.

5.3 Spin state initialization and detection

To prepare the initial spin state for both ^{7}Li and ^{87}Rb, we use the widely-adopted method, two-color optical pumping method, shown in Fig. 5.3 a. For the optical pumping light, we use σ_+/σ_- to drive the spin state to either $|+1\rangle$ or $|-1\rangle$. Due to the spontaneous emission, we need to depump those atoms which have been optically pumped into F = 2 manifold. Therefore, we add a second color for this purpose. For ^{87}Rb, this optical pumping process is done using ^{87}Rb D$_2$ line. For ^{7}Li, due to its unresolved D$_2$ line, we use its D_1 line instead.

This optical pumping process is performed on atoms that are within the optical trap. Our dipole trap is relative deep, around 840 μK for ^{87}Rb and 330 μK for ^{7}Li. The light for this trap is produced by a single frequency laser amplifier (ALS-IR-1064-50-A-SF) seeded by a home-made 1064 nm external cavity diode laser (ECDL). The dipole trap trapping potential leads to an inhomogeneous AC stark shift, combined with the possible off-resonant coupling of the target dark state to some nearby excited states, which, potentially, will affect the optical pumping efficiency. The criterion is to tune the optical pumping light roughly on resonance while decreasing the intensity. In experiment, we scan the optical pumping light frequency and monitor the rate of the generation of atoms in F = 2 manifold, shown in Fig. 5.3 b for ^{7}Li as an example. We park the light frequency to the value with the fastest generation rate, and then scan the light intensity while monitoring the optical pumping

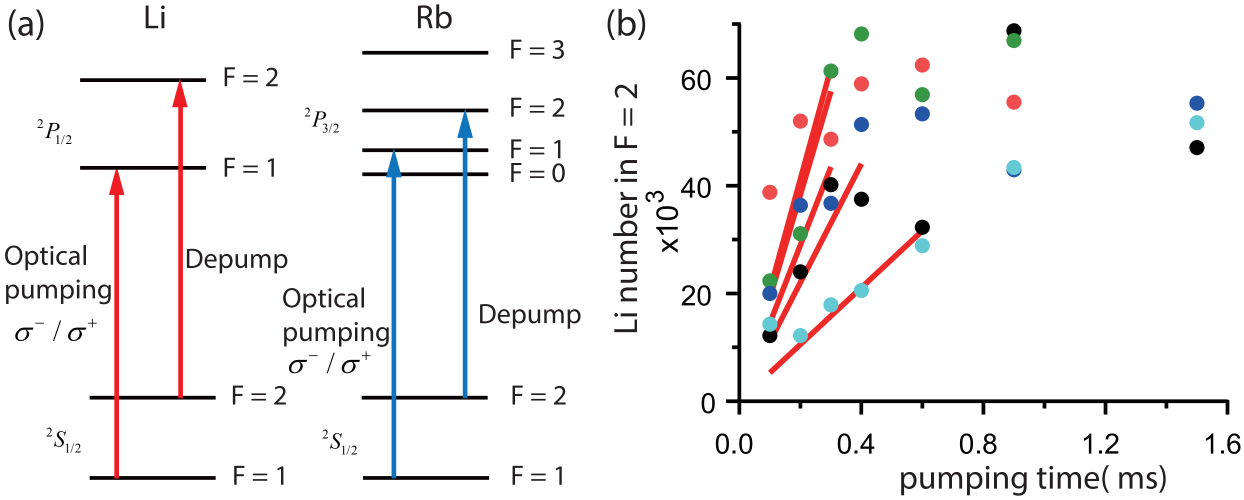

Figure 5.3: Optical pumping scheme. (a): two-color optical pumping scheme for ^{7}Li and ^{87}Rb. (b): rate of the generation of atoms in F = 2 manifold for ^{7}Li in optical dipole trap. Solid line is the linear fit for the rate. Different color represents different optical pumping light frequency. For this measurement, we control the optical power to be around 20 μW, with $I/I_{sat} << 1$. Here I_{sat} is the saturation intensity for ^{7}Li D_2 line.

efficiency. After this optimization, we achieve around 80% optical pumping efficiency to the target state for ^{87}Rb and nearly 100% for ^{7}Li.

To detect the spin state for ^{87}Rb, we use the state-sensitive microwave addressing method. This method is well documented in Ed's thesis [1]. In brief, in this method, we separately address the three different Zeeman sublevels in $f = 1$ manifold through applying a short on-resonant microwave pulse to excite atoms from just one of the Zeeman sublevels into $f = 2$ manifold. We then image those excited atoms through absorption imaging with light resonant with the $F = 2 \rightarrow F' = 3$ cycling transition. To calibrate the ^{87}Rb spin state, we use the unpolarized ^{87}Rb spin with equal population in three Zeeman sublevels as a standard to compare to. This unpolarized ^{87}Rb spin is produced by directly catching atoms from the molasses without optical pumping. We confirm this spin state is indeed unpolarized through the following steps. First, we confirm that the σ^- and σ^+ lights have the same pumping efficiency by monitoring $|0\rangle$ state population after the same short microwave excitation with and without optical pumping. The equal ratio of $|0\rangle$ population with σ^-/σ^+ light for optical pumping over without optical pumping demonstrates the similar pumping efficiency for the two target states. Second, we confirm the same amount of ^{87}Rb in $|-1\rangle$ and $|+1\rangle$ state in our unpolarized sample, by monitoring the ratio of the two state with its corresponding optical pumping over without optical pumping. Again, the similar ratio demonstrates our second point. Third, we confirm the same amount of $|0\rangle$ state population as that of in $|-1\rangle$ and $|+1\rangle$ state. This confirmation is done by measuring the ratio of the three Zeeman states with optical pumping over without optical pumping. Under the assumption that each Zeeman sublevel without optical pumping counts 1/3 of the total population, we sum up the

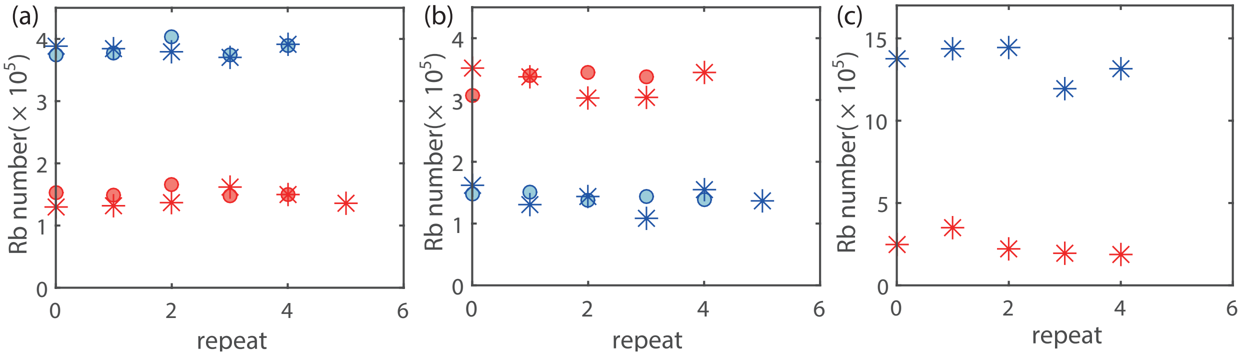

Figure 5.4: Spin detection scheme for ^{87}Rb . Red markers represent ^{87}Rb atom number in F = 2 after a short microwave pulse with optical pumping. Blue markers represent the same experimental result but without optical pumping, thus are for unpolarized sample. Circles represent the experimental settings with σ^+ light, with $|+1\rangle$ the target pumping state. Stars represent the settings with σ^- light, with $|-1\rangle$ the target pumping state. (a) Repeated $|0\rangle$ state population measurements in F = 2 after a short microwave pulse for samples with/without optical pumping. Here we confirm σ^+ has the same pumping efficiency as σ^- in our experiment. (b) Repeated target state population measurements with/without optical pumping. Here we confirm the same amount of ^{87}Rb in $|-1\rangle$ and $|+1\rangle$ state in our unpolarized sample. (c) Repeated $|+1\rangle$ state population measurements with/without optical pumping. Here the pumping target state is $|-1\rangle$. With (a), (b), (c), we confirm the sum of the measured percentages of the three sublevels is around 1 after optically pumping to $|-1\rangle$, and a pumping efficiency of around 80%.

measured percentages of the three sublevels and end up with a value around 1. With this calibration method, we are able to detect ^{87}Rb populations in the three Zeeman sublevels at 8% level.

After this confirmation, to calibrate ^{87}Rb spin state, we do two measurements. First we apply a short microwave pulse to excite the three Zeeman sublevels from F = 1 manifold and count the atom number of this ^{87}Rb spin state in the corresponding F = 2 manifold. Second we do a calibration measurement using the same microwave pulse on the unpolarized ^{87}Rb spin. Then we calculate the ratio between the two to get the percentage. Fig. 5.4 shows this procedure of ^{87}Rb spin detection.

To detect ^{7}Li spin, however, this state-sensitive microwave excitation method does not work for two reasons. First, $f = 2$ ^{7}Li atoms probably not stable, and also the unresolved hyperfine structure makes it harder to pump atoms in the $f = 2$ state to the stretched state without losing them en route to the $f = 1$ level. Second, we are unable to use standard Stern-Gerlach absorption imaging because we are working with a relative hot ^{7}Li gas around 36 μK such that they cannot be well separated spatially by the field gradient due to the fast ballistic atomic cloud's expansion from TOF.

Therefore, we developed a new spin-selective detection method as described below. We overlap our single beam dipole trap with a spherical quadrupole magnetic trap, with a total field $B(\boldsymbol{r}) = B'(\frac{x}{2}, \frac{y}{2}, -z)$. Taking advantage of the small hyperfine splitting in ^{7}Li ground state, a full Breit-Rabi expression for the magnetic field response needs to be taken into account, providing an anti-trapping potential for $m_F = 0$ sublevel at a moderate field gradient level. Here we consider three settings for the hybrid potential, shown in Fig. 5.5.

In the first setting, the magnetic field gradient is off. The trapping potential for each of the Zeeman sublevels is the same, generated solely by the state-independent ac Stark shift of the optical trapping light. An image of the gas released from this trap gives the total atom number N_{Total}, shown in Fig. 5.5 c.

In setting two, we consider adding a moderate-gradient spherical quadrupole trap, with $B' = 58$ G/cm, shown in Fig. 5.5 b. The gradient from this trap is sufficient to expel all atoms in the $m_F = +1$ strong-field seeking state. Atoms in the $m_F = 0$ state do not experience a linear Zeeman shift, but do experience a repulsive quadratic Zeeman shift from the magnetic trapping fields. However, at this setting, the effect of this quadratic Zeeman shift remains very weak within the volume of the dipole trap, so that $m_F = 0$ state atoms remain trapped, as do the $m_F = -1$ state atoms for which the spherical quadrupole fields provide extra confinement. Imaging atoms from this medium-gradient hybrid trap gives the sum of ^{7}Li number in $|-1\rangle$ and $|0\rangle$, with the expression $N(m_F = -1) + N(m_F = 0)$.

Finally, in setting three, we apply a very large (number) gradient field, with $B' = 270$ G/cm. In this case, the repulsive quadratic Zeeman shift is large and the $m_F = 0$ atoms are actively expelled from the hybrid trap, shown in Fig. 5.5 a.

To test this detection method, after initialization of ^{7}Li spin through optical pumping, we apply a RF pulse to rotate the spin. Then we use the above method to analyze ^{7}Li spin. The result is shown in Fig. 5.5 c. The measured result matches our expectation, confirming the effectiveness of our detection method. We also confirm the effectiveness of our method for ^{7}Li spin detection with the presence of ^{87}Rb. In this experiment, after optical pumping to $|+1\rangle$, we turn on a Landau-Zener sweep and then detect ^{7}Li spin configuration. This experiment is done with ^{7}Li alone or with unpolarized ^{87}Rb spin presence, see Fig. 5.5 d. The similar behavior in the two cases demonstrates that our detection method is effective with ^{87}Rb spin presence, thus can be used to detect the ^{7}Li spin dynamics in ^{87}Rb bath.

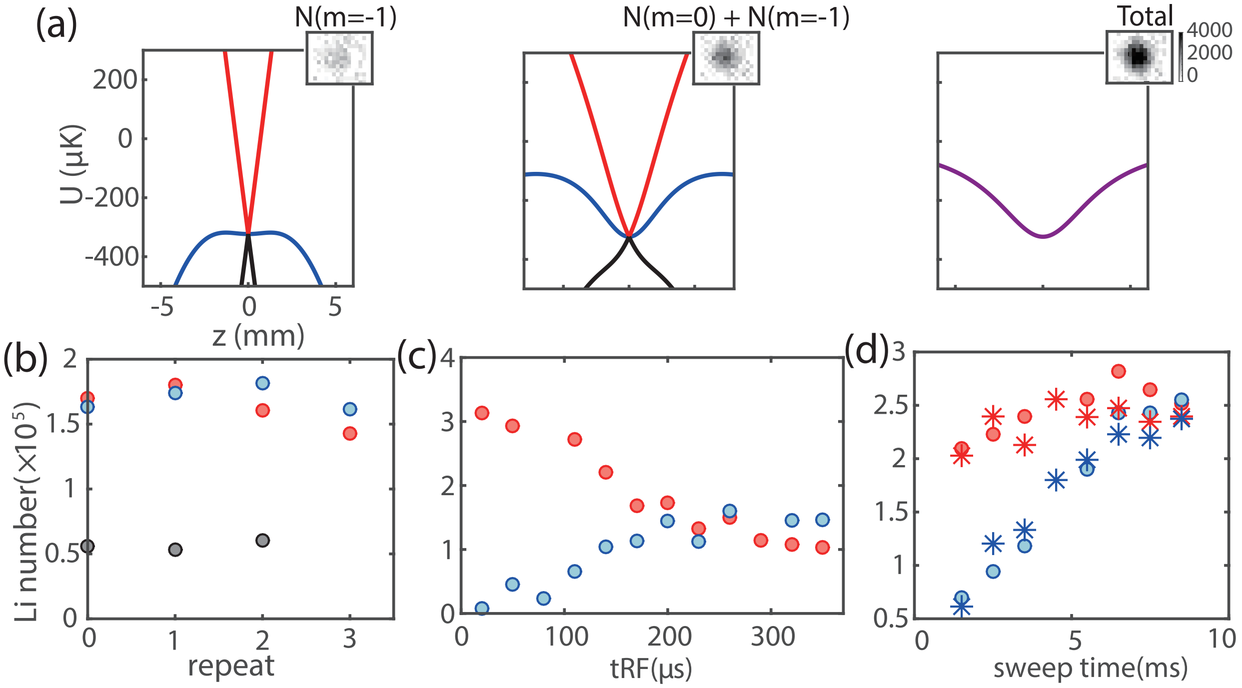

Figure 5.5: Spin detection scheme for ^{7}Li . (a): Hybrid optical trapping potential with a field gradient B'_z for the three Zeeman sublevels along the propagation direction of the dipole trap. From left to right, it displays the result for $B'_z = 270$ G/cm, 58 G/cm, 0 G/cm. Solid red line, blue line and black line represent detection potential for $|-1\rangle$, $|0\rangle$ and $|+1\rangle$ states, respectively. Inset: sample detection images for ^{7}Li . (b): Repeated detection for ^{7}Li spin. Blue: total ^{7}Li number. Red: ^{7}Li number in $|-1\rangle$ with optical pumping using our detection method. Black: ^{7}Li number in $|-1\rangle$ for an unpolarized sample. (c): ^{7}Li spin detection after RF excitation. Red: ^{7}Li number in $|-1\rangle$ as a function of RF excitation length. Blue: ^{7}Li number in $|0\rangle$ as a function of RF excitation length. (d): ^{7}Li spin detection with ^{87}Rb presence. Red: $N(m_F = -1) + N(m_F = 0)$ vs Landau Zener sweep time. Blue: $N(m_F = -1)$ vs Landau Zener sweep time. Circles mark ^{7}Li alone results. Stars mark ^{7}Li results with unpolarized ^{87}Rb presence.

5.4 Experimental result

With the experimental scheme and the detection method mentioned above, we show our experimental results, in Fig. 5.6. The key finding is that the ^{7}Li spin relaxes towards ^{87}Rb spin configuration, in a time scale of seconds. This phenomenon could be explained by the spin-dependent interaction and modeled by the rate equation approach introduced in previous sections. This gives us the convenience to extract the values of the three Γs from our experimental data.

All three measurement settings provide information that constrains the values of the three rates. However, the constraints on certain rates are stronger in certain data sets. Specifically, in setting 1, the fitting will be most strongly constraining for Γ_{ex}, and only marginally constraining for the other rates. Given that our overall goal is to constrain a set of rates that give a universal description of all the data we have gathered, we choose to apply a fit to all measured data simultaneously, allowing the fitting procedure to account automatically to the implication of each data point on the rates affecting the system.

Using Eq. 5.15, with Γ_{ex}, Γ_{mix}, Γ_{sp}, total ^{7}Li number N_{tot} and ^{7}Li life time τ as free fitting parameters, we use least squares method simultaneously fitting the nine data sets shown in Fig. 5.6 to our model. The result of this fitting is displayed in Table 1.

We first constrain the fit with a physical boundary so that all three Γs are positive. The corresponding result is shown in the first row of Table. 5.1. This fitting favors a vanishing singlet-pairing process, which can be seen clearly in Fig. 5.6 e. The creation of atoms in $|0\rangle$ state before $|+1\rangle$ state is a signature of an appreciable mix process. Otherwise, only with singlet pairing, the red line ($N(m_F = -1)$) and the blue line ($N(m_F = -1) + N(m_F = 0)$) should collapse into a single decay line, shown in the inset of Fig. 5.6 e.

Theory predicts three spin-dependent cross sections for the three elementary collision processes, with a weak energy dependence at the collisional energy of our experiments, see Fig. 5.2. This theoretical prediction is shown in the third row of Table. 5.1, with the exchange and mix processes of roughly the same magnitude accompanied by a tiny singlet-pairing process.

To have a tighter constrain in the fitting procedure, we set Γ_{sp} to be the theoretically predicted value and only fit for the other two, Γ_{ex} and Γ_{mix}. By doing so, we are able to shrink the uncertainty in the measured Γ_{ex} and Γ_{mix}, while keeping the fitting center value unchanged, shown in the second row of Table. 5.1.

However, although this non-negative choice for the relaxation rates is physically making sense, we were concerned that setting a hard constraint on the rates (that each must not be smaller than zero) would skew the error estimation by the fitting routine. We thus set all three Γs to be free parameters. This fit ends up with a negative Γ_{sp}. This unphysical result is due to the ^{7}Li atom number fluctuation in our experiment, especially at the early stage of relaxation. For instance, in Fig. 5.6 e, this negative Γ_{sp} induces an initial rising in the $N(m_F = -1) + N(m_F = 0)$ above the total atom number, matching the atom fluctuation in the measurement at early stage. To compensate for this negative Γ_{sp}'s effect on later stage of evolution, this fit increases the value of the Γ_{ex} and Γ_{mix} by about a factor of two compared

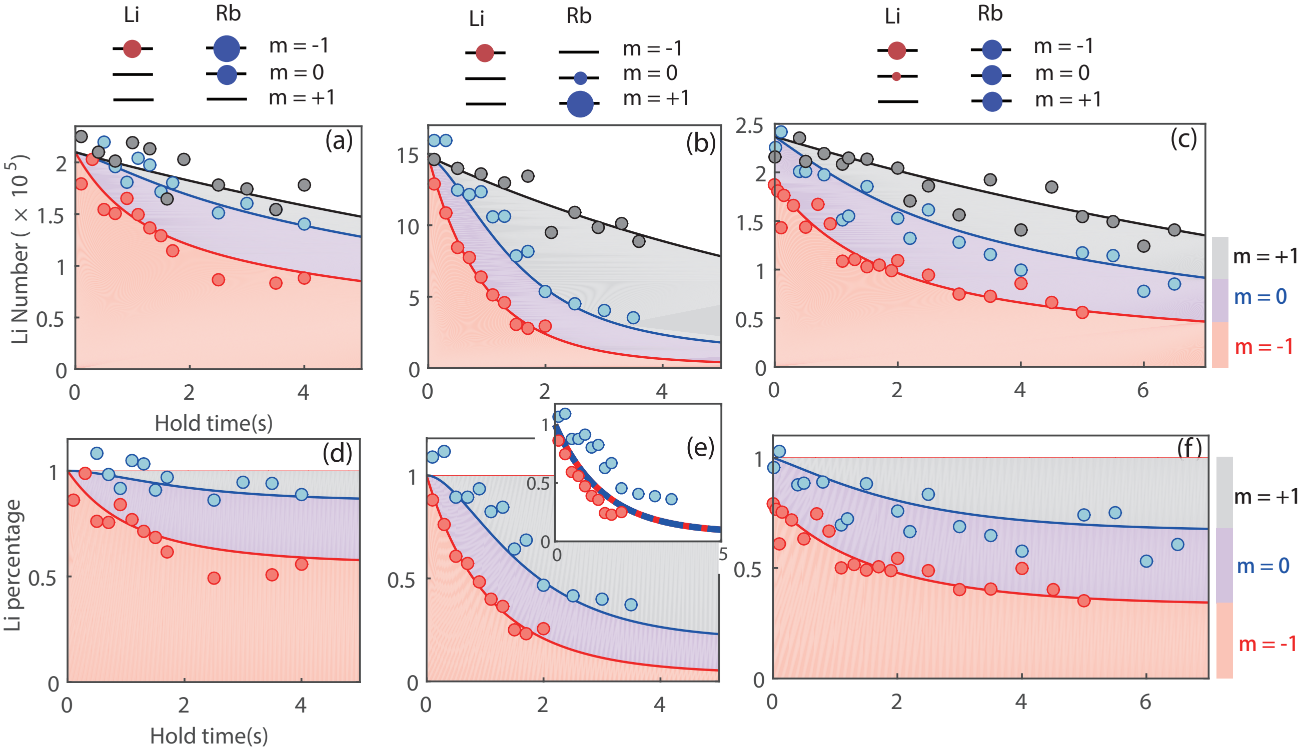

Figure 5.6: ^{7}Li spin dynamics in ^{87}Rb bath. From left to right, it shows ^{7}Li spin dynamics in the three ^{87}Rb bath spin configurations mentioned in main text. The first row shows the two spin after initialization. The second row shows ^{7}Li number evolution in the three Zeeman sublevels in its ^{87}Rb bath configuration. The third row shows the corresponding ^{7}Li percentage evolution in three Zeeman sublevels. The shaded areas in red, purple and gray correspond to atoms in $|-1\rangle$, $|0\rangle$ and $|+1\rangle$ states.

to the case with non-negative relaxation rates constrain. However, the uncertainty level in the two cases for Γ_{ex} and Γ_{mix} are similar, around 35%. Here we conclude our experiment is not in favor of a large and positive singlet pairing process.

A robust output of our fitting is the ratio of different rates, which manifests the relative magnitude of the different spin-dependent processes, and is independent of the optical dipole trap details. In the fifth column of Table. 5.1, we show our results for the ratio between Γ_{ex} and Γ_{mix}. Our measurement of this ratio is in good agreement with theory.

Now we extract the spin-dependent cross section from the measured relaxation rate using Eq. 5.10. The highly mass-imbalanced ^{7}Li-^{87}Rb system has an inefficient energy-transfer. Together with possible optical evaporation for ^{7}Li, the temperatures for both species can be taken as constant values, which is also confirmed experimentally. Therefore, we are allowed to directly use measured T_{Li} and T_{Rb} to estimate $n_{overlap}$ and v_{rel}. With $\sigma = 4\pi a^2$, we are able to extract the corresponding absolute value of spin-dependent s wave scattering length

	Γ_{ex}	Γ_{mix}	Γ_{sp}	σ_{ex}/σ_{mix}	$\lvert a_{ex}\rvert(a_B)$	$\lvert a_{mix}\rvert(a_B)$	$\lvert a_{sp}\rvert(a_B)$
Experiment	1.31 ± 0.36	0.94 ± 0.35	2.72×10^{-7}	1.39 ± 0.64	8.23 ± 1.17	6.99 ± 1.30	0.004
Fix Γ_{sp}	1.30 ± 0.26	0.93 ± 0.18	0.009	1.40 ± 0.39	8.20 ± 0.86	6.96 ± 0.71	0.67
Theory	−−	−−	−−	1.20	7.8	7.15	0.67

Table 5.1: Elementary collision processes. First row: Experimentally fitted values with positive constrain for the three Γs. Second row: Experimentally fitted values with Γ_{ex}, Γ_{mix} as free fitting parameters, Γ_{sp} fixed to theoretical prediction. Third row: theoretical prediction. Errorbars in first and second row are statistical including errors from the least squares fit, trap frequency calibration, temperature measurements and ^{87}Rb atom number counting.

$|a|$.

Here we explain our way to estimate the overlap density of the two species. With a large η around 10, the trapping potential for ^{7}Li and ^{87}Rb formed by a Gaussian beam is well approximated by a harmonic potential. Here $U_{depth} = \eta k_B T$ with U_{depth} the trap depth, k_B Boltzmann constant and T temperature of the gas. Both ^{7}Li and ^{87}Rb obey Maxwell-Boltzmann distribution. Now we label ^{7}Li with 1 and ^{87}Rb 2. Define $\alpha_i = \frac{m_1\omega_{i1}^2}{2k_BT_1}$, $\beta_i = \frac{m_2\omega_{i2}^2}{2k_BT_2}$. Here i = x, y, z, we have:

$$\begin{aligned} n_1 &= N_1\sqrt{\frac{\alpha_x\alpha_y\alpha_z}{\pi^3}}e^{-\alpha_x x^2-\alpha_y y^2-\alpha_z z^2} \\ n_2 &= N_2\sqrt{\frac{\beta_x\beta_y\beta_z}{\pi^3}}e^{-\beta_x x^2-\beta_y y^2-\beta_z z^2} \end{aligned} \tag{5.13}$$

Here N represents atom number, m represents atomic mass and n represents density distribution.

$$\begin{aligned} n_{overlap} &= \frac{1}{N_1}\int_{-\infty}^{+\infty} n_1 n_2\, dxdydz \\ &= N_2\sqrt{\frac{\alpha_x\alpha_y\alpha_z}{\pi^3}}\sqrt{\frac{\beta_x\beta_y\beta_z}{\pi^3}}\sqrt{\frac{\pi}{\alpha_x+\beta_x}}\sqrt{\frac{\pi}{\alpha_y+\beta_y}}\sqrt{\frac{\pi}{\alpha_z+\beta_z}} \end{aligned} \tag{5.14}$$

With this expression, measured trap frequency, temperature and ^{87}Rb number, we calculate the $n_{overlap}$ to be around 1.5×10^{12} cm^{-3}, $v_{rel} = \sqrt{\frac{8k_B}{\pi}(\frac{T_{Rb}}{m_{Rb}} + \frac{T_{Li}}{m_{Li}})}$ to be around 0.36 m/s. The gravity's effect can be ignored here thanks to our high radial trap frequency, around 2.6 kHz, leading to a trap minimum position shift of less than 0.04 μm, which is tiny compared to our beam waist, around 34 μm.

Finally, with our measured Γs, we report the experimentally determined $|a|$, shown in the last three column in Table. 5.1. Fig. 5.7 shows our calibration of trap frequency for both radial and axial, and ^{87}Rb number calibration. Here we report the measured physical quantity values and the corresponding error estimation propagated by Eq. 5.14 in Table. 5.2.

	$T_{Rb}(\mu K)$	$T_{Li}(\mu K)$	N_{Rb}	$f_{radial}(HZ)$	$f_{axial}(HZ)$
Value	87(2)	36(2)	$2.0(1) \times 10^6$	2611(39)	15.63(15)
Error u_a/a	0.006	0.009	0.02	0.015	0.005

Table 5.2: Relative error in spin-dependent scattering length contributed by the relevant experimentally-determined physical quantity. The first row records the measurement results with 1-σ error bar. The second row records the relative error propagated into the scattering length.

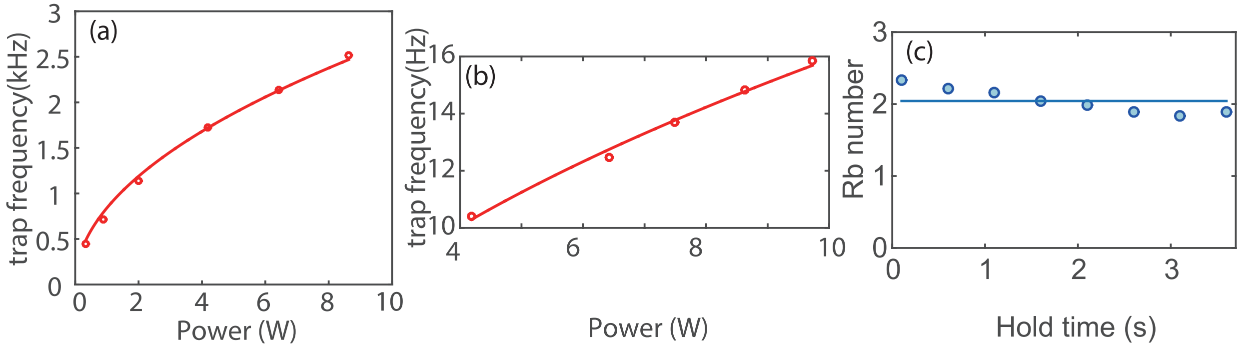

Figure 5.7: Trap frequency and ^{87}Rb number calibration. (a) Radial trap frequency measurements. This is done by parametric heating method at a series of optical dipole trap laser power. (b) Axial trap frequency measurement. This is done by giving the cloud a kick and then monitoring the spatial center of mass oscillation of the atomic cloud. Again, this measurement is done at a series of trap depth. Solid line is a fit to the motion of harmonic oscillator. (c) Calibration of ^{87}Rb total atom number in dipole trap as a function of hold time in trap.

We conclude the main contribution to the uncertainty in the spin-dependent scattering length $|a|$ is from our least squares fit of the nine data sets to our theoretical model mentioned in Sec. 5.2. Specifically, our three experiment with different ^{87}Rb spin bath configurations are done in three different day, thus with different total ^{87}Rb number. As they are done in the same dipole trap, we scale up the relaxation rate by the corresponding ^{87}Rb number.

5.5 Long time dynamics: Stationary ^{87}Rb spin bath

Our experiment can be interpreted from the spintronics point of view. ^{7}Li spin is at first initialized in a non-equilibrium distribution through optical pumping. Then it is injected into a stationary ^{87}Rb spin bath. After some time of evolution, our experiment shows that ^{7}Li spin relaxes towards ^{87}Rb spin distribution, or ^{87}Rb induces local spin switching of ^{7}Li .

In this section, we focus on the steady state of ^{7}Li spin after long enough evolution, assuming the ^{87}Rb spin bath is stationary. This is approximately correct for our system with the ^{87}Rb atom number ten times larger than the ^{7}Li number. For a spin-1 object without transverse coherence, the spin distribution is described fully by specifying just two moments: the magnetization, $M_z = p_{+1} - p_{-1}$, and the quadrupole moment, $N_{zz} = \frac{1}{3}(p_{+1} - 2p_0 + p_{-1})$. With the constrain that all ps are positive and the sum of them equals to unity, we have the constrain on N_{zz}:

$$\begin{aligned} N_{zz} &\leq \frac{1}{3} \\ N_{zz} &\geq M_z - \frac{2}{3} \\ N_{zz} &\geq -M_z - \frac{2}{3} \end{aligned} \tag{5.15}$$

These three inequalities determine the possible range for N_{zz}, shown by the triangle area in Fig. 5.8 a and b.

We hence study the relation between the steady state M_z, N_{zz} of ^{7}Li and those of ^{87}Rb . It turns out that they are not exactly equal to each other, with the final steady state of ^{7}Li M_z and ^{7}Li N_{zz} depending on both ^{87}Rb M_z and ^{87}Rb N_{zz}, and the relative relaxation rates for the three elementary collision processes. This deviation is mainly from the mix process where the enhancement in ^{87}Rb $|0\rangle$ state density helps the depletion of ^{7}Li $|0\rangle$ state density, leading to a different steady state requirement compared to the other two spin processes: $p_0 N_0 = p_m N_p = p_p N_m$, which can cause ^{7}Li spin steady state to be different from its ^{87}Rb spin bath.

In Fig. 5.8, we show 2D contour plots for ^{7}Li spin steady state M_z (a) and N_{zz} (b) against ^{87}Rb M_z and N_{zz}, predicted by our relaxation model with experimentally determined relaxation rates. Scattered markers are the four experimental points after a long time evolution (≥ 2.5 s), with errorbars representing the uncertainties in calibrations of ^{87}Rb bath M_z and N_{zz}, and the filled color representing the values of the corresponding ^{7}Li M_z (a) and N_{zz} (b).

These contour plots show that the steady state ^{7}Li M_z only slightly deviates from ^{87}Rb bath M_z, also confirmed by our experimental measurements of ^{7}Li spin state after long time evolution, shown in Fig. 5.8.

However, the steady state ^{7}Li N_{zz} can deviate from ^{87}Rb values significantly. For instance, if we follow the white dashed line in Fig. 5.8 b, constraining to the subspace with zero ^{87}Rb M_z, this steady state deviation of ^{7}Li from ^{87}Rb can be seen clearly. We thus plot ^{7}Li N_{zz} against ^{87}Rb N_{zz} along this white dashed line, shown in Fig. 5.8 d, with the solid black line representing the equal-value line, and the dashed green line representing the our model predicted ^{7}Li steady state. The green star marks our experimental measurement of ^{7}Li evolving in an unpolarized ^{87}Rb spin bath. The stark difference between the black and dashed green line manifests this significant deviation of ^{7}Li spin state from its ^{87}Rb bath.

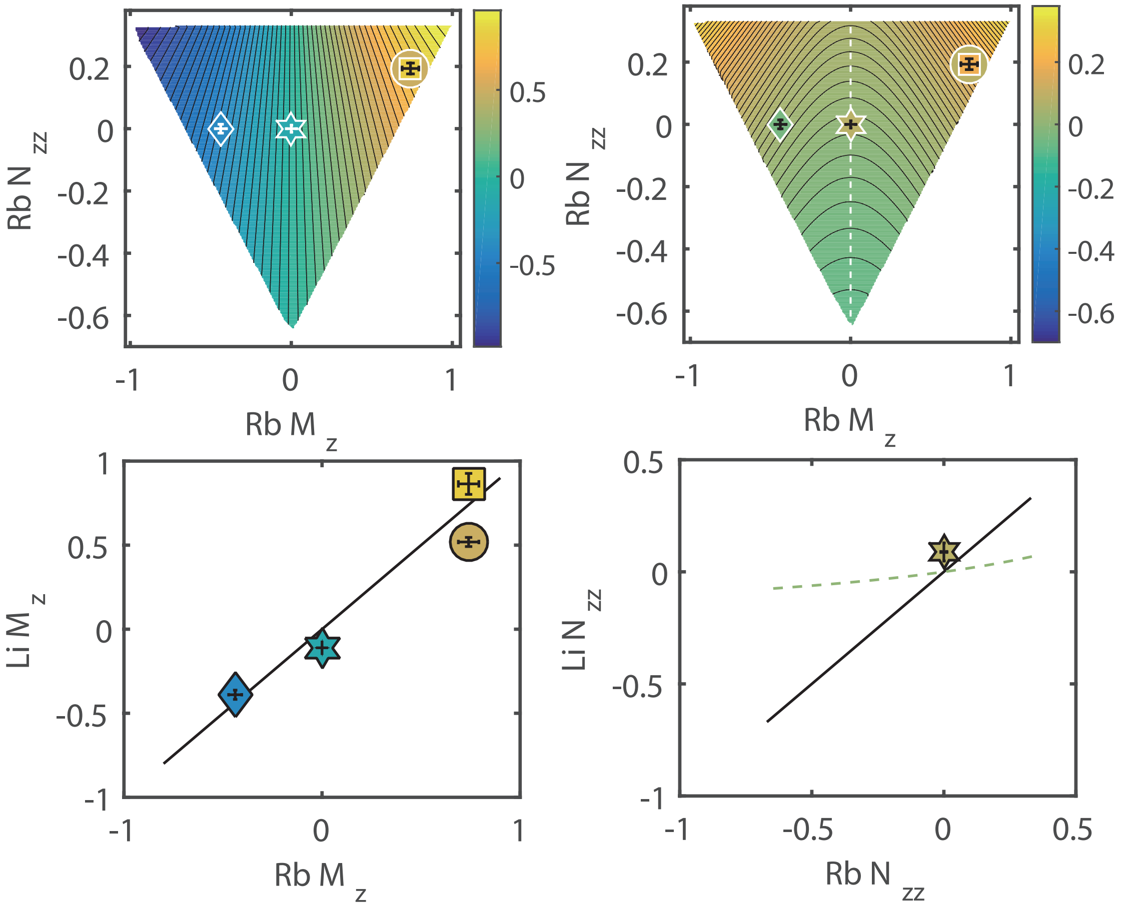

Figure 5.8: Long time evolution. Diamond, six-pointed star, circle, square makers represent experimental measurements after long time evolution, averaged over three to four measurements. Diamond, six-pointed star, circle markers represent ^{7}Li spin initialized to $|-1\rangle$ state. Square marker represents ^{7}Li spin starting from $|+1\rangle$ state. 2D contour plots of ^{7}Li M_z (a) and N_{zz} (b) against ^{87}Rb M_z and N_{zz}. Scattered markers are corresponding experimental measurements after a long time evolution, with errorbars representing the uncertainties in ^{87}Rb M_z and N_{zz}, and the filled color representing the values of the corresponding ^{7}Li M_z (a) and N_{zz} (b). (c) 1D plot of ^{7}Li M_z against ^{87}Rb M_z after a long time evolution. Solid black line guides the eye to the equal-value line. (d) 1D plot of ^{7}Li N_{zz} against ^{87}Rb N_{zz}, constraining to the subspace with zero ^{87}Rb M_z, corresponding to the white-dashed trajectory in (b). Solid black line guides the eye to the equal-value line. Green dashed line is the theoretical model predicted ^{7}Li N_{zz} with the experimentally determined relaxation rates.

5.6 Long time dynamics: Coupled evolution

In the previous section, we consider ^{7}Li spin steady state with an unchanging ^{87}Rb spin bath. Actually, the spin relaxation processes would also change ^{87}Rb spin configuration. The evolution of the system is described by a coupled equation:

$$\begin{aligned}
\frac{d\boldsymbol{N}_{Li}}{dt} &= -\frac{\boldsymbol{N}_{Li}}{\tau_{Li}} + (\Gamma_{ex}^{Li}\mathbf{M}_{ex}^{Rb} + \Gamma_{mix}^{Li}\mathbf{M}_{mix}^{Rb} + \Gamma_{sp}^{Li}\mathbf{M}_{sp}^{Rb})\boldsymbol{N}_{Li} \\
\frac{d\boldsymbol{N}_{Rb}}{dt} &= -\frac{\boldsymbol{N}_{Rb}}{\tau_{Rb}} + (\Gamma_{ex}^{Rb}\mathbf{M}_{ex}^{Li} + \Gamma_{mix}^{Rb}\mathbf{M}_{mix}^{Li} + \Gamma_{sp}^{Rb}\mathbf{M}_{sp}^{Li})\boldsymbol{N}_{Rb}
\end{aligned} \tag{5.16}$$

Here $\boldsymbol{N}_{Li/Rb}$ denotes the dynamical spin population of ^{7}Li and ^{87}Rb, $\tau_{Li/Rb}$ denotes the lifetime of ^{7}Li and ^{87}Rb, $\Gamma^{Li/Rb}$ denotes the relaxation rate per ^{7}Li or per ^{87}Rb, $\boldsymbol{M}^{Li/Rb}$ denotes spin matrix for ^{7}Li and ^{87}Rb. In our experiment, we have ten times larger ^{87}Rb in atom number compared to ^{7}Li, thus the coupled equation should predict similar evolution for ^{7}Li spin as that of a constant ^{87}Rb spin bath. This is indeed the case, as shown in Fig. 5.9, with the dashed lines represent the prediction from the coupled equation, and the solid lines the model fitting results with stationary ^{87}Rb spin bath, indicating a slight deviation, less than 10%.

Now we examine this coupled system from thermal dynamical point of view. The final equilibrium state should satisfy equal chemical potential for the incoming and outcoming states for the three spin dependent processes. For Boltzmann gas trapped in a harmonic trap, we have

$$e^{\frac{\mu}{k_B T}} = \frac{N}{Z} \tag{5.17}$$

Here μ is chemical potential, k_B is Boltzmann constant, T is gas temperature, N is atom number, Z is partition function for a harmonically-trapped Boltzmann gas. Therefore, we have $\mu \propto$ InN. For exchange process,

$$\begin{aligned}
\mu_{+1}^{Li} + \mu_0^{Rb} = \mu_0^{Li} + \mu_{+1}^{Rb} &\implies \frac{N_{+1}^{Li}}{N_0^{Li}} = \frac{N_{+1}^{Rb}}{N_0^{Rb}} \\
\mu_{-1}^{Li} + \mu_0^{Rb} = \mu_0^{Li} + \mu_{-1}^{Rb} &\implies \frac{N_{-1}^{Li}}{N_0^{Li}} = \frac{N_{-1}^{Rb}}{N_0^{Rb}}
\end{aligned} \tag{5.18}$$

Similarly, for mix process,

$$\begin{aligned}
\mu_{+1}^{Li} + \mu_{-1}^{Rb} = \mu_0^{Li} + \mu_0^{Rb} &\implies N_{+1}^{Li}N_{-1}^{Rb} = N_0^{Li}N_0^{Rb} \\
\mu_{-1}^{Li} + \mu_{+1}^{Rb} = \mu_0^{Li} + \mu_0^{Rb} &\implies N_{-1}^{Li}N_{+1}^{Rb} = N_0^{Li}N_0^{Rb}
\end{aligned} \tag{5.19}$$

For singlet-pairing process,

$$\mu_{+1}^{Li} + \mu_{-1}^{Rb} = \mu_{-1}^{Li} + \mu_{+1}^{Rb} \implies \frac{N_{+1}^{Li}}{N_{-1}^{Li}} = \frac{N_{+1}^{Rb}}{N_{-1}^{Rb}} \tag{5.20}$$

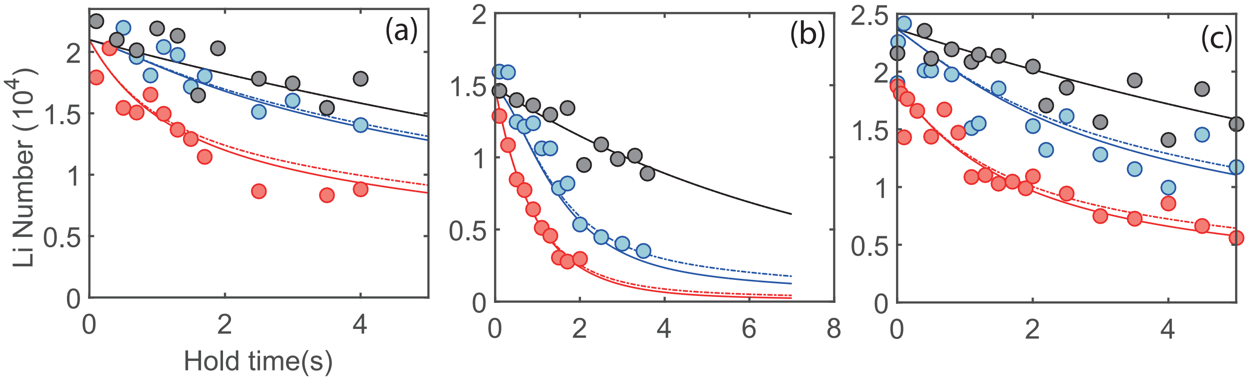

Figure 5.9: ^{7}Li - ^{87}Rb coupled evolution. Solid lines are model fitting results with constant ^{87}Rb spin bath. Dashed lines are predictions from coupled equation. 5.16. (a), (b), (c) corresponds to the three ^{87}Rb bath spin configurations mentioned in main text.

Combined Eq. 5.18, 5.20, we have the spin population percentage of ^{7}Li equal to that of ^{87}Rb . Defining this population percentage by (p_{+1}, p_0, p_{-1}), in addition, we have $p_0^2 = p_{+1}p_{-1}$ from the mix process Eq. 5.19. With the fact that all spin-dependent processes conserve the magnetization, we have

$$N_{Li}(p_{+1}^{Li^0} - p_{-1}^{Li^0}) + N_{Rb}(p_{+1}^{Rb^0} - p_{-1}^{Rb^0}) = (N_{Li} + N_{Rb})(p_{+1} - p_{-1}) \tag{5.21}$$

Here $N_{Li/Rb}$ is atom number for ^{7}Li or ^{87}Rb , p^0 denotes the spin population percentage in the three Zeeman sublevels for the initial state. With the fact that the sum of all ps equals to unity, we thus are able to predict the equilibrium spin population given an arbitrary initial state.

At last, we discuss an interesting situation when ^{7}Li spin evolves in a ^{87}Rb spin bath initialized with an enhancement in $|0\rangle$ state density. Because ^{87}Rb atom number is ten times larger than ^{7}Li atom number, ^{7}Li spin dynamics is ten times faster than ^{87}Rb . This system thus rapidly evolves to a "metastable" state where ^{7}Li N_{zz} can deviate significantly from the quasi-stationary ^{87}Rb spin bath, and then slowly evolves towards the final equilibrium state where both species stay in the same spin states, with the same M_z and N_{zz}.

Fig. 5.10 shows a numerical simulation manifesting this situation. In the simulation, we start with spin polarized ^{7}Li in $|-1\rangle$ state. ^{87}Rb spin is initialized with $(p_{+1}, p_0, p_{-1}) = (0.05, 0.9, 0.05)$. ^{87}Rb atom number is around ten times larger than ^{7}Li atom number. In Fig. 5.10 a and b, we plot the evolution of the Zeeman sub-level population of ^{7}Li (dashed line) and ^{87}Rb (solid line) under Eq. 5.16. In Fig. 5.10 c and d, we plot the evolution of N_{zz} of ^{7}Li (dashed line) and ^{87}Rb (solid line) under Eq. 5.16. Specifically, Fig. 5.10 a and c are constrained to short time evolution, where ^{7}Li quickly evolves to a stationary state, with ^{7}Li N_{zz} deviating from the N_{zz} of the quasi-stationary ^{87}Rb spin bath. Fig. 5.10 b and d focus on the long time evolution of the system, where the ^{87}Rb spin gradually evolves towards the ^{7}Li spin until they arrive at the same spin state. The time scale difference in spin dynamics

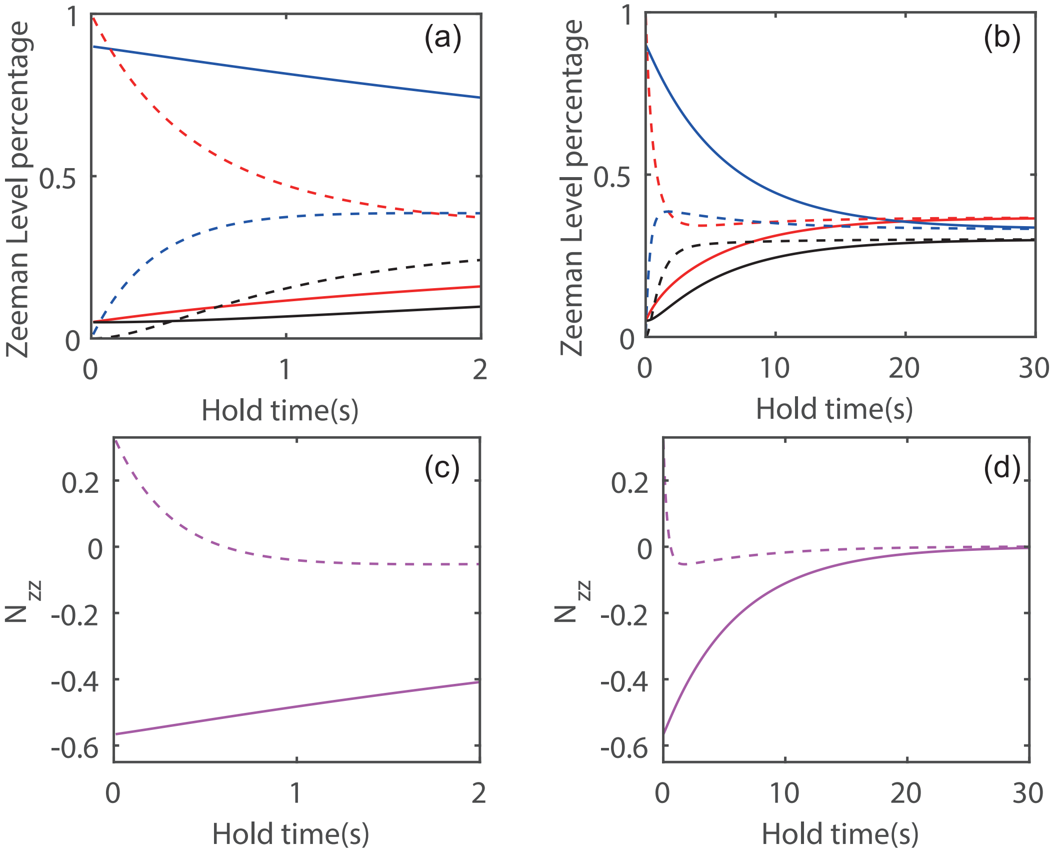

Figure 5.10: Simulated ^{7}Li evolution in a ^{87}Rb spin bath with an enhancement in $|0\rangle$ state population. Here ^{7}Li is initialized in $|-1\rangle$ state and ^{87}Rb spin is initialized with $(p_{+1}, p_0, p_{-1}) = (0.05, 0.9, 0.05)$. ^{87}Rb total atom number is about ten times larger than that of ^{7}Li. Solid lines are for ^{87}Rb evolution. Dashed lines represent ^{7}Li evolution. (a) Short time evolution of Zeeman sublevel population. Red, blue and black lines represent population evolution in $|-1\rangle$, $|0\rangle$ and $|+1\rangle$ state correspondingly. (b) Long time evolution of Zeeman sublevel population. The color scheme here is the same as in (a). (c) Short time evolution of N_{zz}. (d) Long time evolution of N_{zz}.

between ^{7}Li and ^{87}Rb is from the density imbalance, with the spin-dependent collision rate per ^{7}Li ten times larger than the collision rate per ^{87}Rb.

To observe this time scale separation in the spin dynamics between ^{7}Li and ^{87}Rb requires a preparation of ^{87}Rb spin states with an enhancement of $|0\rangle$ state density. For technical reasons, we leave it for future study.

5.7 Coherence

In Ref. [29], coherent spin oscillation between ^{87}Rb and ^{23}Na is observed[1]. This oscillation is induced by the heteronuclear spin exchange interaction and happens between $|0,-1\rangle$ and $|-1,0\rangle$. Here $|m_1,m_2\rangle$ represents magnetic sublevels of ^{87}Rb and ^{23}Na. By tuning the total Zeeman energy so that both states are on resonance, the oscillation induced by the small, HZ-level mean-field interaction is able to be observed and studied. This total Zeeman energy tunability is mainly due to the difference in the nuclear g-factors. For certain state combinations, it is possible to find a resonance at some non-zero magnetic field.

Compared to ^{23}Na-^{87}Rb system, ^{7}Li-^{87}Rb has a large spin-dependent mean field interaction, around 9 times larger. Therefore, similar oscillation should be observed at a relatively lower overlap density. Fig. 5.11 shows the total Zeeman energy difference between these two states. Solid blue line represents $\Delta E(B) = E^{|1_{Li},0_{Rb}\rangle}(B) - E^{|1_{Li},0_{Rb}\rangle}(B)$, corresponding to the exchange process. Solid orange line represents $\Delta E(B) = E^{|1_{Li},-1_{Rb}\rangle}(B) - E^{|0_{Li},0_{Rb}\rangle}(B)$, corresponding to the mix process. Dashed black line guides the eye to resonance position. Therefore, for both physical process, there exists a resonance at a non-zero magnetic field. As we can see from Fig. 5.11, the detuning from resonances is on the order of 10s of HZ and the two resonances are relatively near each other. These features can add complexity when one tries to selectively observe one resonance's effect with a relatively large mean-field interaction strength.

The previous sections describe our explorations of ^{7}Li spin dynamics in a ^{87}Rb spin bath, which focuses on the long time relaxation of the spin system. The spin-dependent mean-field interaction is proportional to the scattering length Δa_F, and as mentioned before, is induced by the forward scattering. On the other hand, the spin relaxation rate is proportional to cross section, thus $(\Delta a_F)^2$. This discrepancy leads to a time scale difference between the coherent process and the incoherent relaxation process. Specifically, the coherent process is around 10 times faster than the relaxation process. To observe the coherence effect, a sufficient long coherence time, longer than the mean-field interaction time scale, is required. In our experiment, after enhancing the overlap density by adding another laser beam to form a cross dipole trap, the fastest time scale for coherent dynamics we are able to achieve is on the order of 10 ms. However, a Ramsey experiment shows a quick decoherence on the order of 1 ms, which is a lot shorter than the required time scale. We attribute this quick decoherence to the interplay between residual field gradient/noise and a spatially-extended hot atomic cloud. In our best experimental settings, we are able to control field gradient to the level of 2 mG/cm. With a 2 mm long cloud, this leads to an around 0.3 kHZ energy difference across the cloud, roughly matching our measured decoherence time scale. One can improve the current situation from two aspects. First, a tighter focused dipole trap is favored because a shorter Rayleigh range can limit the atomic cloud spatial extension, thus enhance the coherence time. Second, evaporating the dipole trap down to work with colder mixtures is highly recommended. This will help enhance the overlap density and, at

---

[1] Similar coherent oscillation has been observed in Li-Na system recently[86].

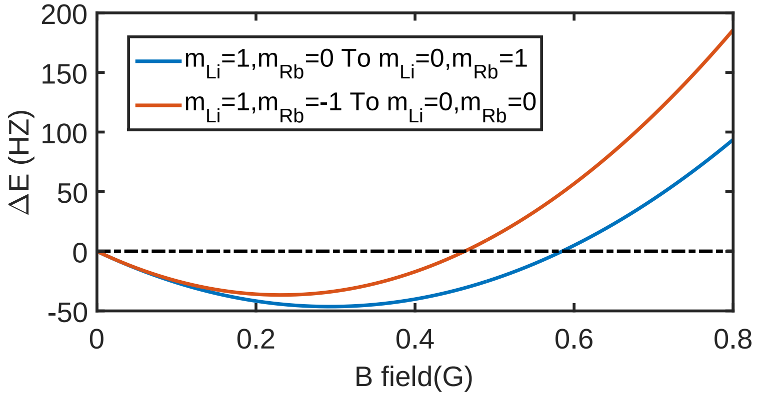

Figure 5.11: Total Zeeman energy difference for spin exchange and mix processes. Solid blue line represents $\Delta E(B) = E^{|1_{Li},0_{Rb}\rangle}(B) - E^{|1_{Li},0_{Rb}\rangle}(B)$, corresponding to the exchange process. Solid orange line represents $\Delta E(B) = E^{|1_{Li},-1_{Rb}\rangle}(B) - E^{|0_{Li},0_{Rb}\rangle}(B)$, corresponding to the mix process. Dashed black line guides the eye to resonance position.

the same time, minimize the three-body loss for ^{87}Rb, which is fairly severe at our current temperature and total atom number in the cross dipole trap. As the trap is ramped down, gravity will ultimately play a role to cut the cloud spatial extension, which, again, will help lengthen the coherence time. At this point, we leave this interesting topic for future study.

Chapter 6

Future

In this chapter, I will discuss some research prospects extended from my PhD research projects. The first prospect is on the behavior of physical system far from thermal equilibrium extended from the magnon condensation work. The second prospect is on atomtronics with heteronuclear spin-dependent interaction.

6.1 Non-equilibrium physics with ultracold atoms

While the thermal dynamics of equilibrium system has been thoroughly studied and well understood, the behavior of a manybody system far away from thermal dynamical equilibrium remains a hard problem nowadays. The evolution of a non-equilibrium system can depend on the microscopic details of the interaction, as well as the initial states, thus varies system from system, hard to predict but less interesting. One way to help the system lose the memory of initial states and microscopic details is through universality near critical point. Non-equilibrium phenomena such as cascades in turbulent flows [87], defect formation across phase transition have been studied both theoretically and experimentally [36, 41–48]. However, the theoretical and experimental characterization of subsequent time evolution of a system far from equilibrium are still lacked. While the behavior of a system near phase transition is governed by the thermal dynamical fixed point (critical point), recent studies show important new universality classes discovered in isolated relativistic systems far from equilibrium [88, 89]. This universality is based on the existence of nonthermal fixed point, and also generalized into non-relativistic systems such as the non-relativistic Bose gas [51]. In this system, Bose condensation occurs out of equilibrium as a consequence of particle transport towards lower momenta with energy transport towards higher momenta. This transport in systems out of equilibrium is described by a self-similar evolution, where the distribution function obeys for isotropic systems:

$$f(t, \boldsymbol{p}) = t^{\alpha} f_s(t^{\beta}|p|) \tag{6.1}$$

The universality manifests itself in the value of α, β and the function form of f_s. A scaling theoretical analysis shows $\beta = \frac{1}{2}$ and $\alpha = \beta d$. Here d represents the dimension of the system. This universal evolution has been observed in a quenched 1 D Bose gas far away from equilibrium [52] and in a F = 1 ^{87}Rb spinor system with magnetization quenched far from equilibrium [53]. In the 1 D Bose gas system, α and β is determined to be 0.09 and 0.1, respectively. The deviation from the theory prediction is explained from two aspect. First, the scaling theory is based on a momentum-energy dual cascade. However, in 1 D with energy and momentum conservation, there is no such transport. Second, the contribution from higher dimensions, for atoms with momentum high enough that can seed thermalization, leads to the deviation of the 1 D system to 3D. With this dimension crossover, no theory prediction is available. The work done with ^{87}Rb spinor Bose gas ends up with $\alpha = 0.33$ and $\beta = 0.54$.

In our magnon work in Chapter 2, we observe a coarsening of the resultant quasi-condensate, with a slow transport of emergent macroscopic transverse magnetization towards lower momenta. This should be able to fit in the nonthermal fixed point scenario. Here we ask several questions regarding this non-thermal fixed point.

First, what is the relationship between the critical point and the non-thermal fixed point? While Kibble-Zurek theory [41–43] related to the former proliferates the high energy modes, the latter, within some k range, is supposed to govern the evolution of these high energy modes. Therefore, it will be experimentally interesting to distinguish the two through, for example, varying the quench time across phase transition and observing the subsequent evolution of the system. To verify the independence of the thermal fixed point from the critical point, or to make sure the latter's function is only to erase out the memory of the system, one can consider quenching the system towards the final state via phase transitions of different broken symmetry.

Second, just as thermal dynamical fixed points are classified through broken symmetries, is there a similar way to classify these nonthermal fixed points? The universal evolution governed by the nonthermal fixed point relates to transporting an emergent conserved quantity towards lower momenta, such as particle number in Bose gas and magnetization in spinor gas. The former is related to a breaking of U(1) symmetry. The latter is related to a breaking of spin-gauge SO(2) symmetry. To verify the dependence or independence of α, β and f_s on the symmetry of the Hamiltonian as well as the broken symmetry related to the emergent conserved quantity could be interesting. This topic can be explored by experiments on the evolution of high energy modes in systems with different underlined symmetry.

Third, current theory exploration shows the dependence of the universality on spatial dimension, like the real thermal dynamic fixed point. Therefore, experiments in different spatial dimension are required.

The ultracold spinor Bose gas, an isolated and well-controlled system, offers a nice experimental platform for this study. First, the interplay of spin-dependent interaction and quadratic Zeeman shift leads to a rich phase diagram [78]. Through tuning the quadratic Zeeman shift, one can quench the system from one phase to another. Thus both Kibble-Zurek physics and subsequent evolution which could be governed by the non-thermal fixed point can be addressed and studied. Second, by comparing the evolution of high energy modes supported by Hamiltonian of different symmetries, the relationship between the nonthermal fixed point and symmetry can be verified. Third, spin-independent optical trapping technique with the freedom of beam shaping can support spinor study in different spatial dimension.

Here we propose using ^{7}Li for this purpose. The advantage of ^{7}Li is the relative large spin-dependent interaction [78], which could speed up the evolution of high energy modes proliferated after the phase transition. In real experiment, we work with a quantum gas in optical dipole trap with finite lifetime. This speed-up can, in principle, help explore a larger k range evolution of the high energy modes within the finite lifetime, thus distinguish among regions dominated by KZ, thermal fixed point and other more complicated regions. For instance, a similar magnon condensing experiment could be done using ^{7}Li where we might expect quicker spin modes thermalization. For this purpose, a high resolution imaging system which can resolve features down to thermal de Broglie wavelength is required. For a quick estimation of ^{7}Li at 30 nK, this value is around 3.8 μm.

6.2 Atomtronics in heteronuclear system

In our daily-used computer, data is encoded as binary zeros and ones through orienting spins in magnetic materials using magnetic field pulses created by an electrical current. This process can dissipate huge amounts of energy and is relatively slow. One hot topic in spintronics is to perform spin transfer switching through spin current injection by the spin-torque effect [90], where local target spins can be switched to another state by strong enough spin current. Spin transfer switching would use much smaller currents to write data, and thus, it would be a more efficient technique.

Chapter 5 shows our results of ^{7}Li spin dynamics in a ^{87}Rb spin bath. This result can be interpreted as local ^{7}Li spin switching by injected ^{87}Rb spin current. To make a direct analogy between the two, we can take advantage of the trapping technique developed in cold atomic community. Fig. 6.1 shows a scheme of Rb spin current drives Li spin switching. Starting with two separated trapped ^{87}Rb and ^{7}Li reservoir with ^{87}Rb atom number much larger than ^{7}Li atom number, the spin of the two species can be controlled independently, say, through optical pumping. At t = 0, the two reservoirs are bridged by a channel formed by optical trapping potential. This complicated potential landscape can be made by projecting the image of a spatial light modulator (SLM) onto the atomic plane [91]. Due to the high chemical potential of ^{87}Rb , strong ^{87}Rb spin current could flow towards ^{7}Li reservoir, leading to ^{7}Li spin switching.

Another scenario shown in Fig. 6.2 on local spin switching can be as following. Consider a ^{7}Li spin tweezer and a nearby ^{87}Rb spin tweezer. The two tweezers can be merged together through tuning AOD driving frequency and power. The overlap density of the two can be enhanced by preparing both in the motional ground state, where the wavefunction overlap can be estimated by the zero point length, $z_0 = \sqrt{\hbar/(2m\omega)}$ [92]. For $\omega = 2\pi\times70$ kHZ, with the current spin-dependent interaction strength, one can get kHZ level switching rate. By repeatedly interacting ^{7}Li spin with ^{87}Rb spin prepared in the same spin state, ^{7}Li spin

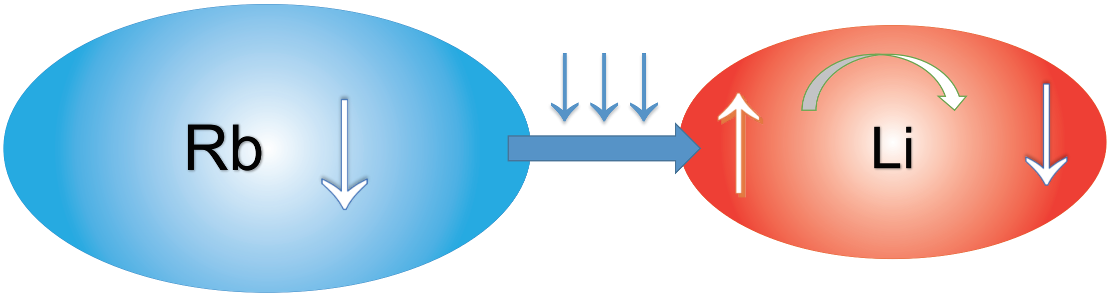

Figure 6.1: Spin Switching Scenario 1.

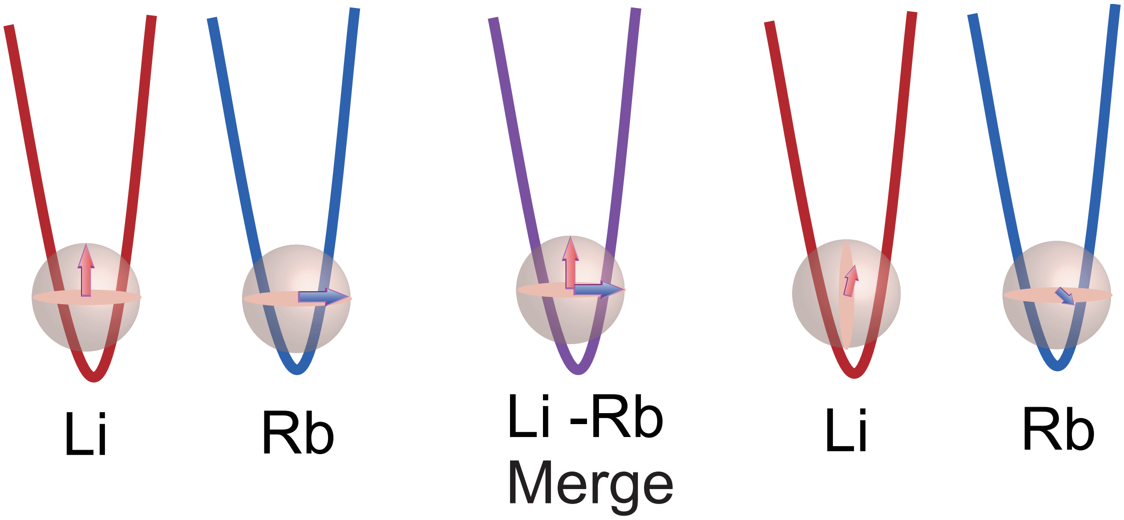

Figure 6.2: Spin Switching Scenario 2.

can be switched into any ^{87}Rb spin state locally. This spin-dependent interaction can be controlled by local magnetic field and can be coherent, and thus can be used for gate control as well as qubit switching [93–95].

This method is spatially selective, but does not include light scattering. So, for example, you might have a high density array of ^{7}Li atoms that encode some magnetic state (maybe memory). If we use resonant light to initialize a bit in this array, it will be hard to avoid also affecting memory in nearby bits – in fact, it will be essentially impossible to achieve this if the memory array is three dimensional. Alternately, as proposed here, one can imagine using a tweezer-trapped ^{87}Rb gas as a stylus: One would optically pump the ^{87}Rb and then position it at the ^{7}Li bit that one wants to initialize.

Here we use ^{7}Li-^{87}Rb as an example, the scenarios can be in principle applied to other systems with reasonable spin-dependent interaction strength.

Bibliography

[1] G. E. Marti, "Scalar and Spinor Excitations in a Ferromagnetic Bose-Einstein Condensate", PhD thesis (2014).

[2] R. E. Olf, "Creating, imaging, and exploiting collective excitations of a multicomponent Bose-Einstein condensate", PhD thesis (2015).

[3] R. Olf, F. Fang, G. E. Marti, A. MacRae, and D. M. Stamper-Kurn, "Thermometry and cooling of a Bose gas to 0.02 times the condensation temperature", Nature Physics **11**, 720 (2015).

[4] J. L. Bohn, A. M. Rey, and J. Ye, "Cold molecules: progress in quantum engineering of chemistry and quantum matter", Science **357**, 1002 (2017).

[5] F. Ferlaino, S. Knoop, and R. Grimm, *Ultracold Feshbach Molecules*, 2008.

[6] P. K. Molony, P. D. Gregory, Z. Ji, B. Lu, M. P. Köppinger, C. R. Le Sueur, C. L. Blackley, J. M. Hutson, and S. L. Cornish, "Creation of Ultracold ^{87}Rb^{133}Cs Molecules in the Rovibrational Ground State", Phys. Rev. Lett. **113**, 255301 (2014).

[7] K.-K. Ni, S. Ospelkaus, M. H. G. de Miranda, A. Pe'er, B. Neyenhuis, J. J. Zirbel, S. Kotochigova, P. S. Julienne, D. S. Jin, and J. Ye, "A high phase-space-density gas of polar molecules", Science **322**, 231 (2008).

[8] M. Guo, B. Zhu, B. Lu, X. Ye, F. Wang, R. Vexiau, N. Bouloufa-Maafa, G. Quéméner, O. Dulieu, and D. Wang, "Creation of an Ultracold Gas of Ground-State Dipolar ^{23}Na^{87}Rb Molecules", Phys. Rev. Lett. **116**, 205303 (2016).

[9] J. W. Park, S. A. Will, and M. W. Zwierlein, "Ultracold Dipolar Gas of Fermionic ^{23}Na^{40}K Molecules in Their Absolute Ground State", Phys. Rev. Lett. **114**, 205302 (2015).

[10] T. M. Rvachov, H. Son, A. T. Sommer, S. Ebadi, J. J. Park, M. W. Zwierlein, W. Ketterle, and A. O. Jamison, "Long-lived ultracold molecules with electric and magnetic dipole moments", Phys. Rev. Lett. **119**, 143001 (2017).

[11] B. Yan, S. A. Moses, B. Gadway, J. P. Covey, K. R. A. Hazzard, A. M. Rey, D. S. Jin, and J. Ye, "Observation of dipolar spin-exchange interactions with lattice-confined polar molecules", Nature **501**, 521 (2013).

[12] W. Ketterle, K. B. Davis, M. A. Joffe, A. Martin, and D. E. Pritchard, "High densities of cold atoms in a dark spontaneous-force optical trap", Phys. Rev. Lett. **70**, 2253 (1993).

[13] N. Radwell, G. Walker, and S. Franke-Arnold, "Cold-atom densities of more than 10^{12} cm^{-3} in a holographically shaped dark spontaneous-force optical trap", Phys. Rev. A **88**, 043409 (2013).

[14] J. Dalibard and C. Cohen-Tannoudji, "Laser cooling below the doppler limit by polarization gradients: simple theoretical models", J. Opt. Soc. Am. B **6**, 2023 (1989).

[15] G. Salomon, L. Fouché, P. Wang, A. Aspect, P. Bouyer, and T. Bourdel, "Gray-molasses cooling of ^{39}K to a high phase-space density", EPL (Europhysics Letters) **104**, 63002 (2013).

[16] A. Burchianti, G. Valtolina, J. A. Seman, E. Pace, M. De Pas, M. Inguscio, M. Zaccanti, and G. Roati, "Efficient all-optical production of large ^{6}Li quantum gases using D_1 gray-molasses cooling", Phys. Rev. A **90**, 043408 (2014).

[17] K. Kim, S. Huh, K. Kwon, and J.-y. Choi, "Rapid production of large ^{7}Li Bose-Einstein condensates using D_1 gray molasses", Phys. Rev. A **99**, 053604 (2019).

[18] L. Anderegg, B. L. Augenbraun, Y. Bao, S. Burchesky, L. W. Cheuk, W. Ketterle, and J. M. Doyle, "Laser cooling of optically trapped molecules", Nature Physics **14**, 890 (2018).

[19] I. Kozyryev, L. Baum, L. Aldridge, P. Yu, E. E. Eyler, and J. M. Doyle, "Coherent bichromatic force deflection of molecules", Phys. Rev. Lett. **120**, 063205 (2018).

[20] R. Dubessy, K. Merloti, L. Longchambon, P.-E. Pottie, T. Liennard, A. Perrin, V. Lorent, and H. Perrin, "Rubidium-87 Bose-Einstein condensate in an optically plugged quadrupole trap", Phys. Rev. A **85**, 013643 (2012).

[21] F. SIEVERS, "Ultracold Fermi mixtures and simultaneous sub-Doppler laser cooling of fermionic ^{6}Li and ^{40}K", PhD thesis (2014).

[22] D. Suchet, M. Rabinovic, T. Reimann, N. Kretschmar, F. Sievers, C. Salomon, J. Lau, O. Goulko, C. Lobo, and F. Chevy, "Analog simulation of weyl particles with cold atoms", EPL (Europhysics Letters) **114**, 26005 (2016).

[23] J. Burke Jr., C. Greene, and J. Bohn, "Multichannel Cold Collisions: Simple Dependences on Energy and Magnetic Field", Phys. Rev. Lett. **81**, 3355 (1998).

[24] B. P. Ruzic, C. H. Greene, and J. L. Bohn, "Quantum defect theory for high-partial-wave cold collisions", Phys. Rev. A **87**, 032706 (2013).

[25] J. Pérez-Ríos, S. Dutta, Y. P. Chen, and C. H. Greene, "Quantum defect theory description of weakly bound levels and Feshbach resonances in LiRb", New Journal of Physics **17**, 045021 (2015).

[26] J. Johansen, "FESHBACH AND EFIMOV RESONANCES IN A ^{6}Li-^{133}Cs ATOMIC MIXTURE", PhD thesis (2017).

[27] W. Hung, P. Huang, F.-C. Wu, M. Bruvelis, H.-Y. Xiao, A. Ekers, and I. A. Yu, "Storage time of cold Rb atoms in an optical dipole trap formed by a multimode fiber laser", J. Opt. Soc. Am. B **32**, B32 (2015).

[28] T. Lauber, J. Küber, O. Wille, and G. Birkl, "Optimized Bose-Einstein-condensate production in a dipole trap based on a 1070-nm multifrequency laser: Influence of enhanced two-body loss on the evaporation process", Phys. Rev. A **84**, 043641 (2011).

[29] X. Li, B. Zhu, X. He, F. Wang, M. Guo, Z.-F. Xu, S. Zhang, and D. Wang, "Coherent Heteronuclear Spin Dynamics in an Ultracold Spinor Mixture", Phys. Rev. Lett. **114**, 255301 (2015).

[30] F. Fang, R. Olf, S. Wu, H. Kadau, and D. M. Stamper-Kurn, "Condensing Magnons in a Degenerate Ferromagnetic Spinor Bose Gas", Phys. Rev. Lett. **116**, 095301 (2016).

[31] H. Watanabe and H. Murayama, "Unified Description of Nambu-Goldstone Bosons without Lorentz Invariance", Phys. Rev. Lett. **108**, 251602 (2012).

[32] G. E. Marti, A. MacRae, R. Olf, S. Lourette, F. Fang, and D. M. Stamper-Kurn, "Coherent magnon optics in a ferromagnetic spinor Bose-Einstein condensate", Phys. Rev. Lett. **113**, 155302 (2014).

[33] Y. Kawaguchi and M. Ueda, "Spinor Bose–Einstein condensates", Physics Reports **520**, Spinor Bose–Einstein condensates, 253 (2012).

[34] A. L. Gaunt, T. F. Schmidutz, I. Gotlibovych, R. P. Smith, and Z. Hadzibabic, "Bose-Einstein Condensation of Atoms in a Uniform Potential", Phys. Rev. Lett. **110**, 200406 (2013).

[35] T. F. Schmidutz, I. Gotlibovych, A. L. Gaunt, R. P. Smith, N. Navon, and Z. Hadzibabic, "Quantum Joule-Thomson Effect in a Saturated Homogeneous Bose Gas", Phys. Rev. Lett. **112**, 040403 (2014).

[36] N. Navon, A. L. Gaunt, R. P. Smith, and Z. Hadzibabic, "Critical dynamics of spontaneous symmetry breaking in a homogeneous Bose gas", Science **347**, 167 (2015).

[37] J. S. Guzman, "Explorations of Magnetic Phases in F = 1 ^{87}Rb Spinor Condensates", PhD thesis (2012).

[38] N. D. Mermin and T.-L. Ho, "Circulation and angular momentum in the A phase of superfluid helium-3", Phys. Rev. Lett. **36**, 594 (1976).

[39] T.-L. Ho, "Spinor Bose condensates in optical traps", Phys. Rev. Lett. **81**, 742 (1998).

[40] T. Ohmi and K. Machida, "Bose-Einstein condensation with internal degrees of freedom in alkali atom gases", J. Phys. Soc. Jpn. **67**, 1822 (1998).

[41] T. W. B. Kibble, "Topology of cosmic domains and strings", J. Phys. A **9**, 1387 (1976).

[42] W. H. Zurek, "Cosmological experiments in superfluid helium?", Nature **317**, 505 (1985).

[43] W. H. Zurek, "Cosmological experiments in condensed matter systems", Physics Reports-Review Section of Physics Letters **276**, 177 (1996).

[44] H. Saito, Y. Kawaguchi, and M. Ueda, "Kibble-Zurek mechanism in a quenched ferromagnetic Bose-Einstein condensate", Phys. Rev. A **76**, 043613 (2007).

[45] H. Saito, Y. Kawaguchi, and M. Ueda, "Topological defect formation in a quenched ferromagnetic Bose-Einstein condensates", Phys. Rev. A **75**, 013621 (2007).

[46] G. Labeyrie and R. Kaiser, "Kibble-Zurek Mechanism in the Self-Organization of a Cold Atomic Cloud", Phys. Rev. Lett. **117**, 275701 (2016).

[47] A. Keesling, A. Omran, H. Levine, H. Bernien, H. Pichler, S. Choi, R. Samajdar, S. Schwartz, P. Silvi, S. Sachdev, P. Zoller, M. Endres, M. Greiner, V. Vuletic, and M. D. Lukin, "Quantum Kibble-Zurek mechanism and critical dynamics on a programmable Rydberg simulator", Nature **568**, 207 (2019).

[48] B. Ko, J. W. Park, and Y. Shin, "Kibble-Zurek universality in a strongly interacting Fermi superfluid", Nature Physics **15**, 1227 (2019).

[49] P. C. Hohenberg and B. I. Halperin, "Theory of Dynamic Critical Phenomena", Rev. Mod. Phys. **49**, 435 (1977).

[50] L. Chomaz, L. Corman, T. Bienaimé, R. Desbuquois, C. Weitenberg, S. Nascimbène, J. Beugnon, and J. Dalibard, "Emergence of coherence via transverse condensation in a uniform quasi-two-dimensional Bose gas", Nat Commun **6** (2015).

[51] A. Piñeiro Orioli, K. Boguslavski, and J. Berges, "Universal self-similar dynamics of relativistic and nonrelativistic field theories near nonthermal fixed points", Phys. Rev. D **92**, 025041 (2015).

[52] S. Erne, R. Bücker, T. Gasenzer, J. Berges, and J. Schmiedmayer, "Universal dynamics in an isolated one-dimensional Bose gas far from equilibrium", Nature **563**, 225 (2018).

[53] M. Prüfer, P. Kunkel, H. Strobel, S. Lannig, D. Linnemann, C.-M. Schmied, J. Berges, T. Gasenzer, and M. K. Oberthaler, "Observation of universal dynamics in a spinor Bose gas far from equilibrium", Nature **563**, 217 (2018).

[54] J. Higbie, L. Sadler, S. Inouye, A. P. Chikkatur, S. R. Leslie, K. L. Moore, V. Savalli, and D. M. Stamper-Kurn, "Direct, non-destructive imaging of magnetization in a spin-1 Bose gas", Phys. Rev. Lett. **95**, 050401 (2005).

[55] G. E. Marti, R. Olf, E. Vogta, A. Ottl, and D. M. Stamper-Kurn, "Two-element Zeeman slower for rubidium and lithium", Phys. Rev. A **81**, .043424 (2010).

[56] G. C. Bjorklund, M. D. Levenson, W. Lenth, and C. Ortiz, "Frequency modulation (fm) spectroscopy", Applied Physics B **32**, 145 (1983).

[57] A. T. Grier, I. Ferrier-Barbut, B. S. Rem, M. Delehaye, L. Khaykovich, F. Chevy, and C. Salomon, "Λ-enhanced sub-Doppler cooling of lithium atoms in D_1 gray molasses", Phys. Rev. A **87**, 063411 (2013).

[58] F. Sievers, N. Kretzschmar, D. R. Fernandes, D. Suchet, M. Rabinovic, S. Wu, C. V. Parker, L. Khaykovich, C. Salomon, and F. Chevy, "Simultaneous sub-Doppler laser cooling of fermionic ^{6}Li and ^{40}K on the D_1 line: Theory and experiment", Phys. Rev. A **91**, 023426 (2015).

[59] U. Schünemann, H. Engler, R. Grimm, M. Weidemüller, and M. Zielonkowski, "Simple scheme for tunable frequency offset locking of two lasers", Review of Scientific Instruments **70**, 242 (1999).

[60] S. Dutta, A. Altaf, J. Lorenz, D. S. Elliott, and Y. P. Chen, "Interspecies collision-induced losses in a dual species ^{7}Li–^{85}Rb magneto-optical trap", Journal of Physics B: Atomic, Molecular and Optical Physics **47**, 105301 (2014).

[61] C. Marzok, B. Deh, P. W. Courteille, and C. Zimmermann, "Ultracold thermalization of ^{7}Li and ^{87}Rb", Phys. Rev. A **76**, .052704 (2007).

[62] M. V. Romalis and E. N. Fortson, "Zeeman frequency shifts in an optical dipole trap used to search for an electric-dipole moment", Phys. Rev. A **59**, 4547 (1999).

[63] F. Fang, S. Wu, A. Smull, J. A. Isaacs, Y. Wang, C. H. Greene, and D. M. Stamper-Kurn, "Cross-dimensional relaxation of ^{7}Li$-^{87}$Rb atomic gas mixtures in a spherical-quadrupole magnetic trap", Phys. Rev. A **101**, 012703 (2020).

[64] Y. G. O. Harms, D. Haubrich, H. Schadwinkel, F Strauch, B. Ueberholz, S. Wiesche, and D. Meschede, "Magnetostatic traps for charged and neutral particles", Hyperfine Interactions **109**, 281 (1997).

[65] J. Goldwin, S. Inouye, M. L. Olsen, B. Newman, B. D. DePaola, and D. S. Jin, "Measurement of the interaction strength in a Bose-Fermi mixture with ^{87}Rb and ^{40}K", Phys. Rev. A **70**, .021601 (2004).

[66] J. Goldwin, S. Inouye, M. L. Olsen, and D. S. Jin, "Cross-dimensional relaxation in Bose-Fermi mixtures", Phys. Rev. A **71**, .043408 (2005).

[67] V. V. Ivanov, A. Khramov, A. H. Hansen, W. H. Dowd, F. Münchow, A. O. Jamison, and S. Gupta, "Sympathetic cooling in an optically trapped mixture of alkali and spin-singlet atoms", Phys. Rev. Lett. **106**, 153201 (2011).

[68] M. Egorov, B. Opanchuk, P. Drummond, B. V. Hall, P. Hannaford, and A. I. Sidorov, "Measurement of s-wave scattering lengths in a two-component Bose-Einstein condensate", Phys. Rev. A **87**, 053614 (2013).

[69] C. Marzok, B. Deh, C. Zimmermann, P. W. Courteille, Y. V. V. E. Tiemann, and A. Saenz, "Feshbach resonances in an ultracold ^{7}Li and ^{87}Rb mixture", Phys. Rev. A **79**, .012717 (2009).

[70] R. A. W. Maier, M. Eisele, E. Tiemann, and C. Zimmermann, "Efimov resonance and three-body parameter in a lithium-rubidium mixture", Phys. Rev. Lett. **115**, 043201 (2015).

[71] J. Pérez-Ríos, S. Dutta, Y. P. Chen, and C. H. Greene, “Quantum defect theory description of weakly bound levels and Feshbach resonances in LiRb”, New Journal of Physics **17**, 045021 (2015).

[72] G. Breit and I. I. Rabi, “Measurement of nuclear spin”, Phys. Rev. **38**, 2082 (1931).

[73] J. Burke Jr., J. Bohn, B. Esry, and C. Greene, “Impact of the ^{87}Rb singlet scattering length on suppressing inelastic collisions”, Phys. Rev. A **55**, R2511 (1997).

[74] Private communication with Dr. Eite Tiesinga.

[75] C. Buggle, J. Léonard, W. von Klitzing, and J. T. M. Walraven, “Interferometric Determination of the s and d-Wave Scattering Amplitudes in ^{87}Rb”, Phys. Rev. Lett. **93**, 173202 (2004).

[76] C. Chin, R. Grimm, P. Julienne, and E. Tiesinga, “Feshbach resonances in ultracold gases”, Rev. Mod. Phys. **82**, 1225 (2010).

[77] I. Zutic, J. Fabian, and S. Das Sarma, “Spintronics: fundamentals and applications”, Rev. Mod. Phys. **76**, 323 (2004).

[78] D. M. Stamper-Kurn and M. Ueda, “Spinor Bose gases: Symmetries, magnetism, and quantum dynamics”, Rev. Mod. Phys. **85**, 1191 (2013).

[79] A. M. Rey, V. Gritsev, I. Bloch, E. Demler, and M. D. Lukin, “Preparation and detection of magnetic quantum phases in optical superlattices”, Phys. Rev. Lett. **99**, 140601 (2007).

[80] H. K. Pechkis, J. P. Wrubel, A. Schwettmann, P. F. Griffin, R. Barnett, E. Tiesinga, and P. D. Lett, “Spinor Dynamics in an Antiferromagnetic Spin-1 Thermal Bose Gas”, Phys. Rev. Lett. **111**, 025301 (2013).

[81] X. He, B. Zhu, X. Li, F. Wang, Z.-F. Xu, and D. Wang, “Coherent spin-mixing dynamics in thermal ^{87}Rb spin-1 and spin-2 gases”, Phys. Rev. A **91**, 033635 (2015).

[82] C. K. Law, H. Pu, and N. P. Bigelow, “Quantum Spins Mixing in Spinor Bose-Einstein Condensates”, Phys. Rev. Lett. **81**, 5257 (1998).

[83] L. E. Sadler, J. M. Higbie, S. R. Leslie, M. Vengalattore, and D. M. Stamper-Kurn, “Spontaneous symmetry breaking in a quenched ferromagnetic spinor Bose–Einstein condensate”, Nature **443**, 312 (2006).

[84] U. Ebling, J. S. Krauser, N. Fläschner, K. Sengstock, C. Becker, M. Lewenstein, and A. Eckardt, “Relaxation Dynamics of an Isolated Large-Spin Fermi Gas Far from Equilibrium”, Phys. Rev. X **4**, 021011 (2014).

[85] Z. F. Xu, D. J. Wang, and L. You, “Quantum spin mixing in a binary mixture of spin-1 atomic condensates”, Phys. Rev. A **86**, 013632 (2012).

[86] A. Mil, T. V. Zache, A. Hegde, A. Xia, R. P. Bhatt, M. K. Oberthaler, P. Hauke, J. Berges, and F. Jendrzejewski, *Realizing a scalable building block of a u(1) gauge theory with cold atomic mixtures*, 2019.

[87] N. Navon, C. Eigen, J. Zhang, R. Lopes, A. L. Gaunt, K. Fujimoto, M. Tsubota, R. P. Smith, and Z. Hadzibabic, “Synthetic dissipation and cascade fluxes in a turbulent quantum gas”, Science **366**, 382 (2019).

[88] J. Berges, A. Rothkopf, and J. Schmidt, “Nonthermal fixed points: effective weak coupling for strongly correlated systems far from equilibrium”, Phys. Rev. Lett. **101**, 041603 (2008).

[89] C. Scheppach, J. Berges, and T. Gasenzer, “Matter-wave turbulence: beyond kinetic scaling”, Phys. Rev. A **81**, 033611 (2010).

[90] M. D. Stiles and J. Miltat, “Spin dynamics in confined magnetic structures iii”, in , edited by B. Hillebrands and A. Thiaville (Springer Berlin Heidelberg, Berlin, Heidelberg, 2006) Chap. Spin-Transfer Torque and Dynamics, pp. 225–308.

[91] D. H. White, T. A. Haase, D. J. Brown, M. D. Hoogerland, M. S. Najafabadi, J. L. Helm, C. Gies, D. Schumayer, and D. A. W. Hutchinson, *Observation of two-dimensional anderson localisation of ultracold atoms*, 2019.

[92] L. R. Liu, J. T. Zhang, Y. Yu, N. R. Hutzler, Y. Liu, T. Rosenband, and K.-K. Ni, *Ultracold molecular assembly*, 2017.

[93] D. Hayes, P. S. Julienne, and I. H. Deutsch, “Quantum logic via the exchange blockade in ultracold collisions”, Phys. Rev. Lett. **98**, 070501 (2007).

[94] C. Weitenberg, S. Kuhr, K. Mølmer, and J. F. Sherson, “Quantum computation architecture using optical tweezers”, Phys. Rev. A **84**, 032322 (2011).

[95] G. Pagano, F. Scazza, and M. Foss-Feig, “Fast and scalable quantum information processing with two-electron atoms in optical tweezer arrays”, Advanced Quantum Technologies **2**, 1800067 (2019).